MONTAN
UNIVERSITÄT
LEOBEN

Chair of Petroleum and Geothermal Energy Recovery

Master's Thesis

Measurement and acquisition of accessible production data for the training of a mathematical model based on artificial intelligence to predict multiphase flow rates by means of a virtual flow meter (VFM)

Patrick Jasek, BSc

July 2020

Author:
BSc. Patrick Jasek
m01435158

Advisor: DDI. Dr. Clemens Langbauer
DI. Dr. Rudolf Fruhwirth

Leoben, ………………

MONTANUNIVERSITÄT LEOBEN
www.unileoben.ac.at

EIDESSTATTLICHE ERKLÄRUNG

Ich erkläre an Eides statt, dass ich diese Arbeit selbständig verfasst, andere als die angegebenen Quellen und Hilfsmittel nicht benutzt, und mich auch sonst keiner unerlaubten Hilfsmittel bedient habe.

Ich erkläre, dass ich die Richtlinien des Senats der Montanuniversität Leoben zu "Gute wissenschaftliche Praxis" gelesen, verstanden und befolgt habe.

Weiters erkläre ich, dass die elektronische und gedruckte Version der eingereichten wissenschaftlichen Abschlussarbeit formal und inhaltlich identisch sind.

Datum 27.05.2020

Unterschrift Verfasser/in
Patrick, Jasek

AFFIDAVIT

I hereby declare that the content of this work is my own composition and has not been submitted previously for any higher degree. All extracts have been distinguished using quoted references and all information sources have been acknowledged.

Danksagung / Acknowledgement

First of all, I would like to express my gratitude to my advisor Dr. Clemens Langbauer for his constant support and guidance during the experimental-phase and throughout the whole project. He gave me the opportunity to be part of his team and grow personally and professionally. I am very thankful to my second advisor Dr. Rudolf Fruhwirth, for his support in working with artificial neural networks and his valuable hints for visual data presentation. I wish to thank Ing. Andreas Öfler for his help and collaboration in the various construction and maintenance works during the experiments in the pump testing-facility. Finally, I express my greatest thanks and appreciation to my parents, my brother, Marta Muszynska and Radoslaw Matusiak for their support, and constant encouragement during my work.

Kurzfassung

Die Echtzeit-Produktionsüberwachung in der Öl- und Gasindustrie ist von großer Bedeutung, insbesondere da die Feldoperationen mit zunehmender Erschöpfung der Lagerstätten wirtschaftlich marginal werden. Produktionsmessungen werden normalerweise mit herkömmlichen Testabscheideranlagen durchgeführt, die keine kontinuierlichen Produktionsinformationen liefern. Eine Alternative bietet ein physikalischer Mehrphasen-Durchflussmesser, dessen Anwendung erwünscht, aber kostspielig ist und ein gutes Verständnis der maßgeblichen Systemphysik und der Fluidchemie erfordert.

Diese Arbeit beschreibt die Entwicklung einer innovativen Messtechnik, die als virtueller Durchflussmesser (VFM) bezeichnet wird. VFMs sind datenbasierte mathematische Modelle, die für Echtzeit-Mehrphasen-Durchflussvorhersagen genutzt werden. Sie basieren auf leicht zugänglichen Sensorwerten aus Bohrlöchern. Für diese Arbeit wurden verschiedene physiklaische Eigenschaften gemessen und bei kontrollierten Laborbedienungen aufgezeichnet, um Eingabedaten zum Lernen, Validieren und Testen eines künstlichen neuronalen Netzwerks (ANN) bereitzustellen. Die Experimente wurden im Pumpenteststand (PTS) mit einer vertikal installierten elektrischen Tauchkreiselpumpe (ESP) an der Montanuniversität in Leoben durchgeführt. Ziel war es, einen dreiphasigen Strömungskreislauf zu konstruieren, in dem verschiedene Strömungskonfigurationen unter festen, zuverlässigen und wiederholbaren Laborbedingungen getestet und quantifiziert werden können. Die Idee war, ein breites Spektrum verschiedener Strömungsbedingungen zu analysieren, indem die Strömungsraten manipuliert und gleichzeitig die entlang des Strömungswegs installierten Sensordaten aufgezeichnet wurden. Anschließend wurden sowohl Sensordaten als auch die Durchflussmessungen verarbeitet und als Eingabe für das mathematische Modell verwendet.

Das experimentelle Programm bestand aus 32 Experimenten, 3 einphasigen, 11 zweiphasigen und 18 dreiphasigen Experimenten. Insgesamt konnten 85 verschiedene Strömungskonfigurationen untersucht werden. Alle dreiphasigen Experimente, die aus 19 verschiedenen Paramteren und Durchflussraten von Wasser, synthetischem Öl und Druckluft bestehen, wurden im VFM-Modell zur mehrphasigen Durchflussvorhersage implementiert. Zunächst wurde jedes einzelne Experiment einzeln untersucht und modelliert, um die Unterschiede in der Genauigkeit der Durchflussvorhersage als Funktion der Durchflussrate jeder Phase zu analysieren. Schließlich wurden die verarbeiteten Daten aller 18 Dreiphasenexperimente zusammen in drei getrennten neuronalen Netzen für Wasser, Öl und Gas als Ausgangssignale modelliert, um Interferenzen zwischen den vorhergesagten Durchflussraten zu vermeiden, da sich die analysierten Durchflussspektren erheblich unterscheiden. Die erreichte Vorhersagegenauigkeit der Phasen ist technisch nützlich und führt zu einem durchschnittlichen relativen Fehler von 1,20%, 4,85% und 2,40% für Wasser, Öl und Gas. Die gemessenen Durchflussspektren liegen zwischen 0-12 m^3/h für Wasser, 0-2,8 m^3/h für Öl und 0-18 kg/h für Gas.

Das erstellte Modell kann Durchflussraten bei technisch angemessenen Durchflussspektren vorhersagen und beweist das Potenzial von Sensordaten bei der Mehrphasen-Durchflussvorhersage und somit die Fähigkeit zur Echtzeitüberwachung der Produktion.

Abstract

Real-time production monitoring in the oil and gas industry has become very significant particularly as field operations become economically marginal with increasing reservoir depletion. Production measurements are typically performed with conventional test-separator facilities, which don’t deliver continuous production information. An alternative solution are physical multiphase flow meter. Their application is desired but costly and requires a good understanding of the governing system physics and fluid chemistry.

This work describes the development of an innovative metering technology, which is known as Virtual flow meter (VFM). VFMs are data-based mathematical models for real-time multiphase flow prediction, which make use of readily accessible sensor readings from wells. For this work different physical properties were measured and recorded in a controlled laboratory environment to provide input data for learning, validation and testing of an artificial neural network (ANN). The experiments were conducted in the Pump testing-facility (PTF) using a vertically installed electric submersible pump (ESP) at the Montanuniversity in Leoben. The objective was to construct a three-phase flow loop were different flow configurations could be tested and quantified under firm, reliable and repeatable laboratory conditions. The idea was to analyze a broad spectrum of different flow conditions, by manipulating the flow rates and simultaneously record the sensor responses installed along the flow path. Both, sensor data and flow measurements were then processed and used as input for the mathematical model.

The experimental program consisted of 32 experiments, 3 single-phase, 11 two-phase and 18 three-phase experiments. In total 85 different flow configurations could be investigated. All three-phase experiments consisting of 19 different records and flow rates of water, synthetic oil and pressurized air were implemented in the VFM model for multiphase flow prediction. Initially, every single experiment was investigated and modeled individually to analyze the differences in flow prediction accuracy as a function of the flow rate of each phase. Finally, the processed data of all 18 three-phase experiments were modeled together in three separate neural networks with water, oil and gas as outputs, to avoid any interference between the predicted flow rates due to different output ranges. The reached prediction accuracy of the phases is technically useful and results in an average relative error of 1,20%, 4,85% and 2,40% for water, oil and gas respectively. The measured flow rate ranges are between 0-12 m^3/h for water, 0-2,8 m^3/h for oil and 0-18 kg/h for gas.

The created model can predict flow rates at reasonable flow rates and proves the potential of sensor-data in multiphase flow prediction and is herewith capable to monitor production outputs in real-time.

Table of Content

Page

1 Introduction

The occurrence of multiphase flow can be observed in many processes of nature, like raindrops falling through the air, blood flow in veins or earth avalanches moving down mountain slopes. The phenomenon of multiphase flow is a well-studied problem and was mathematically described and investigated in both flow-conducts and porous media. This work focuses on the measurement of multiphase flow in a pipe system consisting of connector-tubes, pipes, and pumps, typically used in the production of oil and gas. In general, multiphase flow is part of numerous industrial applications like the pharmaceutical, food, or oil and gas industry. To measure and improve multiphase flow metering techniques, advanced knowledge about the fluid phases and their physical behavior is required. The measurement setup and the measuring instruments must be chosen accordingly to the transported components and must utilize the required accuracy. There are no universal flow meters available. The measurement accuracy of flow systems within a process is typically regulated by the law based on the expertise of metrology associations. In the oil industry production allocation measurements on concessions with shared facilities must be recorded and documented. Reliable measurements are required to assure accurate production allocation and are the basis for fiscal transfer calculations. The fluid streams need to be quantified before entering a common processing station or flow line. The reason for a unified and strict metering regulation is the money transfer between companies or the government. The biggest difficulty in measuring multiphase flow is the complex nature of fluids produced from wells. This is why companies agree on specified uncertainty limits, based on the state of the art metrology systems. The produced fluid mixture in oil wells typically covers a wide spectrum of different flowing conditions and components. For decades scientists with different backgrounds like aerospace, chemistry, environmental, or petroleum engineering investigate the multiphase flow phenomenon and try to model its behavior. In the petroleum industry, this need is evident for many decades. Since the 1980s, several flow-metering instruments have been manufactured, based on different physical principles. Nowadays these metering systems are often combined to improve measurement accuracy. Flow meters differ in their design and offer advantages in size, measuring range, or quantification principle. In the oil and gas industry, the identification of produced fluids at individual wells is important for profit calculations, production forecasts and production decline analyzes. These information are necessary to make decisions about stimulation operations, artificial lift implementation, or well abandonments. With the recorded data it is possible to identify production changes earlier and propose better solutions like e.g. pump replacements or re-completions from production to injection wells. Typically, produced fluids from different operators are commingled in one flowline and directed to a separator station, where the fluid fractions are separated based on gravity due to their different densities. In the next step, the separated phases are measured by a single-phase flow meter like e.g. orifices for gas and turbine meters for oil and water (Corneliussen et al. 2005). The main disadvantage of this methodology is the missing information about the contribution of each well to the overall production. Therefore, the interest to develop multiphase flow meters for individual wells is continuously growing, especially as reservoirs are getting more depleted and the offshore application of test-separators is costly and often limited due to space and weight restrictions. The technology in the field has advanced and the accessibility of multiphase flowmeters (MFM) capable to perform at the desired accuracy level has increased. Nowadays, MFM can measure oil, water and gas rates from wells without the need for separation. They form an important part of on- and offshore installations. Commissioning is relatively fast onshore, but the calibration and maintenance especially offshore are time-consuming and costly. During the calibration process, the verification of metering failure for the expected operation window is calculated. To reduce the calibration frequency new methods using mathematical models based on artificial intelligence were developed. The use of artificial neural networks (ANNs) proved to work very well in many different fields of the oil and gas industry like e.g. seismicity, reservoir modeling, or drilling. In terms of multiphase flow metering, the concept of virtual flowmeter (VFM) gained momentum over the last decade. Primarily, the systems were planned to serve as a solution for malfunction identification. The requirement to develop these models was to provide enough production data. With the growing trend of generating additional value from history data within the companies, improved backup systems based on ANN were developed to serve as an alternative solution for MFM. Whereas, mechanistic models still suffer from the necessity of matching dynamically changing flow conditions and complex fluid composition, models based on artificial intelligence (AI) are driven by the generated production data from senor records. Gathered readings from different operational modes like e.g. well shut-in, production restart, steady production, etc. allow to generate a reliable model. The prediction accuracy of VFMs based on mechanistic principles is sensitive to time and associated system changes. Data based VFMs are not physical tools but more an information library created from recorded data to deliver results at low costs. In most of the applications VFMs consist of readily accessible pressure and temperature data from installed sensors along the flow path. (Mokhtari und Waltrich 2016; Corneliussen et al. 2005).

The acceptance of VFMs for fluid fraction determinations is questioned by the leading metrology agencies and government institutions. However, associations like the American Petroleum Institute acknowledged, and recommend the use of VFM models as an alternative for physical MFMs, particularly in the subsea application where several well streams are produced into a shared separator (Corneliussen et al. 2005).

The current uncertainty results from the lack of literature and academic studies, which would quantify the feasibility and reliability of VFM models. Only a few studies deliver promising results regarding flow rate determination, proving accuracy levels in the range between 1% and 10% relative to test-separator measurements. Nevertheless, more studies are required to validate the application and performance of VFM-models in different fields at wider ranges of conditions. (Mokhtari und Waltrich 2016); (Haldipur und Metcalf 2008); (Melbø et al. 2003; Melbø).

1.1 Problem statement and motivation of the study

To understand the new opportunities brought by VFMs, one needs to understand the different application principles of MFMs and test-separator systems. When measuring with separator-based methods, relatively stable inflow conditions are required, to obtain reliable results. This might consume a significant amount of time, particularly for offshore wells with long flow lines and tiebacks. MFMs, which measure the individual flow rate directly on the wellhead, theoretically solve this problem. Nowadays, it is possible to quantify flow rates in real-time. However, these types of meters are expensive and require frequent calibration and long-term maintenance. Additionally, their performance is limited by specific operation conditions. At high Gas-Volume-Fraction (GVF) and Water-Liquid-Ratios (WLR), the uncertainty in oil rate prediction increases significantly (Falcone et al., 2009). The majority of MFMs show increased errors for GVF > 90%. Further, if the presence of precipitates like wax or scales is likely to occur, the accuracy of MFMs can be highly affected.

Therefore, an independently measuring backup system would be desirable in case a MFM fails or measures outside of its operating envelope (Corneliussen et al. 2005). In the last decade, companies started to use VFMs as a backup system (Dellarole et al. 2005). These VFM systems used conventional sensors to measure pressure and temperature. The pressure drop over a choke or a pipe section is used to estimate flow rates, whereas, combined with temperature changes, densities and further compositions are calculated (Falcone et al. 2010). VFM-models can deliver production rates in real-time and allow to analyze the changes in production performance for production and reservoir management. VFM-models are used to monitor single wells or entire fields of co-mingled wells (Mokhtari und Waltrich 2016). Another potential field of application for VFM models is the production allocation. Conventionally, in multiple well systems, the streams are comingling into one production separator. If a well is tested the stream is directed to test-separator, for fraction measurements. These separators are expensive and typically there are more wells than test-separators in the field. Therefore, conventional allocation tests are time-consuming and lead to delayed results. Production tests last between several hours up to a couple of days. To avoid frequent production delays, well tests are executed usually within a time interval of one month. However, the fraction of produced fluids in individual wells may vary significantly between the test intervals. VFM-models offer a solution to this problem, while simultaneously offering a performance monitoring system (Varyan et al. 2015).

1.2 Objectives

The main objectives of this study are:

1. Execution of laboratory measurements for different multiphase flow arrangements using an electrical submersible pump (ESP).

2. Data collection and processing, for the generation of a data-based multiphase flow prediction system using artificial neural networks (ANNs).

Within this study, the accuracy of a newly created VFM-model at stable and controllable laboratory conditions is analyzed. The recorded data was used for creating an ANN for oil, water, and gas flow determination. The questions that are aimed to be answered in this study are the following:

- Is there any relationship between recorded data and flowrates that can be modeled?
- What accuracy can be reached in three-phase experiments based on the laboratory data?
- What data is carrying more valuable information in terms of multiphase prediction?

2 Literature review

As described earlier fluids produced from wells are rarely pure liquids or gases but more often mixtures of hydrocarbons and water. The reservoir fluids enter the well as a multiphase mixture with three or more phases. Depending on the geological formation and physical conditions a variety of solid phases like sand, hydrates, and waxes can be by-produced. The total throughput of commingled streams of several wells is measured after a complete phase separation in three-phase separators, using conventional single-phase meters.

In mature oilfields, any reduction of facility costs regarding maintenance is significant to shift the economical limit of these fields in time and prolong their feasibility. Here, the replacement of expensive test separators and test-lines by compact and reliable MFMs might increase the production time of the field. Another application possibility for MFMs is the hydrocarbon recovery in remote locations on-and offshore. Mostly where the economic developments have pushed the offshore production towards subsea completions systems, which often use several kilometer-long pipelines to connect the wells with the processing facilities either on the shore or platform. In these fields, MFMs would reduce the number of facilities needed, which might positively impact the costs. Of primary importance is the reduction of test separators for well-testing applications. Using MFMs, with its favorable small footprint, for offshore applications it is possible to save space on platforms and reduce loads. Additionally, the costs of long well-test lines in unmanned locations, deep-water projects and remotely monitored satellite fields could be saved.

To optimize flow measurements the implemented MFMs need to quantify the fluids streams over a wide range of possible conditions. In particular, the flow rate may reach from 150 m^3/day to 5500 m^3/day, gas-oil ratios (GOR) from 18 Sm^3/m^3 to 2000 Sm^3/m^3 and water liquid ratios (WLR) ranging from 0-98%. Additionally, the pressure range is significant and can reach up to 700 bar whereas the Temperature is typically between 50°C to 150°C. Another level of complexity is added due to the changing tubing diameters along the path. Typical production tubings are in the range between 50 mm to 200 mm, whereas subsea or underground flow lines are between 200 and 1000 mm. The quantification of such a complex system, which shows dynamic changes over the lifetime of a well is challenging. The biggest advantages of the new measuring technique are given in terms of production allocation, continuous production monitoring, and significant metering cost reduction (Falcone et al. 2010).

2.1 Multiphase flow

In single flow problems, we can use mathematical descriptions like the velocity profile, turbulence, and boundary layers to classify and solve the flow behavior. For a multiphase fluid, flowing through pipe conduct, these single-phase characteristics are insufficient to describe, understand and control multiphase flow. Multiphase flow is highly dependent on operating conditions, fluid properties, rates, pipe geometry, and inclination. The operator can control the flow regime just to a small extent that's why one needs to know which flow characteristics the pumped fluid has to derive what problems might occur. This question pushed engineers to set up laboratory experiments using transparent pipes to observe and classify the flow structures also called flow regimes of various fluids at different conditions. These regimes were combined to maps and divided into flow patterns that describe the flow in vertical and horizontal pipes. The description of flow regimes and their transition is to some extent arbitrary and depends on the interpretation of the observer. To describe the complex behavior of multiphase flow streams, one needs to understand which features are influencing the flow. Transient effects occur when the boundary conditions of the observed system are changed e.g. opening or closing a valve. Further geometry and terrain effects influence the velocity and pressure inside the pipe and affect the phases distribution. If the above-described effects are held constant, the fluid flow is entirely controlled by the fluid physical and chemical properties. Generally, all flow regimes can be classified into a dispersed, separated, or intermittent flow. In dispersed flow, the transported fluid shows a uniform distribution of the fluid in all directions. Typical examples are bubble and mist flow, which can be seen in Figure 1. Separated flow is characterized by a continuous phase distribution in the flow direction and a non-continuous phase in the radial direction. Representatives of this regime are stratified and annular flow. Intermittent flow occurs when two phases travel through the pipe in the form of slugs, plugs, and churns and show a phase discontinuity in the flow direction as shown in Figure 2Figure 1. Finally, the flow regime is also a function of the liquid-liquid or liquid-gas interaction (Corneliussen et al. 2005).

2.2 Multiphase flow maps

The following figures for horizontal and vertical flow respectively illustrate the flow characteristics in a two-phase liquid-gas regime as a function of the superficial velocity. The superficial velocity of a gas or liquid is a hypothetical velocity at which the fluid would travel in the absence of any other fluid in the pipe and is defined as the flow rate of the fluid divided by the flow conduct diameter, as shown in equation 1. Where $v_{s,i}$ is the superficial velocity of the traveling fluid, Q_i is the flow rate of the fluid and A is the pipe diameter.

$$v_{s,i} = \frac{Q_i}{A} \qquad \text{(Eq. 1)}$$

The sum of superficial gas velocity $v_{s,gas}$ and superficial liquid velocity $v_{s,liquid}$ is the mixture velocity v_m and is written in equation 2.

$$v_m = v_{s,gas} + v_{s,liquid} \qquad \text{mixture velocity} \qquad \text{(Eq. 2)}$$

Flow regime maps describe the flow characteristics either in the horizontal or vertical flow direction. For both horizontal and vertical flow systems, the transition from one to the other flow regime is dependent on the pipe diameter, interfacial tension, and fluid density. In Figure 1, we can identify seven different flow regimes illustrated as a function of superficial velocities. It is important to remember that these values serve as an orientation of how the flow characteristics change with increasing or decreasing superficial velocities. To use such a map for precise determination one would need to record the behavior for each, individually observed system. This means that each map is only valid for a specific pipe material, fluid and transport properties.

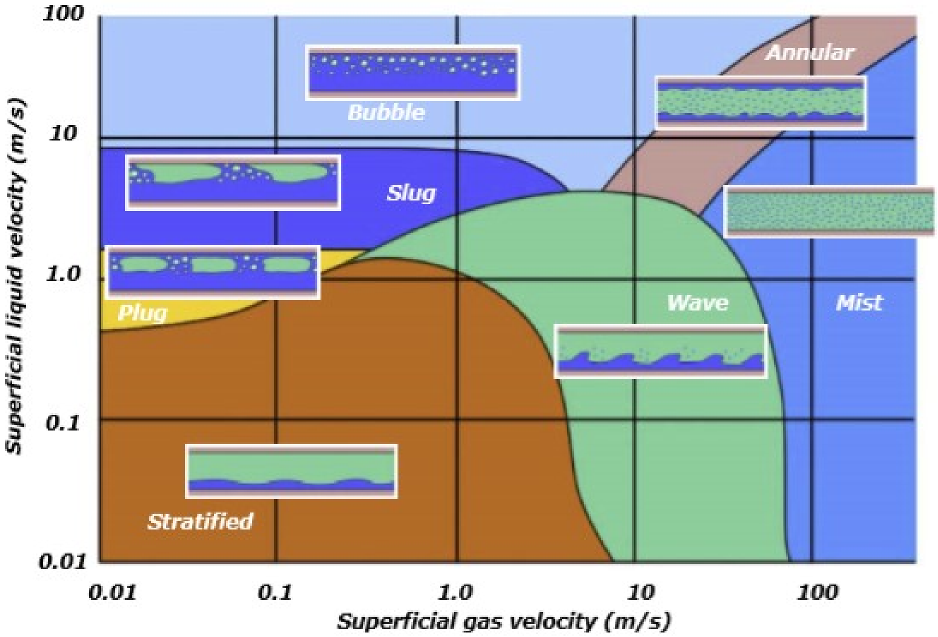

Figure 1. Flow regimes in horizontal pipes (Corneliussen et al. 2005)

Like the horizontal flow map also the vertical flow map shows the dependence of the flow structures and the individual superficial velocities. In the illustration for vertical flow in Figure 2, only five different regimes occur. This figure shows that at a certain superficial gas velocity the flow will remain annular for all superficial liquid velocities (Corneliussen et al. 2005).

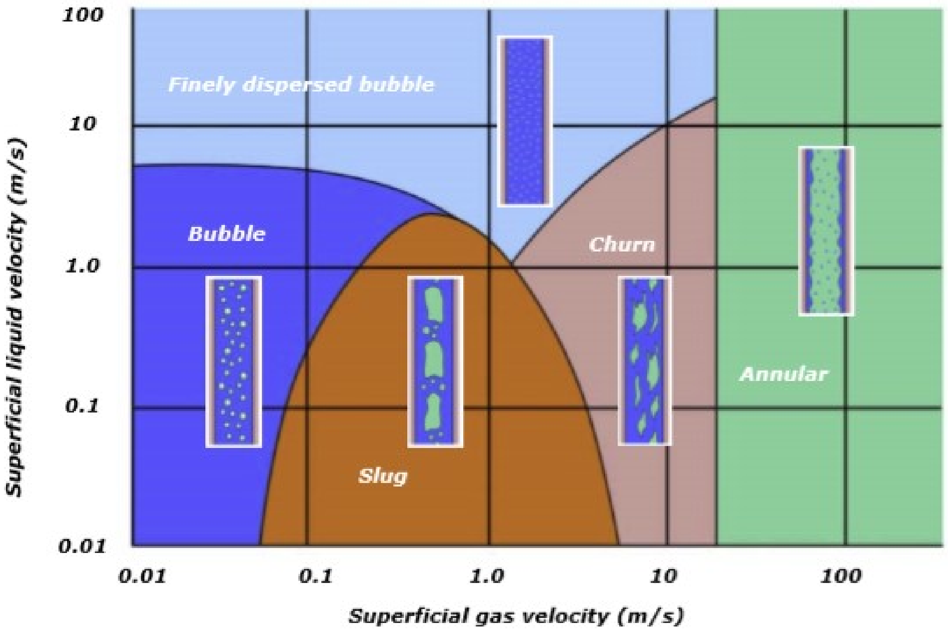

Figure 2. Flow regimes in vertical pipes (Corneliussen et al. 2005)

2.3 Slip properties

It is important to understand how the flow of a multi-component system can be described. According to the multiphase flow regimes discussed earlier, it is necessary to introduce new mathematical properties describing the distribution of the phases in flow conducts. At static or no-slip conditions the area occupied by a fluid is expressed in fractions of the pipe sectional area called gas void fraction, λ_{gas} for gases and liquid hold-up, λ_{liquid} for liquids. When two fluids at different physical states travel along a flowline the portion of the pipe occupied by a liquid will be greater than the section occupied by gas. This can be explained by the higher traveling velocity of gases in general and the tendency of liquids to accumulate in horizontal or inclined sections. For this purpose, the liquid hold-up, λ_{liquid} and the gas void fraction, λ_{gas} are defined as shown in equations 3 and 4. Where A_{liquid} and A_{gas} are the areas of the pipe occupied by a liquid and gas respectively and A_{pipe} is the cross-section of the pipe.

$\lambda_{liquid} = \frac{A_{liquid}}{A_{pipe}}$ Liquid hold-up (Eq. 3)

$\lambda_{gas} = \frac{A_{gas}}{A_{pipe}}$ Gas void fraction (Eq. 4)

The liquid hold-up and the gas void fraction add up to one. The same is valid for the gas and liquid volume fraction, which describes the volumetric flow of one phase α_i, defined as the volumetric flow of one individual phase, q_i relative to the volumetric flow of the mixture q_m.

Both properties, volumetric fraction and areal fraction add up to one regardless of slip conditions, as shown in equations 5 and 6.

$\lambda_{liquid} + \lambda_{gas} = 1$ Areal sum of fluid fractions in pipe diameter (Eq. 5)

$\alpha_{liquid} + \alpha_{gas} = 1$ Volumetric sum of fluid fractions in a pipe (Eq. 6)

If we consider a homogeneous flow, where both phases travel at the same velocities the liquid hold-up is equal to the liquid volume fraction and the gas void fraction is equal to the gas volume fraction. In the most flowing regimes, the slip conditions cause the liquid hold-up to be larger than the liquid volume fraction and the gas void fraction to be smaller than the gas volume fraction. These parameters can be used to calculate superficial velocities of the phases and develop an understanding of the flow regimes and their transitions (Corneliussen et al. 2005).

2.4 Multiphase flow-metering technology

As already introduced, the main objective of multiphase flowmeters is to quantify the fractions of the produced fluids, typically water, oil, and gas. The measurement of all fractions at once by only one individual device is not possible. In test-separator measurements the produced, fluids need to be separated before the quantification. Apart from different measuring technologies, various measurement philosophies with different levels of separation are in use. Transported fluids can be either fully separated into gas and liquids, partially separated, or in some cases, just a representative stream sample is measured in a sample line. All three options are well established in the industry and the final decision is made by the operator, typically based on technical, fiscal and economic regulations.

There is a huge variety of available technologies on the market focusing on the acquisition of different physical properties like density, velocity, or momentum. Others focus on capturing the physical effects that occur during the flow process. The eight most used flowmeter types are divided by the physical principle they are based on. For example, Instruments that quantify mechanical aspects like the force transmission of the fluids to vibrating tubes or turbines. Hydraulic flowmeters, which analyze fluid pressure losses or fluctuations. Instruments based on acoustic attenuation use sound wave sources to identify the fluid fractions. A few make use of electrical fluid properties like e.g. electrical impedance to analyze the induced voltage when a conducting fluid is passing an electromagnetic field. Less favorable, due to special handling requirements are these using radioactive sources, to analyze the attenuation and scattering effects of gamma rays. High potential is linked to recently improved magnetic resonance technologies that use the neutron interrogation of individual species and work perfectly for hydrogen bearing fluids like water, oil and natural gas. For the determination of water molecules, microwave emitting devices are used, which measure the attenuation of these and proved to deliver satisfactory results. Finally, a measurement principle that focuses on the evaluation of oil molecules within the stream and is often used for the water cut determination is infrared spectroscopy. Infrared light is hereby emitted and absorbed by the oil and bypasses water molecules and enables the calculation of the oil and water fraction. It is very common to use flowmeter combinations since each one of these is sensitive to different features and captures certain phases better than the other. For gas and general single-phase measurements, venturi type meters, which measure the pressure differential across a narrow pipe section, are very often used. To evaluate gas-liquid ratios gamma attenuation and neutron interrogation technologies are installed. Whereas water liquid ratios can be determined best using the electrical impedance and vibrating tube principles (Falcone et al. 2010).

Before making any decisions about the flowmeter type, one should think of which measuring philosophy is most likely to be successful and accurate enough for the desired application. Apart from separating the stream into its phases followed by separate measurements, one might try to mix the stream to reach a higher homogeneity. If the fluid stream is perfectly mixed the traveling velocity of the different phases can be considered equal. This principle reduces the complexity of the problem by eliminating slip effects. It is very likely that the velocities of the phases equalize but typically after the homogenizer the situation might change quickly, primarily due to the gravity impact. Therefore, the positioning of the measuring devices plays a crucial role. In measuring setups based on the flow homogenization, a combination of at least three different flowmeters is used. One for measuring the stream velocity or mass flow, second for measuring the mean density combined with the third to measure the gas-liquid ratio. Another flowmeter for cross-correlation might be added for precise phase fraction determination. A possible measurement combination could be e.g. a turbine or venturi meter for mass flow determination, neutron interrogation tool for water and hydrocarbon rates and a gamma type meter for gas-liquid ratios and mean density. Cross-correlated by conductivity measurement. This setup would anyway require prior knowledge about fluid densities and the chemical composition. Unfortunately, these dynamic properties might change over the lifetime of the well. It is then required to either find correlations to allow accurate fluid modeling based on characterization techniques or if these changes cannot be modeled accurately additional fluid sampling and analysis are recommended.

Since the accumulation of liquids and the potential of slugging across the flow-lines is hardly controllable three-phase separators require some stabilization time after they are filled or switched between wells, during well-tests. In contrast to a conventional single-phase measurement after a separation stage, MFM measurements are carried out more quickly and the real-time data can be analyzed immediately (Corneliussen et al. 2005).

2.5 Well-testing

Well tests are performed for well performance monitoring. It is a reliable source of information to identify production changes and implement optimization processes during the lifetime of the field. Trained operators in both, off- and onshore regions extract important information about the changes in production outputs and can identify unfavoured events. Based on findings from well-test results the company either decides to shut down certain wells, drill new wells, or reduce production rates by choking or turning down the pump-rate. Conventionally this information gathering process is done by simplified testing methods using vessels called test separators, where the separated fluid fraction is measured individually using Venturi, Turbine, or Coriolis meters. Test Separators are typically expensive, and the measurement time is long due to their specification, which requires stable flow conditions, for representative sampling. After the stream is directed into one of these vessels, it again requires time for the fluids to separate. Time might become a critical issue particularly in deep-water developments, where the installed flowlines are several kilometers long. If several wells are connected to one production manifold, as shown in Figure 3, wells can be switched to a testing manifold, where they can be monitored one by one without the need for shutting down all the other wells and avoid unnecessary production deferral or potential loss of production (Corneliussen et al. 2005).

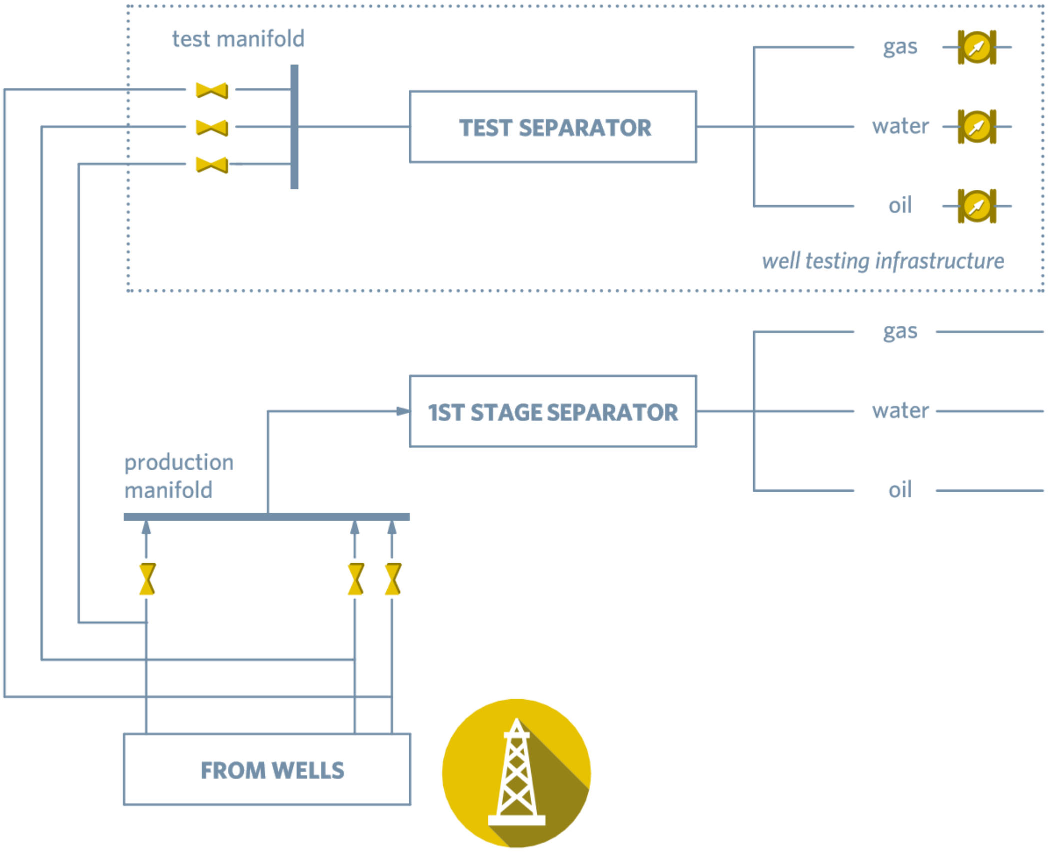

Figure 3. Conventional well-testing setup (Falcone et al. 2010)

With installed MFMs in the subsea-manifold, it is possible to save the expenses for separate flow-lines. A big plus to the operational mode of MFMs is the fact that these devices need less frequent interventions of special personnel and can monitor the well continuously and provide real-time data. Whereas, test separators with an accuracy between 5% and 10%, which is nowadays achievable with MFMs too, require regular intervention and provide only data from a narrow and sometimes unrepresentative testing window, which is then used for calculations until the next testing cycle is conducted (Falcone et al. 2010). Another disadvantage of conventional well-tests using test-separators is the performed shutdown, which might cause wellbore damages, pump disorders and as a result production losses. The next drawback of the conventional technology is that test-separators have a huge footprint and exert high loads on the platforms. A big issue in terms of continuous production might arise in wells that need to be tested regularly because they are prone to flow assurance problems and require more frequent work-overs to keep high production rates. Two typical MFM configurations could be used for well-testing purposes. The less complex option, shown in Figure 4, requires the integration of an MFM into a conventional well-testing infrastructure that can be used for back-up measurements, in case of a test-separator malfunction, or for validation purposes after a separator calibration.

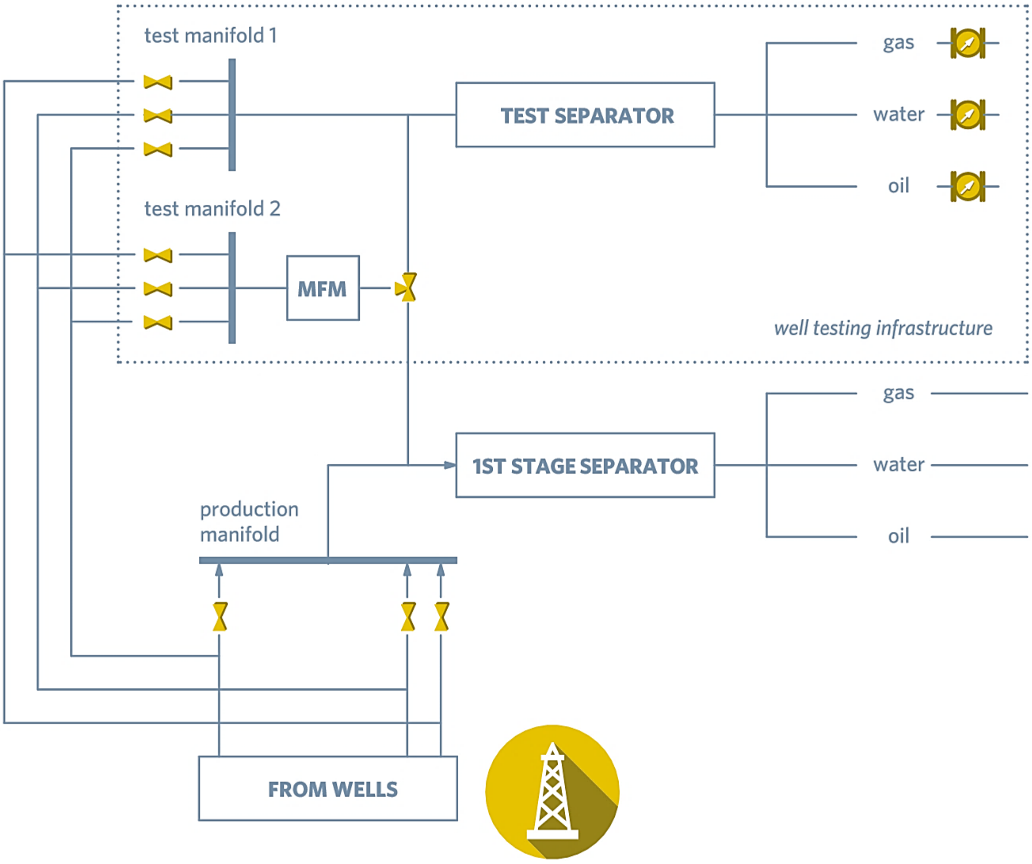

Figure 4. Conventional well-testing setup with integrated MFM
(Falcone et al. 2010)

This option does not contribute to a reduced footprint of the total system but allows continuous surveillance of individual wells while others are tested. Another measurement configuration uses a MFM as a single component without any additional instrumentation and is illustrated in Figure 5. MFMs might be used for well-tests on newly drilled wells and have proved to deliver satisfactory results without any fluid separation. The additional value is reflected in the improved control of the pressure drawdown and the reduction of required flow periods for testing (Corneliussen et al. 2005).

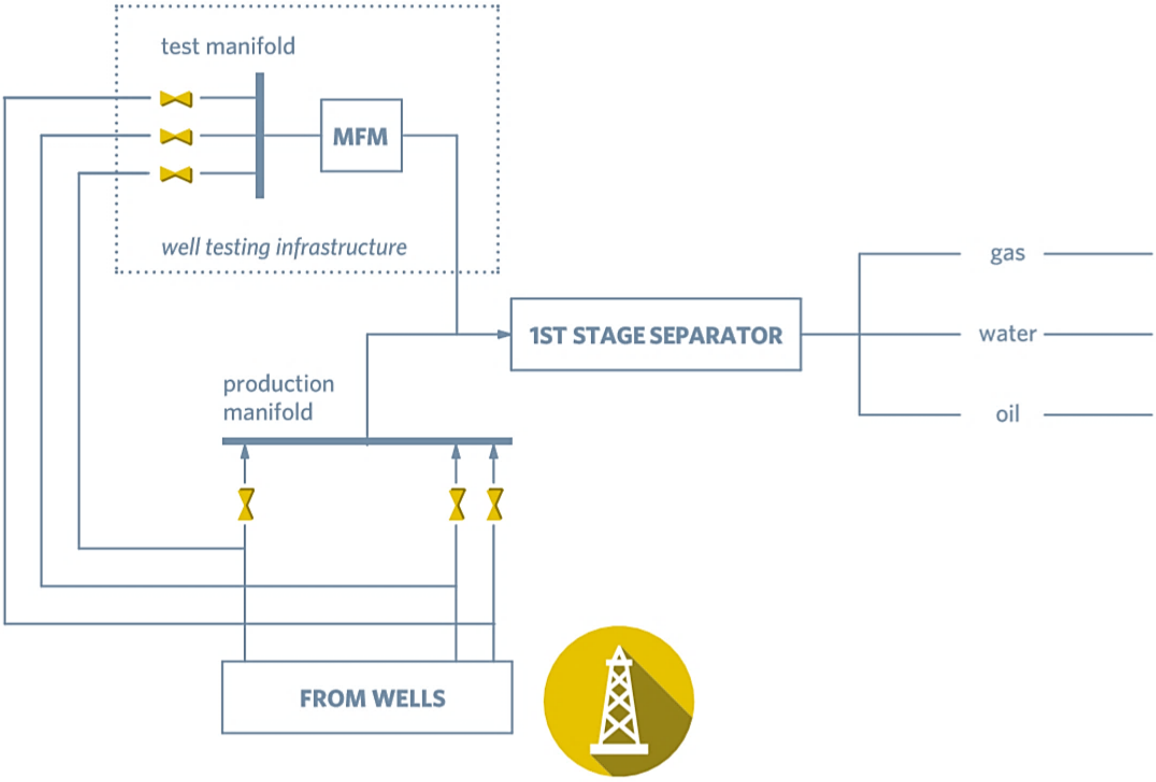

Figure 5. Well-testing setup based on MFM
(Falcone et al. 2010)

2.6 Production allocation

In every field where the production outcomes are split or shared between more operators, allocation measurements of individual wells belonging to one operator are required before the streams are commingled in one pipeline. It is typical in subsea operation to share transporting pipelines and processing facilities for total cost reduction. Many of the mature offshore fields e.g. in the North Sea would not be feasible without an existing infrastructure. Figure 6 illustrates an arbitrary production network of several independently operated wells connected to a shared separator facility.

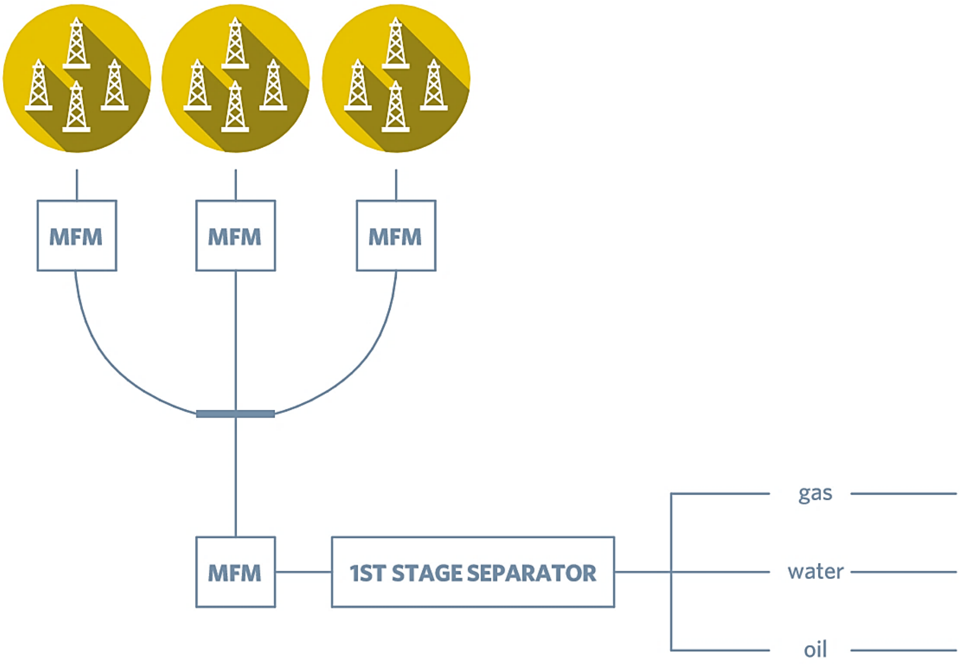

Figure 6. Possible measurement setup for production allocation and fiscal tracking (Falcone et al. 2010)

MFMs give particular advantages in remote offshore developments, where well streams of several operators are directed to a shared processing facility. Typically, before the outputs are mixed their produced hydrocarbon amount needs to be quantified to secure and allocate the produced amounts of each company. In this case, MFMs could replace cost-intensive sample lines and separators and the stream could flow directly to the shared measurement and processing unit. Apart from the advantage of direct output determination of each, so-called satellite field, operators can control and prove the quality concerning the contractual specifications of the host facility. Processing facility operators typically agree on certain amounts of impurities like solids, define maximum amounts of water or accept only gas with certain levels of CO_2 and H_2S. With a reliable measuring and real-time monitoring system, the well operator secures themselves from wrong accusations and legal consequences (Corneliussen et al. 2005).

2.7 Production monitoring

Real-time monitoring of outputs is a crucial and highly desired approach for many companies. It is required to reduce production costs and increase the feasibility of technically demanding fields. Monitoring technologies are incorporated in the general process of digitalization in the oil and gas industry and are a successful way to optimize upstream operations.

The main target is to monitor and control the performance of producing wells. These systems allow to track and identify different operational modes of the downhole system based on the transmitted data. Downhole data like pressure, temperature, or acoustic vibrations are used to identify and predict changes in the fluid compositions and flow rates. By combining this information with historical production data, gathered over the lifetime of a field, outputs prognoses and improved production strategies can be implemented. Historical data can be compared with future forecasts and check their probability based on the reservoir deliverability. Apart from understanding the thermodynamic reservoir specifications for successful reservoir management the monitoring of installed production devices is crucial for securing the desired production outputs. This is closely linked with accurate intervention and logistics planning. Every intervention that is not predicted is causing more downtime than it normally would if the possible malfunction would have been detected in advance. Different records of the production system depending on the completion and installed facilities are taken. In wells with e.g. installed ESPs, different types of failures can be avoided by looking at intake pressure and the motor winding temperature. One of the reasons why both tend to increase is scaling. Combining these readings with the aquifer chemistry of a well prone to form precipitates further adequate operations can be utilized. It is possible to have an autonomous decision-making algorithm that recognizes the danger of scaling and after surpassing a programmed threshold value of intake pressure and motor temperature, a chemical injection line is activated and allows scale inhibitors or any other additives to flow downhole. This is how quick decisions can be made from translated data records (Unneland und Hauser 2005). Real-time production monitoring is therefore very important for measuring actual and forecasting future outputs, predict failures, plan interventions, and update numerical models for improved reservoir management.

2.8 Reservoir management

Reservoir management is by definition dealing with the allocation of resources to optimize hydrocarbon recovery and minimize capital and operational expenses. These two sides often stand in contradiction and the overall process of optimization is a compromise between maximized recovery and economical efficiency. The investigation of the possible conflicts and outcomes between those two objectives is the main target for the field-operator. An important tool in reservoir management is reservoir flow modeling used to create production forecasts. These developed models typically plot the production rates as a function of time. When the resource price including market volatility is added, future cash flows can be predicted. These estimates are important for stakeholders and are used to calculate and compare the values of different developments. There are different modeling concepts, each technique estimates different results so the detailed approach of every economic evaluation should be known before comparing two different projects with each other.

An important tool for estimating the remaining reserves and calculate the production forecasts are given through MFMs. Thanks to real-time, continuous production data delivery operators can better judge on the reservoir performance. Whereas traditional test-separators delivery only discretized information on cumulative volumes. Figure 7 shows a possible arrangement consisting of MFM for continuous reservoir management (Corneliussen et al. 2005).

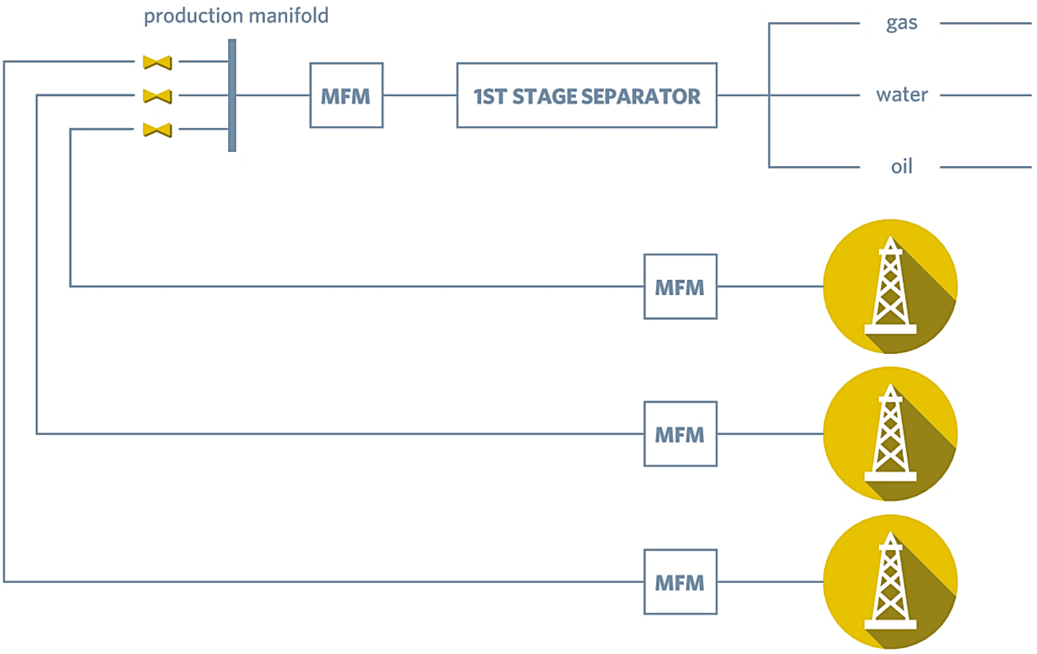

Figure 7. MFM setup for reservoir management
(Falcone et al. 2010)

2.9 Reserves estimation

Reserve estimations are conducted to rate discoveries and update the reserves of fields already in production. In new developments, reserve estimations are based on the data derived from seismic acquisition and geological interpretation of the petroleum system. Typically, point information from wildcat wells like e.g. cores or logging data is available to solidify the knowledge gathered from surface-based measurements. If the reservoir model consisting of net formation thickness, reservoir size, porosity, and saturation is set up, first estimates of the hydrocarbon initial in place can be conducted. For the evaluation of the reservoir volumetrics highly sophisticated data analysis methods using statistics and geo-statistics are used to correlate properties and fit their characteristics to their sedimentary history. After first production tests the drainage area, reservoir height, skin, and permeability can be derived and checked with predicted values. This data is then used to calculate the reserves, estimate recoverable resources and their economic value. Another important factor in estimating the recovery factor and the total recoverable hydrocarbons is the driving mechanism of the petroleum system. Having first estimates on all of these properties allows one to transfer the data into a numerical software to monitor and predict developments on the field scale. Typically three different cases P90, P50 and P10 are derived to perform a risk analysis and estimate the possible chance of success. These cases describe the level of confidence or the probability of 90%, 50% and 10% of recovering the estimated amount of hydrocarbons, respectively. These static models need to be updated over time when fluids are produced from the reservoir. These numerical models are described by conservation laws and are fundamental for building a link between the dynamics of the system and its physics. Modeling of the dynamic behavior of a reservoir system with various changes in temperature, pressure, water cut and gas oil ratios over time is challenging and requires a very good understanding of the local geology, reservoir chemistry, and thermodynamics (Gandhi und Sarkar 2016)**.** The typical process of approving a model consists of matching the current behavior to history readings. History matching is a commonly used phrase that describes the process of fitting the actual dynamic model to the past behavior of the reservoir. It is difficult to model such systems based on discrete-time information from test-separator measurements. A big advantage is brought by MFMs which measure the outputs continuously and allow to forecast hydrocarbon production and estimate ultimate recovery. However, the fluid metering operation is not error-free. There are different levels of acceptable accuracy, depending on whether they are required for fiscal, allocation, or reservoir management purposes. In the case of reserves estimation, an accuracy of 10% for measured outputs is generally considered to be acceptable. The metering accuracy is particularly important for smaller discoveries, technically demanding field or marginal fields, where the results of inaccurate predicted reserves and recovery factor can meaningfully impact the total project economics. Since the results from production measurements are implemented in the reservoir modeling process, the levels of uncertainty that are accepted depend on overall field reserves, market price, predicted production time and other relevant aspects (Corneliussen et al. 2005).

2.10 Fiscal and custody transfer measurements

Offshore field operators typically use the available infrastructure like processing facilities or transportation pipelines to reduce the overall development costs. If there are none of these available it is required to compensate for their lack on own expenses. In many well-developed areas like e.g. the North Sea in the United Kingdom or the Dutch part of the North sea, production streams of more independent licenses are often commingled into one shared processing facility or flow line. It is necessary to quantify the production from each well or at least from each operating company to track their production outputs. The importance of direct and continuous metering is highlighted again since it is a useful measure to allocate the commingled streams to their owner's and is also required to calculate the financial obligations and expected revenues. A visual representation of a possible sharing setup is pictured in Figure 8.

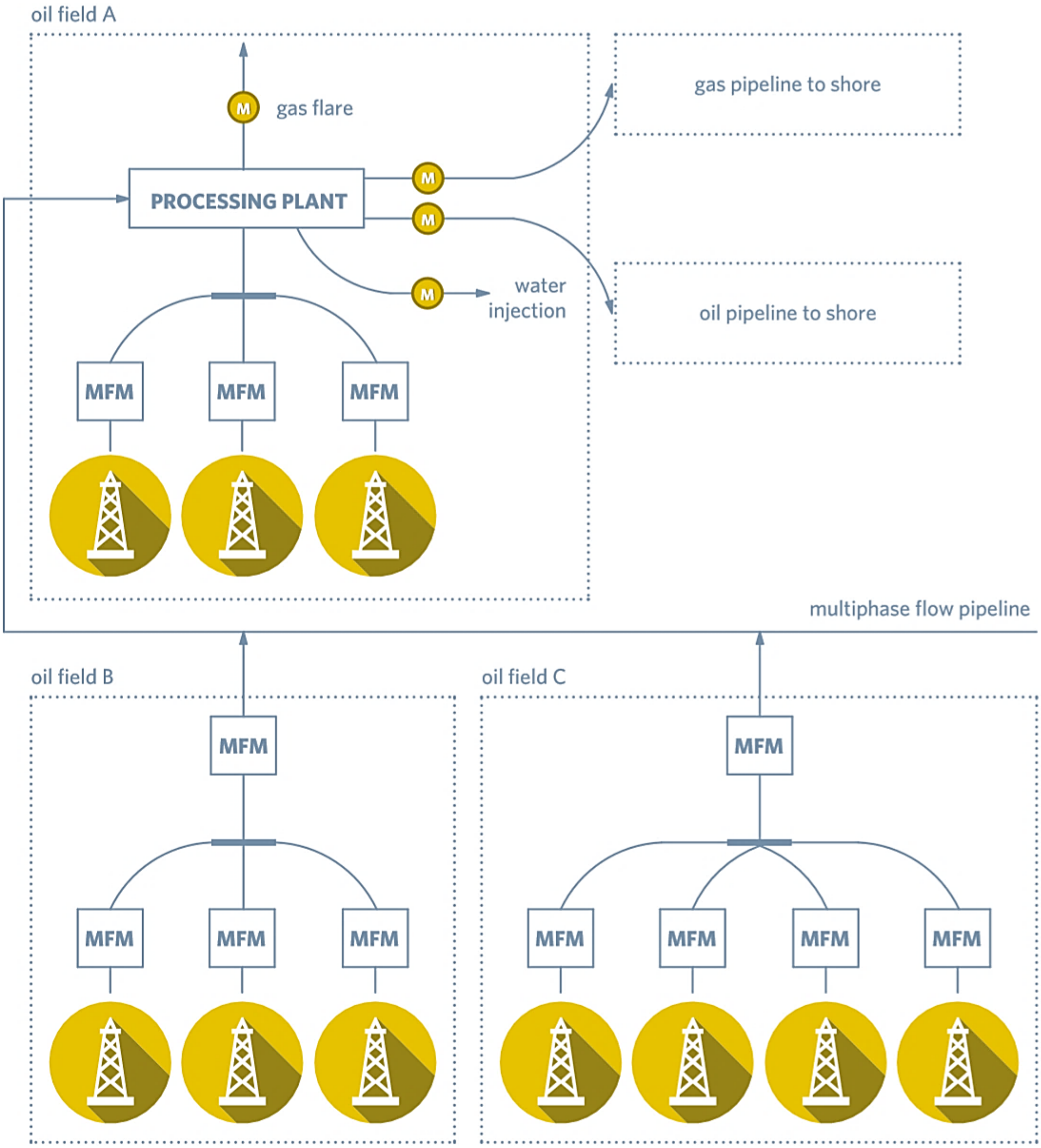

Figure 8. Multiple-field cluster
(Falcone et al. 2010)

The measurement methodology and required accuracy are clearly defined by national metrology standards like API, AGA, or ISO and need to be documented and reported transparently by each operator. The obligation of detailed documentation is often extended to other operations like chemical injections where the amount and environmental compatibility need to be assured. All of these measures are used in the final reports for the fiscal and custody transfer regulations. These documents are the guarantee for money transfer, either between companies or companies and the government. Any error in the fluid measurement will be reflected in an error of the corresponding money transaction. “*Whether it is oil, gas, or chemicals, a tiny error of even 0.25% in the flow measurement of materials being transferred can cost a company millions of dollars in one year. A very large custody transfer system can meter $6,000,000 worth of natural gas per day or $2.2 billion per year. If the measurement is off by 0.25%, that’s an error of $15,000 per day or $5.5 million per year in somebody’s favor*” (Emerie Dupius and Gerrard Hwang 2010). Controlling has the highest priority for each operator to assure accurate measurements and sufficient documentation to prove the origin and amount of the produced hydrocarbons (Corneliussen et al. 2005).

3 Virtual flow meter (VFM)

Worldwide there are two industry-accepted solutions for providing fiscal and custody transfer measurements. It is either by using test separators or using multiphase flow meters. Both approaches require hardware installations (Corneliussen et al. 2005). This can limit the applicability of physical metering devices due to arising transportation issues, space considerations, or cost limits. A virtual flow meter is a mathematical model that allows estimating multiphase rates using available data on the flow route. A VFM primarily uses readily available cheap measurements such as pressure and temperature data and can potentially serve as a cost-efficient addition to physical flow metering devices. VFM models can be classified as mechanistic or data-based models. In mechanistic models, data and the unknown features are typically linked by solving a partial differential equation, derived from conservation laws valid for flows in a pipe geometry. This methodology requires the selection of an appropriate numerical method, properly set boundary conditions and the access to continuous time-dependent input parameters. A very interesting feature of this method is that the results of desired properties can be calculated at arbitrary points of the flowline, as defined in the model (Amin 2015). The data-based methodology can be used as an identification tool for different operation modes. Nowadays, flow prediction based on recorded data interpretation is used as backups for physical flow meters. These recorded features, when modeled accurately, can identify any change in operation and can be translated to changes in the flow quality and quantity. These models don’t require any additional knowledge about the system but are based simply on available data records. The challenging part in setting up this kind of VFM is the need for extensive data amounts, ideally historical, system-specific data records. Practically data-based models are easier to set up than the mechanistic ones but don’t explain the physics behind the occurring events. Nevertheless, data-based VFMs are a matter of intensified investigation and are seen as potential standalone measuring solution (Jan et al. 2016) (Andrianov 2018).

3.1 VFM types

As previously described the VFM systems can be separated into two main categories namely mechanistic and data-based models. Mechanistic concepts are the most widely used types of VFMs in the industry. The reason why they are the most frequently used system is the deep level of expertise that was developed over the last 50 years of investigation in the area of virtual metrology. Good results could be achieved due to well research and understanding of the individual mechanistic models, which combined reflect and allow the prediction in certain production systems. Currently, the leading virtual flow metering systems consist of several individual models that are combined depending on the production system characteristics.

- Reservoir fluid model
- Reservoir inflow model
- Thermal-hydraulic model
- Choke model
- Electric submersible pump (ESP) model

The main idea behind the mechanistic VFM system is to link different types of models and generate a combined solver that delivers system variables like pressures and temperatures along the flow path. For this purpose, It is necessary to create a PVT profile that fits the produced fluid properties and is adapted to the conditions to which they are exposed during uplift. Using a data adjustment algorithm, the model data are adjusted to the physical measurements. Parameters like flow rate, discharge and heat transfer coefficient or slip properties are adapted such that the model outputs, match the measured pressure and temperature records and obey the conservative laws like e.g. the material balance equation. A typical mechanistic modeling approach can be summarized within the following steps (Bikmukhametov und Jäschke 2020):

1. Create a fluid properties model: Black Oil, Composite, Equation of State
2. Pick production system model based on available measurements: e.g. ESP model
3. Data cleansing and validation: Remove outliers and filter noise.
4. Decide on tuning parameters: flow rates, choke discharge, heat transfer coefficients.
5. Initialize model, with random parameter values from step 4.
6. Simulate the models selected in step 2 using the fluid model in step 1 and initialization input from step 5.
7. Select model outputs from step 6 according to available measurements in step 2 e.g. intake, discharge pressure, and wellhead temperature, etc.
8. Run the adaptation algorithm to minimize the deviation between model results in step 6 and the validated data in step 3 by adjusting the tuning parameters from step 4.
9. Present results after checking their plausibility

Many of the VFM technologies are based on the working principle described in the steps from 1 to 9. The vast majority of the commercially available models are incorporated into commercially available software. They slightly differ in their modeling approach, implemented solver types and are not universally applicable. The available solutions have many similarities in structure, input data requirements and all of them work best if the simulation engineer understands the specifications of the system to accurately adjust fluid properties and the production system model to estimate the dynamically changing flow rates. Well established and widely incorporated systems are provided by Schlumberger, Kongsberg, FMC, ABB, or

Roxar. The PETEX Group e.g. provide Prosper, which is not a fully integrated VFM system since it is not able to fit model data to the respective physical measurements. Nevertheless, it can be used for flow predictions since the system contains different fluid and flow-system models, capable of executing complex production performance analysis (Amin 2015).

3.2 Principles of data-based models

VFMs based on collected field or experimental data are generally easier and cheaper to generate since they don't require additional hardware installation or specific production engineering knowledge. The biggest challenge is to sort, filter and validate recorded data and create a mathematical model that reacts and on the changes in the input data and accurately predicts the desired outputs. The biggest advantage of this modeling approach is the missing necessity of a precise system and fluid model description. No flow path geometries, friction, or temperature-related parameter are required. No prior knowledge of the governing system and physical specification is needed. Any desired function can be solved by the so-called machine learning approach. Machine learning is not particularly new technology, but it becomes more important especially due to the increased importance of recording, collecting and storing data from measurable quantities. Companies are recognizing the huge potential of information that can be extracted from monitoring activities. It was first the ability to cheaply measure and secondly the access to the required computational power, to finally process and validate this huge amounts of data, that pushed the development of data-based MFMs significantly (Hastie et al. 2017).

In machine learning, the process of fitting the model to available data is often referred to as training. If the model is trained properly and the system dynamics are within the range of the input data used for training, data-based models can accurately predict the desired outputs in real-time. The model will not perform satisfactorily on data that were not within the training range. That's why adapting and tuning of the model with data from different operating modes increases the accuracy of flow metering. Different from mechanistic models, where the conservation laws are often solved in their dynamic, time-dependent form, most of the data-based VFM models are solved by steady-state algorithms. There are systems based on a dynamic problem formulation, where the output from previous time steps influences the flow rate prediction at current time steps. Typically, these models use a solver that allows finding one solution in time or takes the solution from the last step as initial input for the flow rate calculation in the current time step (Perkins 1993).

3.3 ESP data-based model

The idea of modeling a production system based on its completion is desired since the already installed sensors, required for system performance analysis, can be used as input data for a data-based model. ESPs are widely used artificial lift systems, which proved to work in many different production fields. ESPs work excellently for on-and offshore applications, have a fair capability of handling solids, gas and have the highest operating range in terms of production output from all artificial lift systems. ESPs are limited by high temperatures, abrasive solids and high viscosity fluids which increase the unit's power requirements. Therefore a reliable source of electric power on the surface must be available. For high operational flexibility, a variable speed drive is recommendable alternatively choking of the production at the wellhead is possible to adjust the operational range. Generally, ESPs run on a constant frequency therefore their design and capacity must be based on reliable inflow-data and matched with the systems deliverability. Artificial lift equipment is typically installed if the natural lifting capacity of the reservoir is too weak to produce fluids to the surface in a feasible manner. Common reasons are low bottom-hole pressure, liquid loading, or highly viscous fluids (TAKACS 2017). When setting up an ESP model the main target is to link the pump pressure records together with the power and current consumption. The idea is to match the records with the flow rates in real-time. With the properties measured at the pump and additional records along the flow path, multiphase flow mixtures that are produced by the ESP can be computed. To create the model the individual fluid fractions pumped through the system must be quantified. If the model input properties are collected and their outcome in terms of flow rates is known, the desired multiphase stream can be modeled without any prior knowledge about detailed system physics. The flow rate measurement required for the model can be utilized differently. One option would be to use data from a well-test performed by three-phase separators using single-phase meters. The second possibility is to use physical MFMs. If a VFM model is designed based on measurements from physical MFM it can be used as a back-up system for flow monitoring and control. The position of the MFM is significant. If the installed hardware is measuring the output of one well the VFM-model can be used as a back-up system for the MFM in case of a malfunction. If the MFM is installed at the end of a comingled well grid and the VFM is trained from its records, it has the potential to be used as a standalone solution. Similar to a test-separator installation. The modeling process can be divided into three main steps. Data collection, Data processing, and model creation. The data collection setup in the field can be similar to the one illustrated in Figure 9.

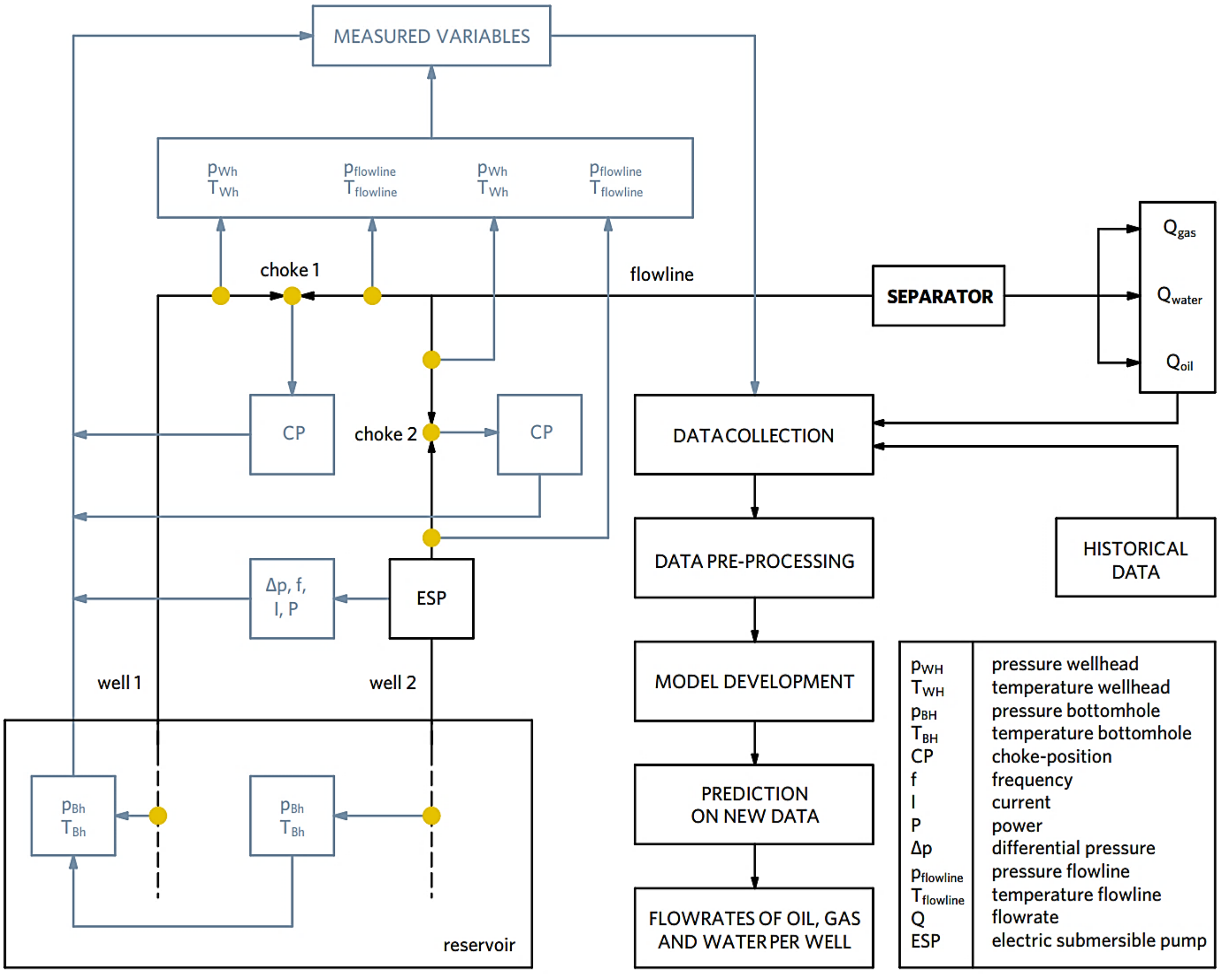

Figure 9. Possible measurement arrangement for data collection (Bikmukhametov und Jäschke 2020)

This figure illustrates the measured variables like e.g. bottom hole pressure and temperature, wellhead pressure and temperature, ESP readings and the flow rate output. In this case, the measured water, oil, and gas rate are combined with historical data to feed the artificial neural network (ANN). Before feeding any network, the data need to be processed. In processing, the data-sets are filtered and cleaned from noise and outliers. In a steady-state modeling approach, time-dependent data should not be utilized. Finally, model creation consists of the learning, training and validation steps. The learning process is performed on a defined portion of data and creates the solving algorithm. A mathematical function that tries to fit both the training and testing data accurately. The mathematical relation between the input and output data can be a linearized multi-regression model or a more sophisticated artificial neural network. In the training process, this algorithm is improved and tuned with additional data. Finally, the model is tested with the third portion of the data. If the validation-error of the model is satisfactory the algorithm is tested on newly acquired data it has never seen before. The importance of this step in terms of model generalization will be a matter of the following section (Bikmukhametov und Jäschke 2020).

4 Artificial neural network (ANN)

The theory of artificial neural networks consists of various architectures, learning methods and system classes. They differ in their solving approach and have different underlying theorems but all of them have a common source of inspiration, namely biological neural networks known from brains. The special fact about ANNs is that they can compute any functional dependence between input and output. This ability is described by the universality theorem. It does not matter if one wants to use ANNs for image recognition or translating a text from one language into another. All of these processes can be described as a function and are solvable due to the learning ability of ANN and their universality (Nielsen 2019). In the theory of neural networks, the governing objective is to find a mathematical relationship between the input features and the output variables. A visual representation of an arbitrary neural network is shown in Figure 10.

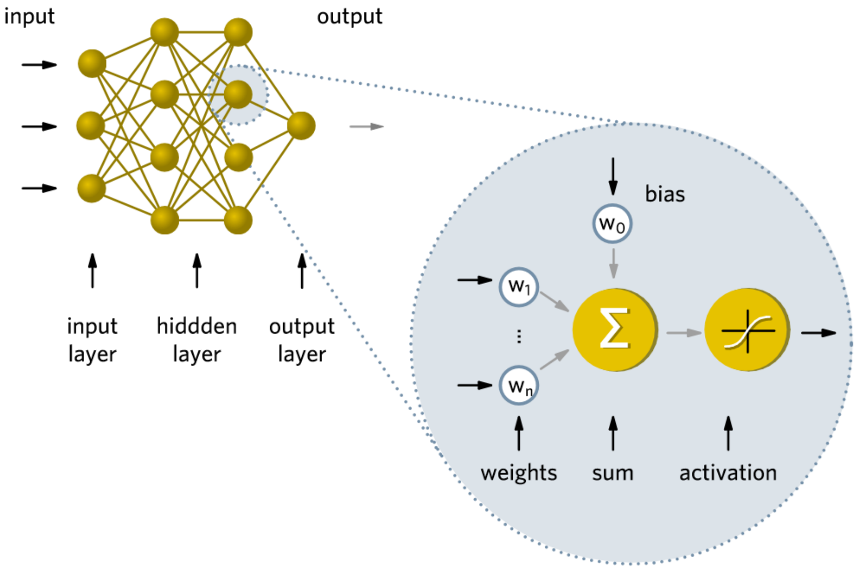

Figure 10. Artificial neural network example
(Fruhwirth 2019)

All ANNs consist of an input layer. The input layer is the first layer of a network where the measured input data from experiments or historical data is inserted. Every inserted data type represents a network feature. Any recorded feature or physical parameter represents a node which often refers to as an input-neuron. Similar to the network in the human brain, neurons in artificial networks are also interconnected. The connection type and density differ depending on the model architecture. Neurons of the input layer are connected with neurons of the following layer but are typically not connected within the same layer. Connected cells between two layers have a connection path which is represented by a weight factor. The weight factor describes how strong the previous neuron will affect the output in the current one. Typically the neuron networks are structured in a layered way. That means that all of the neurons in the input layer are connected with neurons in the second layer, a hidden layer. A network can have various numbers of hidden layers but it does not guarantee network A, to be more accurate than a network B with fewer layers. The objective is to find the optimum number of hidden units and layers at which the output satisfies the desired prediction accuracy. The last layer in a network is called the output layer. Systems with more than an input and output layer are defined as multilayer perceptrons. A perceptron or neuron is a linear classifier that uses a linear function for solving a prediction problem. Perceptrons, calculate the output based on the input value multiplied by its assigned weight, as shown in Figure 11.

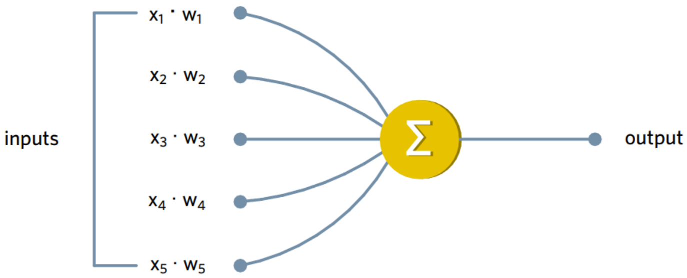

Figure 11. Perceptron scheme (Missinglink.ai 2020b)

The weighted sum of all inputs in one layer is called the local receptive field. If no hidden units are introduced, the network is a multi-linear-regression solver. Hidden layers are introduced since they are the spots in the network where non-linear relationships between the input and desired output are created. Results in the hidden layers are sent through an activation function. This activation function can be both linear and non-linear. There are many well studied and frequently used activation function like e.g. ReLU, TanH or Sigmoid, which can have a binary, percentual, or a more complex response which drives the activation of an output neuron. All of the activation function parameterize the output and regulate the influence of the output neurons on the final prediction result (Missinglink.ai 2020a). Activation functions help to generate output values within the desired range, and their non-linear form is crucial for the learning process. For VFM application, differentiable activation functions that introduce non-linearity proved to work well in predicting flow rates (Bikmukhametov und Jäschke 2020).

After each learning step the algorithm computes the minimum error between measured and precited variables and is adjusting the weights during the backpropagation process. Backpropagation is a learning algorithm and will be part of the following sections (AL-Qutami et al. 2018). The feed-forward type of neural networks, without any recursive or circuit connection between features and variables, has been frequently used for VFM applications because of its excellent ability to approximate any relationship between features and flow rates. The challenge in using these models is the transient behavior of fluids when flowing through pipe conducts. Feed-forward networks are not capable of identifying temporal relationships in the data. There are currently models in development based on recursive neural networks (RNN) which are using internal memory and remembers the relationship between inputs and outputs and combine the current weights based on the previous time-step. One of the first described examples for modeling multiphase flows with VFMs was performed by Qiu and Toral in 1993. The laboratory-based model used pressure readings to predict a two-phase flow of liquid and gas using a feed-forward network (Shoeibi Omrani et al. 2018).

4.1 Methodology

Before modeling the VFM, the collected data from the flow system must be analyzed before starting the learning process. In data processing, the data is filtered from noise, outliers, unwanted and partially missing readings. It is also possible to combine reading results forming new features. The term often used for input data preparation is feature engineering. Some typical operations are e.g. scaling, binning, feature imputation but most importantly visualization. Scaling is recommendable if the input features show a high deviation in their ranges. It might be difficult for an ANN to compare these features, so a solution might be a normalizing or standardization step. In binning, data is separated into different bins according to the desired property like recording time or range. This process allows to smooth out the data, eliminate outliers and reduce the risk of overfitting. It also might be necessary to complete some missing records, this is possible with feature imputation. In continuously measuring application a time derived mean or median input might be used. Without any doubt, an initial visualization of data is very much recommended. Visual inspection is an important instrument to analyze data, predominantly to identify outliers but also to plan further processing measures. Another very useful measure in data processing is feature projection which is used for the complexity reduction of an ANN. This is possible by switching from higher-dimensional space to a lower-dimensional space. It is a significant step for model generalization. Important is that the network requires ideally only as many dimensions as the problem produces. On the one hand in case of solving the task with a higher-order network, noise might be modeled. Introducing the so-called overfitting problem. On the other hand, if a higher dimension problem is solved by a lower-order solution network, the system will be under-fitted. Several techniques are used for dimensionality reduction like for instance, Principal Component Analysis (PCA). In PCA a large set of variables is transformed into a smaller set of principal components that still contains most of the information. Practically, the best fitting linear approximation within a data cloud is evaluated by calculating the minimal quadratic sum of all errors between the data points and the linear function. For two variables the principal components are shown in Figure 12.

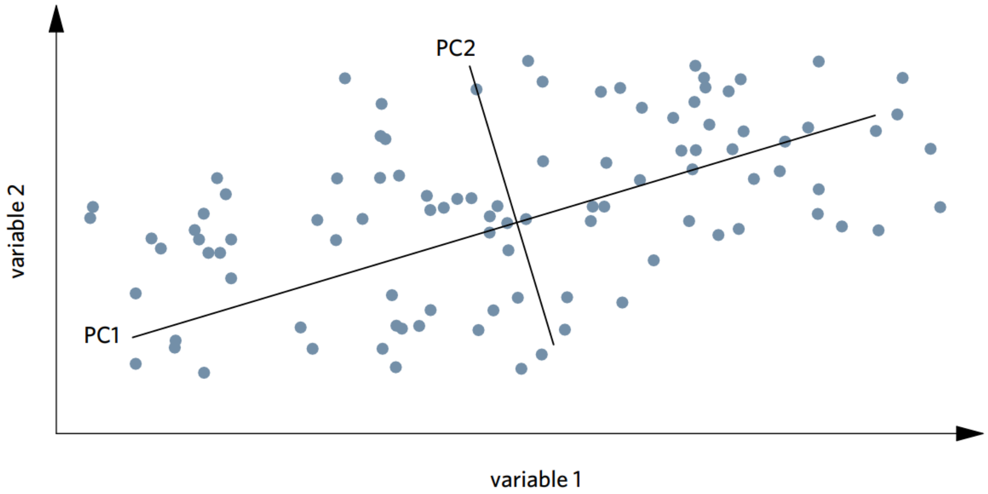

Figure 12. Principal components for two arbitrary variables (Jaadi 2019)

If more variables are used a covariance matrix is created which allows to evaluate principal components, by solving the characteristic polynomial. With this method, linear dependencies between the input variables and the principal components are evaluated by calculating the eigenvectors of the covariance matrix, which describe the direction of maximum data dispersion. Eigenvectors define the axes where the most variance, therefore most information is captured. Eigenvalues are the measure of the introduced variance and are expressed as principal components. Where, the first principle component PC1 describes the biggest variation in the data, the second principal component PC2 the second largest and so on. The number of principal components is equal to the number of input variables of the covariance matrix. Typically, a few principle components are enough to describe the majority of the variance in the system. To calculate the percentage of variance introduced by each principal component, one needs to divide each eigenvalue by the sum of all eigenvalues. A typical graph summarizing the captured variance with respect to the principal component is shown in Figure 13.

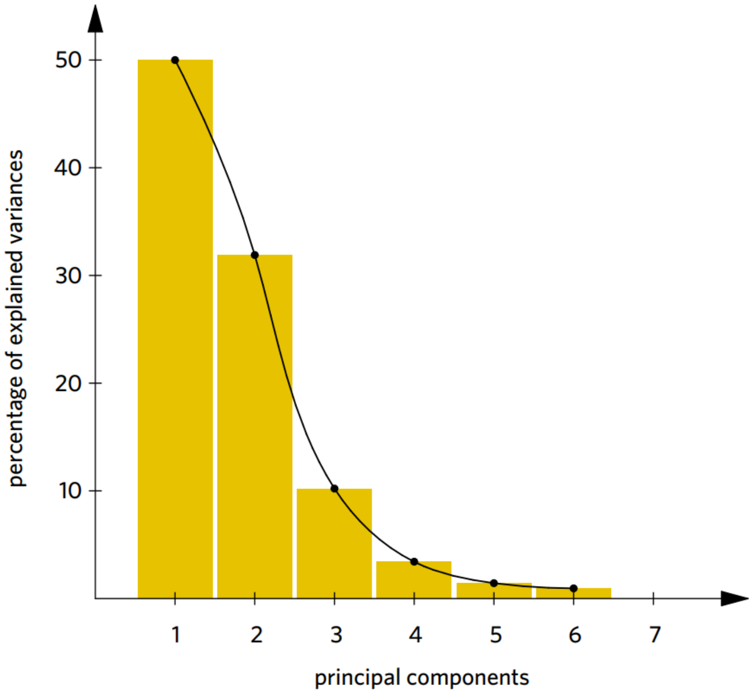

Figure 13. Variance with respect to principal component plot (Jaadi 2019)

In Figure 13 one can see that the first principal component explains 50% of the variance and the second around 33%. That means that one could reduce the dimensionality from 7 variables to 2 principal components and still capture 83% of the variance introduced by the data. (Jaadi 2019).

Another commonly used method for data reduction would be a sequential forward selection, where the desired output is predicted using only one input variable. This process is repeated with all features, and the feature with the lowest validation error is chosen to be combined in the next round with all features individually. The combination of two features with the lowest validation error is then carried into the next iteration step and again combined with all remaining features. These steps are repeated as long as the validation error is being minimized. The main idea behind data processing is to reduce the amount of redundant data and in projects were huge data amounts are processed, for lowering the required computation power during learning and training. The vast majority of VFM projects described in the literature use raw sensor data, therefore space for improvement in terms of feature engineering in VFM applications is still available (Bikmukhametov und Jäschke 2020).

4.2 Modeling strategy

The model development starts after data is being processed. In this major step, the final algorithm that correlates the outputs to the inserted features is developed. The modeling process consists of two main operations, learning, validation and testing. For this purpose the incoming data is divided into three respective subsets, using 60% for learning and 20% for each validating and testing. The percentages are set accordingly to the dataset size. For small to medium datasets the earlier described selection is recommendable. In the learning process, the input data is inserted and an arbitrary initial solution is estimated. The predicted value is compared with the measured solution and conventionally the mean squared error (MSE) is calculated. Ideally, if the data shows no or little outliers. Alternatively, a minimum absolute deviation (MAD) might be implemented which is not sensitive to outliers. The error calculation between predicted and desired values is the starting point of the error-backpropagation algorithm which is performed with the learning and validation subsets. Equation 7 shows the minimum squared error.

$$E = \frac{1}{2}\sum_{i}^{N} \left| y_{predicted,i} - y_{desired,i} \right|^{2} \qquad \text{(Eq. 7)}$$

This function is often denoted as the cost-function or error-function, E and the target is to minimize it by adjusting the network parameters. To understand how the system adjusts these parameters, it is required to understand how the predicted values are calculated and what parameters the system adapts during the learning process. Mathematically, it means that one needs to find the minimum of the error-function. The parameters that influence a neural network are the input that is measured and the weights, w that are assigned to every connection path between two neurons in neighboring layers. The neural network is initialized with randomly picked weights and updates them in every learning step. To avoid the risk of trapping in local minima, multiple experts are trained in a single cluster simultaneously. The initialization weights are different for each expert and the best performing expert is remembered by the model. The learning algorithm consists of two steps, the feed-forward and backpropagation step. In the backpropagation step, the weight is adjusted accordingly to the gradient of the calculated error-function. The gradient is defined as the change of the cost function with respect to the particular weight and is visually represented in Figure 14.

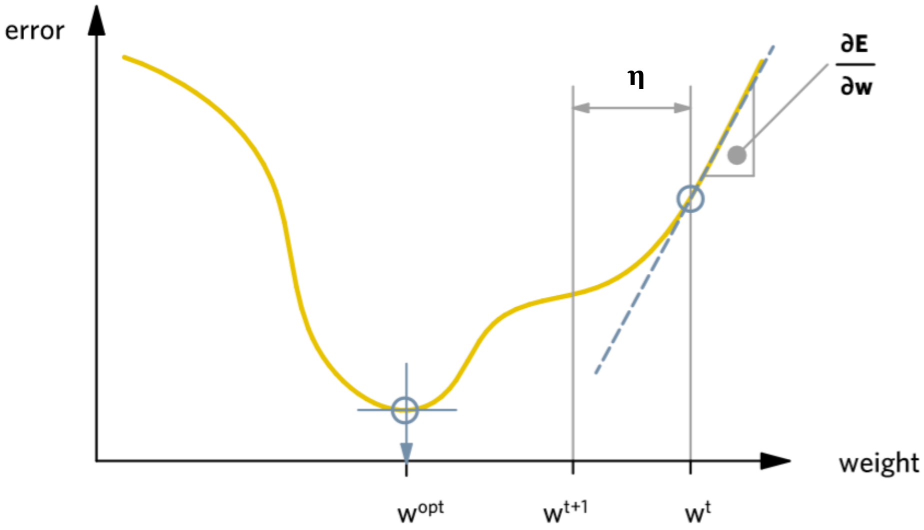

Figure 14. Illustration of the error-function minimum estimation (Fruhwirth 2019)

The step size by which the weights are increased or decreased is controlled by the learning rate, η. Small learning rates will lead to accurate results but the computation time might be technically unacceptable, whereas using too high learning rates might result in missing the error-function global minimum.

An improved approach refers to as adaptive learning, which updates the learning rate η, according to the cost-function gradient, $\frac{\partial \mathrm{E}}{\partial \mathrm{w}}$ for every weight individually and is shown in equation 8.

$$w_{\mathrm{t}+1} = w_t - \eta(\mathrm{t})\frac{\partial \mathrm{E}}{\partial \mathrm{w}} \qquad \text{(Eq. 8)}$$

A positive gradient reduces weight, w_t whereas negative gradients increases it. This process is repeated for all the neurons in the network propagating back to the first weights assigned to the input layer. With the updated weights a new feedforward process is started. The weights are adjusted again and a new output for each perceptron is calculated. One neuron output can be described as the weighted sum of all inputs and their weights from the previous layer. The output of the current neuron is used as input for the next layer, consisting again of weights, multiplied by the input and a bias. The weighted sum is then sent through an activation function, which decides whether a neuron is activated or not. The bias is a special weight type that allows one to move the activation-function to left or right and is typically initialized with 1 and further trained within the model. The effect of a changing bias on the activation function is shown in Figure 15.

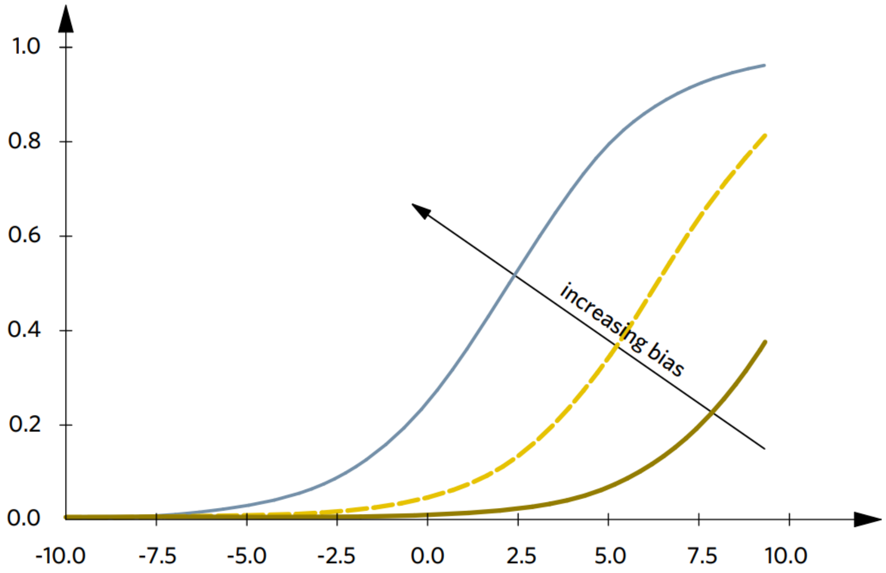

Figure 15. Effect of bias on activation function (GeeksforGeeks 2018)

With increasing bias, the triggering values decrease, which helps in controlling the activation function. Although, a bias is not necessarily required in ANNs their importance in terms of the bias and variance trade-off, will be explained later in this chapter.

The learning process is repeated until the error-function minimum is reached. Since the modeled problems introduce a high complexity and their approximation is time-consuming a frequent solution is the introduction of stopping criterions which are divided into inferior and superior types. Stopping criterions are used to prevent the network from overtraining and save computation time. It may happen on the cost of overall accuracy but the solution should be as accurate as required and also computable in a technical relevant time frame according to required standards. The computation can be stopped after a certain amount of training epochs or by setting the desired threshold-error by defining the inferior stopping criterions. Superior stopping criterions are based on either error fluctuation, time-controlled early stopping, or generalization loss. All these features can be used to control the quality of the network. The monitoring of generalization loss is done by plotting the error-function against the training epochs. If the monitored error increases after reaching a minimum it is typically a sign for modeling noise and refers to as overfitting. Generalization is a significant measure that describes the ability of the model to make accurate predictions based data it has not been trained on (Bikmukhametov und Jäschke 2020). After the learning period, the model needs to be validated and is therefore tuned with a different data subset. The main purpose of model validation is to control the generalization loss. Another reason for validating the network is the ability to improve the selected hyperparameters. Hyperparameters are set before the training and regulate the network size and neuron connectivity. Adjusting them allows changing the number of layers and the number of neurons in each layer. Figure 16 and Figure 17 demonstrate what features can be observed when plotting the error against the training epochs.

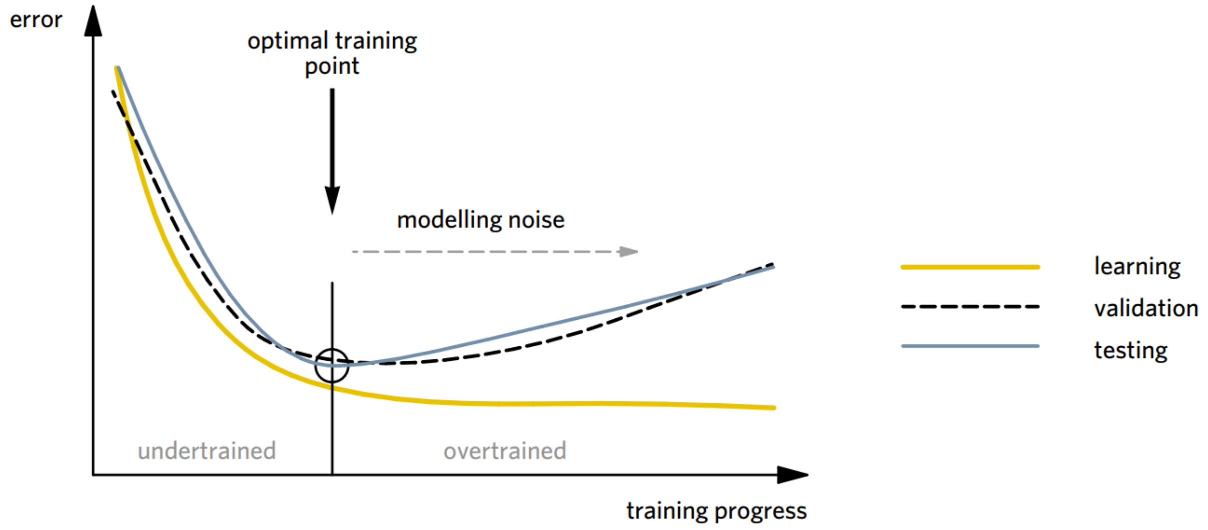

Figure 16. Noise modeling
(Fruhwirth 2019)

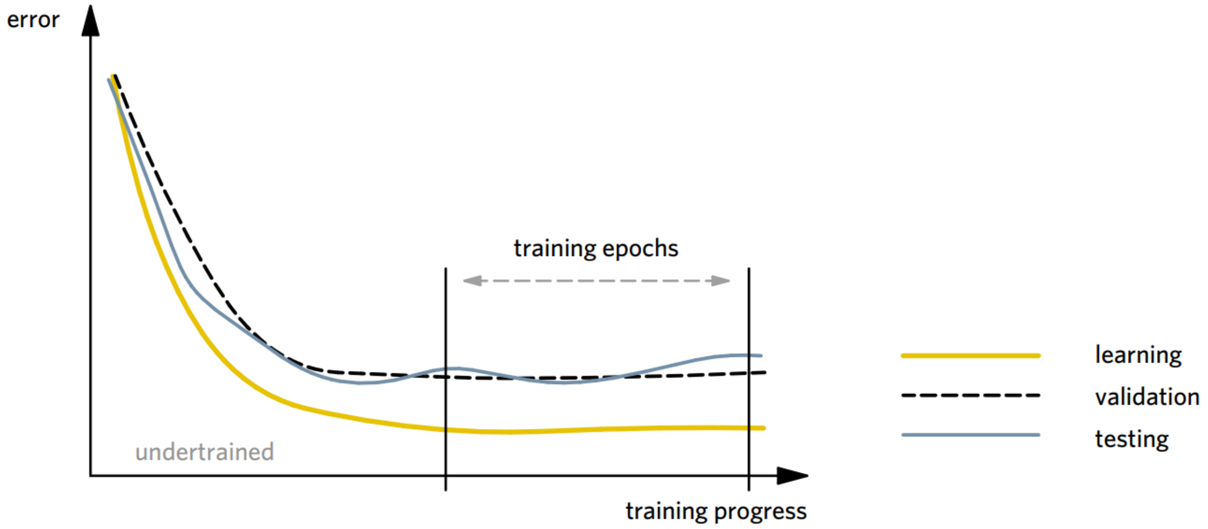

Figure 17. Error fluctuations
(Fruhwirth 2019)

The testing subset is used for quality control and model-error prediction since the data is statistically independent and has not been used during modeling. If a model that fits the learning and validation dataset, also fits accurately the test data, minimal overfitting has been reached.

An alternative for introducing stopping criterions is the very commonly used K-fold cross-validation, which is used to reduce the influence of data variability on model performance (Hastie et al. 2017). In this method similar to the conventional data partitioning, the input data is divided into an arbitrary number of sets also called folds. Each equally divided set is split into three subsets for learning, validation, and testing. The learning set is used to create the ANN. The validation subset is used for quality control and decision making. Based on this subset the model parameters are adjusted to fit the dataset best. If the difference between the learning and testing error is minor the model shows low variance between two data sets. Finally, the statistically independent testing subset is fed into the network. If the testing error is not changing significantly compared to the learning and validation error, a good generalization degree of the model was reached, since the accuracy for all three subsets is in the same range. Before the training starts, hyperparameters are selected and then the model is trained on the first subset so-called K-1 fold. The error for all folds and subsets is calculated separately. The process is repeated for K-folds and the error evolution is monitored and compared between the subset. The subset hyperparameters leading to the lowest validation error is chosen to be tested on the entire dataset. Figure 18 shows how data is partitioned into n-subsets.

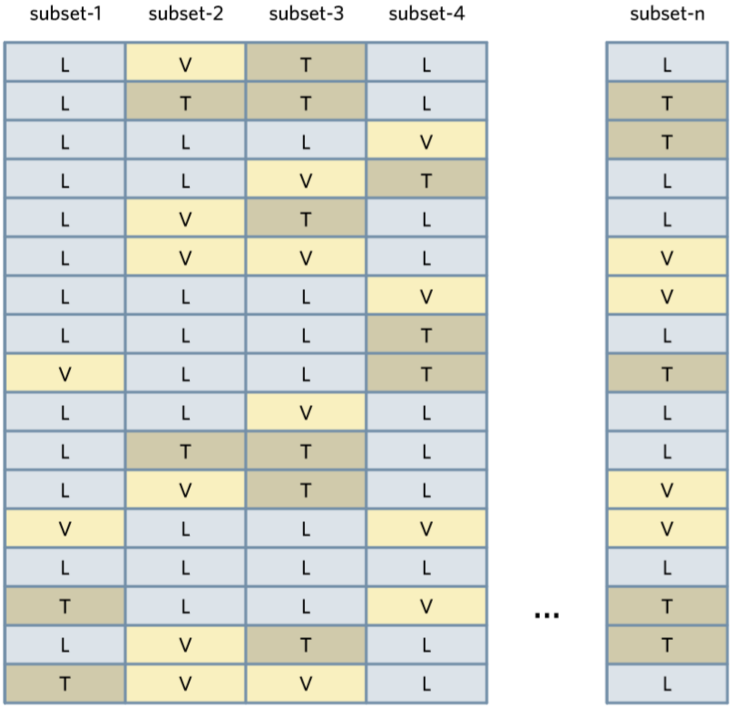

subset-1	subset-2	subset-3	subset-4		subset-n
L	V	T	L		L
L	T	T	L		T
L	L	L	V		T
L	L	V	T		L
L	V	T	L		L
L	V	V	L		V
L	L	L	V		V
L	L	L	T		L
V	L	L	T		T
L	L	V	L		L
L	T	T	L		L
L	V	T	L		V
V	L	L	V		V
L	L	L	L		L
T	L	L	V	...	T
L	V	T	L		T
T	V	V	L		L

Figure 18. K-fold cross-validation principle
(Fruhwirth 2019)

One assumption that is required for conducting cross-validation is that the data points are independent, which is not entirely true for VFM applications. When for instance the pump intake pressure at time t_i is recorded, it will have an impact on the intake pressure at time t_{i+1}. The solution to overcome this dependent relation is to either record data at sufficient big time steps or reduce the prediction operation to steady-state conditions where the pressure reading is not changing with time. Anyhow, if the estimated validation-error indicates a good model performance, but the testing results show an increased error outside of the desired range, the created network is overfitted. If the modeled function shows the described behavior, an unwanted degree of unpredictability, a measure of how a model performs on new data, is reached. High variance is caused by modeling noise, typically by creating a too complex solution network compared to the stated problem. The goal of data-based models is to find an optimum trade-off between variance and bias. A visual representation of the difference between both properties is illustrated in the following Figure 19 (Bikmukhametov und Jäschke 2020).

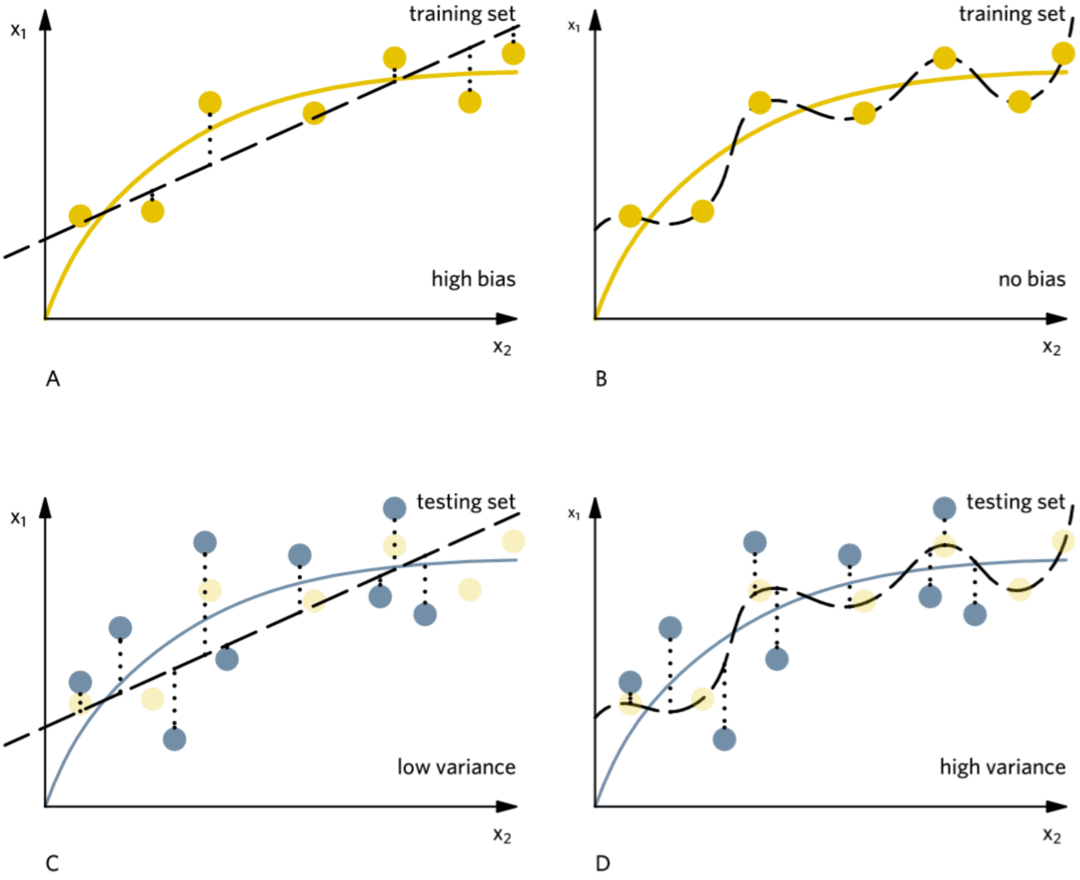

Figure 19. Visual comparison of bias and variance on arbitrary data samples

Picture A and B show how two arbitrary variables x_1 and x_2 relate to each other. The yellow points visualize a training set that was used to train and fit a function describing the relationship. The yellow line represents a logarithmic function which is correlating both variables and is the desired model result. Whereas, the dashed straight-line function is the model output. In picture A it is not accurately fitting the data and is therefore biased. One can calculate the summed Euclidean distance between each data point and the straight line to quantify the bias. In picture B, the same set of data described by a different dashed function is ideally fitting the data points. The dashed function ideally fits the data and doesn’t require any bias correction. Comparing both dashed functions in pictures A and B, one can immediately say that the predicted function in picture B represents a better fit to the training data but not necessarily to the yellow desired function. In the next two pictures C and D, one can see that apart from the training data set an independent set of testing data was added. Again the desired logarithmic function in blue and both dashed functions are shown. In picture C the straight-line function shows again a certain bias with respect to the training data but the difference in bias between both data-sets is comparable. This indicates a low variability of the modeled function. Typically such a function refers to as under-fitted. In picture D, the previously perfectly fitting dashed function is not matching any of the testing points. It is now introducing bias and has, therefore a high variability or variance compared to the straight-line function. This kind of function characteristic refers to as over-trained. Summarizing none of both dashed functions represents the data relationship accurately. This example should demonstrate how an initially well-fitting function might be far away from the actual result, especially when more independent input variables are introduced. Thanks to visualizations it is easier to interpret the outcome. In the case where both, bias and variance are balanced the algorithm has reached a satisfactory generalization. After successful training and testing on partitioned data, the model is ready to be used for predictions on new data with significantly higher confidence (Hastie et al. 2017).

5 Experimental Tests

The objective of this work was to create a data-based model using experimental data to predict multiphase flow using a VFM. The generated ANN is an ESP based model, developed at the Montanuniversity for the purposes of the Artificial Lift Research Centre at the Petroleum and Geothermal Energy Recovery Institute. The data acquisition process was performed under controlled conditions in a laboratory environment. The test data used for modeling the VFM consist of various features like e.g. pressure and temperature readings installed along the flow path. Besides, dynamic data like torque, acceleration, power, and current, readings, which are related to the operational mode of the ESP are used. The ESP operational window was manipulated using a frequency converter for controlled, real-time changes in the desired pumping speed. The modeled three-phase flow of water, gas and synthetic oil was tested under various conditions and with different fluid fractions, according to the desired experiment specifications and facility operation limits. The fractions of water and synthetic oil were measured using a magnetic flow meter and a spindle flow meter respectively. For the quantification of gas, a more sophisticated mass flow meter system was used, which principle will be explained in the next section. The recorded data were digitalized, plotted and analyzed using a Data-Visualization software. The initial goal was to use this VFM model to predict outputs in wells with increased water to liquid ratios (WLR). The elevated water fraction range has both technical and practical reasons. Firstly, the VFM model was initially planned to be trained for wells with marginal feasibility. Secondly, due to the reduced amounts of required synthetic oil, the handling, logistics and the cost of disposing oil-contaminated fluids have been optimized.

5.1 Experimental Setup and Preparation

The PTF is used for research purposes related to artificial lift optimization, development, and testing of new related technologies. Within this facility, all required construction and installation work was done to adapt and utilize the setup according to the needs of the VFM development. The PTF consists of two operational floors. On the lower located basement floor the main container, an isolated steel vessel with a total capacity of 1,3 m³, was placed. This container was used as a water storage tank for withdrawing the water during measurements. For this purpose, the tank was pressurized with compressed air or a piston pump to a maximum pressure of 35 bar. After the pressure build-up, the water outflow was controlled by changing the regulating valve position. The tank was equipped with a manometer, liquid level meter, pressure release valve, inside heating coil, additional connection ports, pressure, and temperature sensors. The water flows from the tank over a magnetic flowmeter, where the water quantity is computed based on the voltage induced across the electrodes, which are positioned perpendicular to the applied magnetic field. The charged particles of water are separated into negative and positive ions when passing the magnetic field. Cations and anions accumulate on the opposite electrodes causing a potential difference that is proportional to the flow. The synthetic oil used in the experiment is non-reactive, odorless polydimethylsiloxane with a viscosity of approximately 10 mm²/s. It has a density of roughly 0,93 g/cm³ at 25°C and its chemical structure is shown in Figure 20.

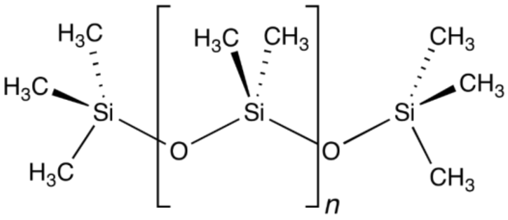

Figure 20. Polydimethylsiloxane
(IFA 2019).

Silicone oil shows physical properties similar to crude oil and is non-polar. Different to crude oil polydimethylsiloxane is non-toxic and non-flammable and was therefore used in the experiments (IFA 2019).

Oil was flowing from a hanging cylindric tank fixed on the same framework as the ESP with a capacity of roughly 220 L. The oil was firstly manually poured into the tank using a funnel to reduce the risk of spilling. The oil tank was equipped with a ball-valve on the top which was opened for re-filling operations but closed again during production. Apart from a pressure release valve fixed on the oil tank, a screw-type displacement pump was installed to keep the tank pressure constant during the withdrawal process. There are two pressure and temperature sensors installed, each one on the top and the bottom. The oil vessel is hydraulically connected to the water tank and operated at the same pressure and temperature of roughly 20°C. Before entering the tee-connector the bypassing oil amount is measured using a screw-type flowmeter, which is a type of displacement pump and derives the flow rate based on the cylinder diameter, displaceable volume per rotation and the number of rotations over a given amount of time. For simulating natural gas we used compressed air, which was fed to the system from a compressed air stack. The gas flow was recorded using an absolute and dynamic pressure gauge. Before being comingled with the water and oil fraction, the temperature of the gas stream was measured. Based on these three measurements the gas rate was mathematically computed. A detailed description of the gas-rate computation is part of the error propagation section. Additionally, a control-valve is installed together with a check-valve. The control-valve position allows regulating the portion of inflowing gas. Its function is crucial since a too wide open passage would lead to a complete cut-off of the remaining two phases during a three-phase test. From the tee-connector, the fluid mixture flows into a vertically installed static mixer tube to ensure consistent mixing during the measurement cycles. From that point on, the fluid flows mostly in a vertical direction until it reaches the wellhead on the upper floor. The mixed fluid is then entering the vertically hanging ESP at its intake where the temperature and pressure are recorded. The ESP used in this experiment is a mixed flow impeller pump, equipped with 82 stages, designed for a production rate of 13,9 m³/ h, which is equal to roughly 334 m³/day. The pump motor is driven by a frequency converter that allows changing the motor-shaft rotations per minute (RPM) according to the planned production rate. The operational window of the installed ESP is shown in Figure 21.

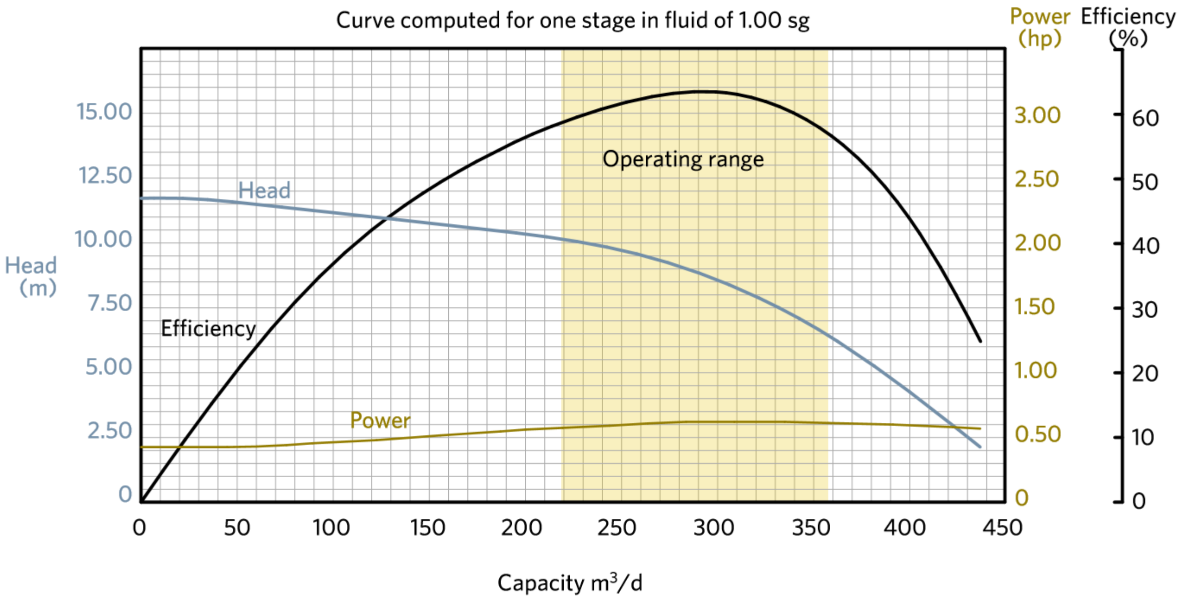

Figure 21. Arbitrary ESP operational envelope

This pump curve is recorded for the pump running at 50 Hz and a pump speed of 2917 RPM The yellow-colored plane in the graph represents the operating range which is desired for running the pump at optimum efficiency. On the bottom of the pump additional sensors monitoring the motor torque, temperature and acceleration are installed. At the pump discharge, the fluid leaves the pump and the temperature and pressure are measured again. The fluid mixture travels via a hosepipe to the wellhead, where the respective pressure and temperature are recorded. The output can be manipulated using another installed control valve, which is controlling the opening position and acts like a backpressure choke. After passing the wellhead the fluid flows back down to the basement into an intermediate bulk container (IBC), closing herewith the flow loop. The IBC tank is equipped with a liquid-level meter to mitigate the risk of overfilling and automatically close the installed valve in case the

IBC is full but the operator did not stop the pumping procedure. The overview of the measurement setup is shown in Figure 22.

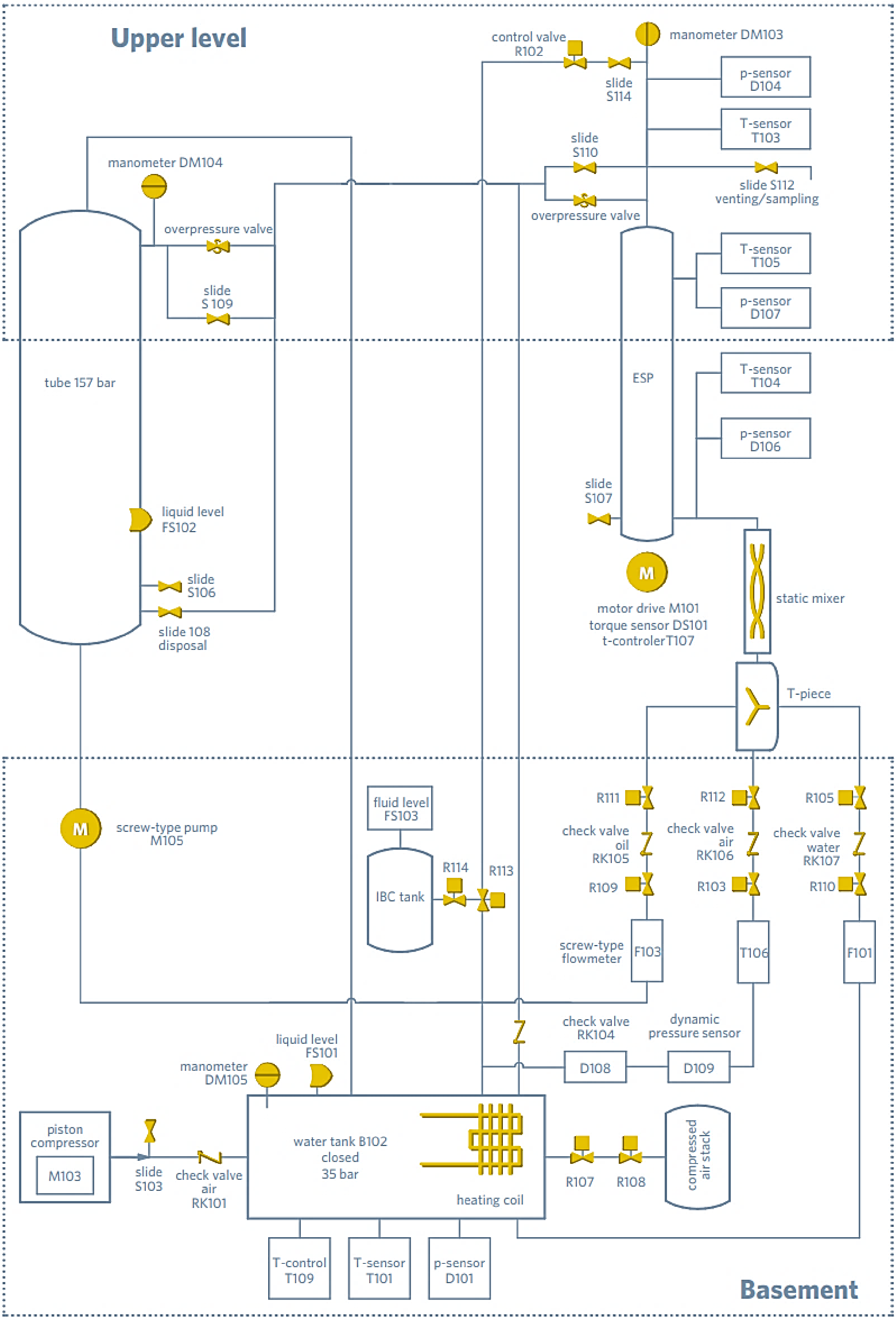

Figure 22. Experimental setup for VFM data acquisition

After a completed cycle the produced fluid is left in the tank until the liquid phases separate, whereas the gas is vented. Typically for separation, the IBC tank was lifted to the upper level and left for 24 hours until the phase separation was completed. This separation step was important to recover the oil and reuse it in the next experiment run. This action allowed to reduce the amount of fresh oil used for the experiment. Since, both water and the synthetic oil were initially colorless their optical identification was challenging. To overcome this problem an organic compound, known as Sudan Blue (II) was added to colorize the oil and enable a good visual identification which led to more efficient oil separation. Sudan Blue (II) is an anthraquinone dye used for coloring organic hydrocarbon-based solvents like oils, fats or waxes. It was bought as a blue powder and added to the oil before filling the oil tank. A half-filled teaspoon is enough to colorize around 200 l of oil. The chemical composition of Sudan Blue (II) is represented by the formula in Figure 23 (Jenny Hartmann-Schreier 2015.).

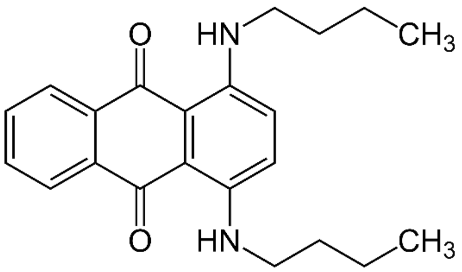

Figure 23. Sudan Blue (II) IUPAC name:1,4-bis(butyl-amino)anthraquinone (Jenny Hartmann-Schreier 2015)

The separated oil was used to refill the oil tank and a new IBC tank was placed at the position of the previous one, ready to receive the fluids from the next cycle. These steps were required to save-up time and conduct new measurements continuously. Before starting the next run the water vessel was filled with freshwater and pressured again. If all other required measures like e.g. visual leak investigation were taken a new test-run was about to start.

When working under laboratory conditions a significant role plays the disposal ability to the used chemicals since they might be linked to meaningful costs in a project. In this experiment apart from water and gas, which don’t need any legal authorization from the local environment authorities, the used synthetic oil needed to be separated and disposed of according to the Austrian Waste Management Law (RIS - Abfallwirtschaftsgesetz 2002 - Bundesrecht konsolidiert, Fassung vom 26.05.2020 2020). The challenge that arose during the operations was the oil-contaminated water, which could not be separated completely through gravitation and needed additional treatment. After the gravity separation of oil and water in the IBC tank, an intermediate phase consisting of a dense emulsion was separated and left for disposal with all the other emulsion fractions created during each measurement. The residual water needed additional analysis to assure that the water chemistry, which was influenced by the synthetic oil, is compiling with the requirements and threshold values defined by the Austrian law and local authorities. For this purpose, the Cleanliness association in Leoben (Reinhaltungsverband in Leoben) was contacted to evaluate the water properties and trace amounts of hydrocarbon-based solvents and fats, that are allowed to be regularly disposed of with fresh water into the sink. The relevant threshold values that needed to be estimated are the chemical oxygen demand (COD), the pH-value, solid particle fraction and the total concentration of hydrocarbons. Table 1 shows the maximum allowable threshold values received from the Cleanliness association.

Table 1. Required water specification for regular disposal

Property	Limit
Total hydrocarbon content	10 mg/L
COD	600 mg/L
pH	6,5-9,5
Max. temperature	35°C
Solid particle fraction	10 mg/L

The temperature and pH measurement could be easily controlled. The water tank is left for conditioning at ambient temperature and the pH measurement is done with pH indicator strips. More complex is the estimation of the total hydrocarbon content and the closely related COD which is a measure of the number of oxidizable pollutants that can participate in reactions with oxygen as the oxidizing agent, expressed in mass of oxygen per volume of solution, mg/L. Any organic compound like e.g. oil, when introduced to the water can be oxidized to CO_2 using strong oxidizing agents in an acidic milieu. This process is used during water examinations to quantify the number of organics diluted before the disposal permit is given. The detailed procedure is described in the ISO 6060 norm. For the examination of organic compounds, which were introduced by synthetic oil, a quantum cascade laser spectrometer (QCLS) was used. This device is capable of measuring the total hydrocarbon content in the range of 0,1 mg/L.

Before the oil content analysis, the remaining water from one test cycle was pumped into a clean IBC tank through an oil filter pump. This measure was required to minimize the oil contamination of water before testing with the QCLS. For the measurement, at least one liter of the contaminated water was sampled and analyzed in the laboratory. The water sample required prior preparation before being tested. In the beginning, a 900 mL sample was poured together with 50 mL cyclohexane into a glass bottle closed with a cap and vigorously mixed for 5 minutes. One could do the mixing manually, use an analytic shaker, or put the sample into an ultrasonic bath. The mixing was performed to assure that all of the organic compounds dissolved in water are transferred to the organic cyclohexane phase. After the phase separation, the lighter organic phase was sucked from the top by a pipette. Roughly 40 mL was needed for the measurement. Before the sample was inserted into the QCLS a reference spectrum, so-called blank, needed to be measured. As a blank sample, 40 mL of pure cyclohexane was used. In the next step, the first sample measurement was conducted and delivered values between 250-400 mg/L, which were too high at least by one order of magnitude. To reduce the hydrocarbon concentration the water from the IBC tank was left for additional 24 hours, filtered, sampled and analyzed again. Nevertheless, additional measures reduced the concentration to around 25 mg/L, the allowable limit could finally not be reached. This resulted in an increased amount of liquid that needed to be exposed to the costs of the department.

The performed program consists of 32 measurements which are separated into three categories depending on the number of measured phases. In total 3 single-phase, 11 two-phase and 18 three-phase experiments were carried out and processed. During the measurement-cycles different pump-speeds, rates and control-valve positions were tested, in total 85 different configurations where recorded. Table 2 summarizes the conducted experiments, their type and the number of tested configurations in each cycle.

Table 2. Experimental program

#	Date	Type	Number of configurations
1	30.09.2019	2-Phase	2
2	03.10.2019 (1)	2-Phase	2
3	03.10.2019 (2)	2-Phase	1
4	04.10.2019 (1)	2-Phase	1
5	04.10.2019 (2)	2-Phase	1
6	16.10.2019	2-Phase	2
7	18.10.2019	2-Phase	2
8	23.10.2019	2-Phase	2
9	24.10.2019	2-Phase	2
10	21.11.2019	2-Phase	1
11	28.11.2019 (1)	3-Phase	2
12	28.11.2019 (2)	3-Phase	3
13	02.12.2019 (1)	3-Phase	3
14	02.12.2019 (2)	3-Phase	2
15	04.12.2019	1-Phase	1
16	05.12.2019	2-Phase	2
17	06.12.2019	1-Phase	4
18	09.12.2019	3-Phase	2
19	11.12.2019	3-Phase	2
20	13.12.2019	3-Phase	3

21	16.12.2019	1-Phase	3
22	19.12.2019 (1)	3-Phase	5
23	19.12.2019 (2)	3-Phase	5
24	19.12.2019 (3)	3-Phase	3
25	09.01.2020 (1)	3-Phase	3
26	09.01.2020 (2)	3-Phase	3
27	13.01.2020	3-Phase	4
28	28.01.2020 (1)	3-Phase	4
29	28.01.2020 (2)	3-Phase	3
30	27.02.2020 (1)	3-Phase	4
31	27.02.2020 (2)	3-Phase	4
32	28.02.2020	3-Phase	4

5.2 Experiment evaluation

To build a VFM model precisely quantified 3-phase experiments are required. Additionally to three-phase experiments, one and two-phase experiments were conducted to improve, test and adapt the experimental setup by controlling and adjusting the flow-control system. It was necessary to test the control-valve positions and configure the pumping system to perform stable three-phase quantifications. Each data set was analyzed and modeled individually to predict the flow rates for each cycle. In some two-phase experiments, the gas rate was very low and the error in the prediction was significant. Whereas, water could be predicted in most experiments in a satisfactory manner. The three-phase experiments were analyzed in the same way as the two and single-phase experiments. Based on the processing and filtering workflow developed and improved during modeling two and single-phase data, a deeper understanding of the recorded features and their dependency between the flow rates could be acquired.

During the production procedure depicted sensor-data are screened in real-time. In Figure 24 a typical data display is shown. These readings are used by the operator to monitor and control the system during production cycles.

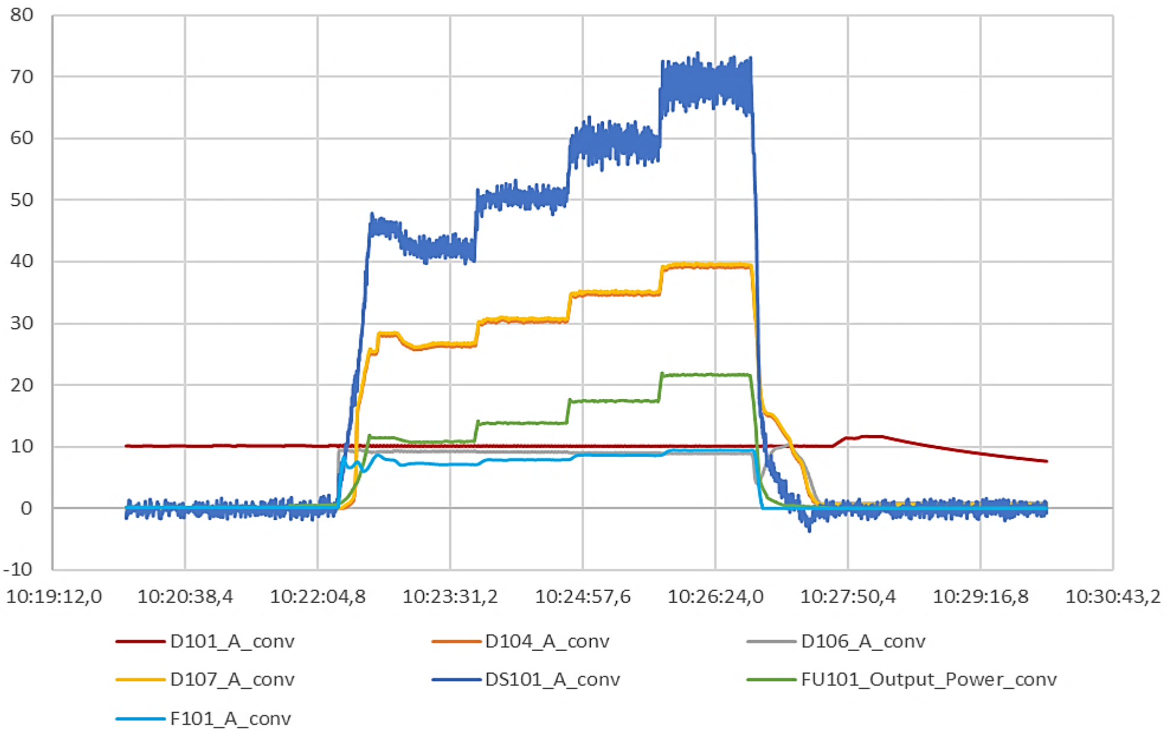

Figure 24. Monitored sensor data during a measurement cycle

This graph represents a typical measurement cycle. On the x-axis, the time is plotted whereas on the y-axis the measured quantity. Different properties with different units are shown in the graph. Since the ranges of the measured parameters have a different magnitude the readings are normalized to allow better visualization. The steps that can be recognized are related to the changing RPM of the motor and herewith changing power consumption which is represented by the green line in kW. The torque record is represented by the uppermost blue line in Nm. The first step in this example was run at 2200 RPM followed by an increase of 200 RPM until the maximum speed of 2800 RPM was reached. Each production step was kept steady for roughly 1 minute. Apart from the power reading in green, one can recognize the pump intake and discharge pressure, in grey and yellow respectively. The orange line which is the wellhead pressure sensor reacts stepwise on the changes in the system. The red and light-blue colored lines are measuring the water tank pressure and the water flow rate in bar and m³/h respectively. The flowrate is reacting proportionally to the changing RPM. The grey line which records the pressure intake is stable over the major part of the measurement and denotes a small drop during the last step at 2800 RPM. This might be due to the decreasing inflow rates from the emptying tanks. The red line shows similar behavior to the grey line since it remains mainly steady. This is a good sign since the red line records the water tank pressure, which is mimicking the reservoir pressure and similar to a real reservoir it should not vary significantly. Apart from the sensor-reading plot, a flow rate diagram, as shown in Figure 25 was plotted and observed simultaneously to react quickly, if the flow of any phase was prevented.

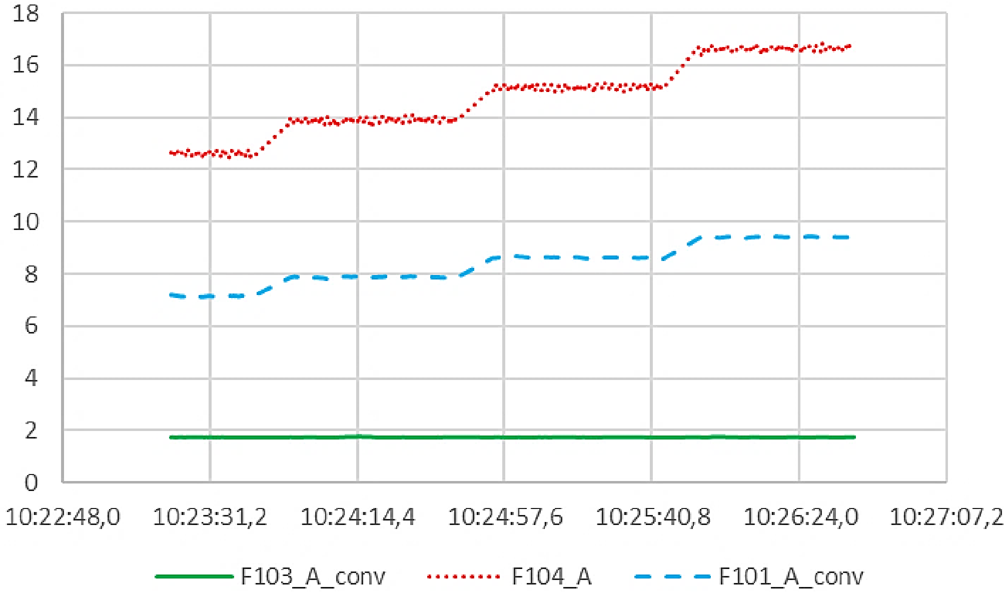

Figure 25. Monitored flow rates from measurement cycle

The water and gas rate is described by the blue and red lines respectively. One can see how both react on the system changes and recognize that both reflect the same step-behavior. In contrast, the oil rate represented by the green line is kept constant. The operator can control the fluid outflow by regulating the control-valve position as needed. Based on a fluid level measurement in the oil tank, the operator estimates the remaining production time before switching off the pump, since the oil amount is the limiting factor. Based on the readings the operator can control and in case of unpredicted malfunction, stop the measurements sufficiently early to reduce the risk of spilling, pressure build-up, and further damage. It is recommended to work in a group of at least two people since the person monitoring the visualized data is not able to observe the situation in the basement. The second person must not work in the basement during a running operation but should rather observe the system from the top floor and inform the operator about unexpected behaviors during a test.

The evaluation process will be explained on the measurement results derived on 09.01.2020. The data-analysis started with the import of the recorded data, in the desired time interval into an Excel sheet for further inspection. The recorded sensor data was visualized in a cartesian plot as shown in Figure 26. Here the recorded features are plotted against the horizontal time axis.

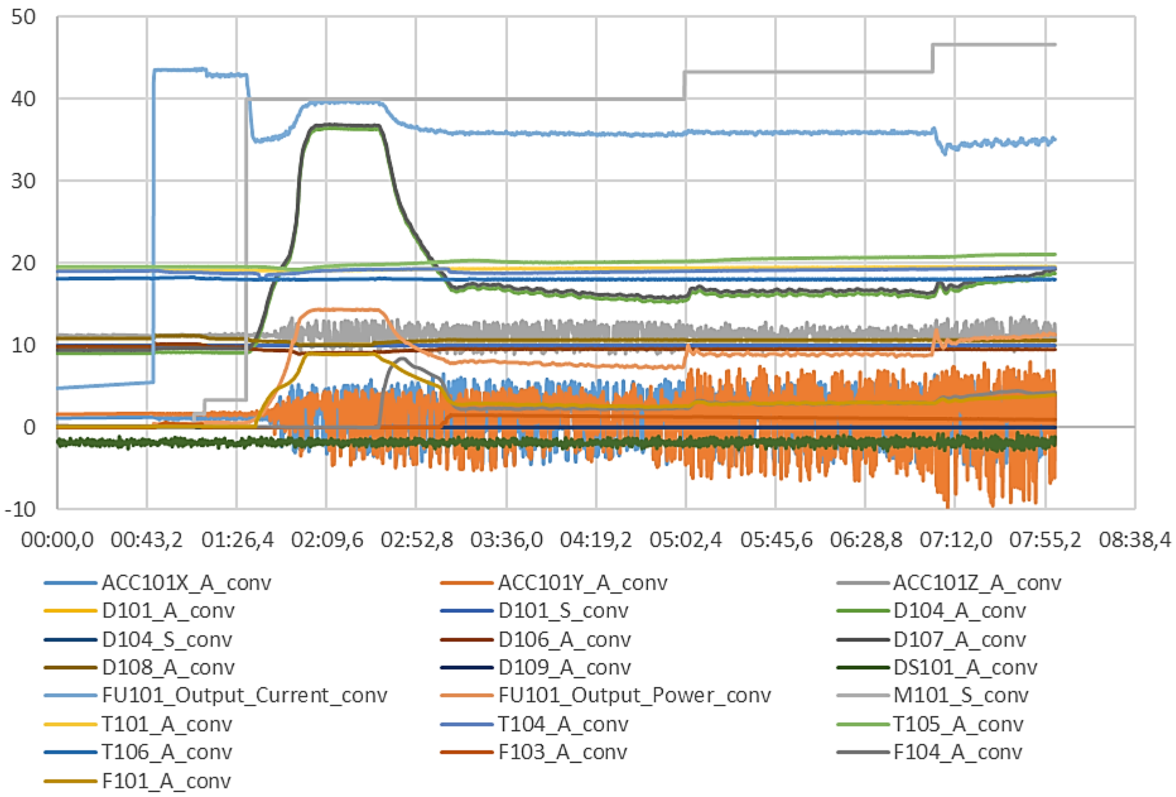

Figure 26. Raw-Data visualization

The interpretation and extraction of valuable information from this graph is hardly possible. There are too many features overlapping with each other causing confusion and are not useable for further decision making in its raw form. To overcome this problem the data needs to be filtered from unstable and transient behavior, according to the steady-state requirements of a feed-forward network. It was necessary to filter the spectrum from the initializing time at start-up and the parts were the pump-frequency was increased. The filtered data spectrum is shown in Figure 27.

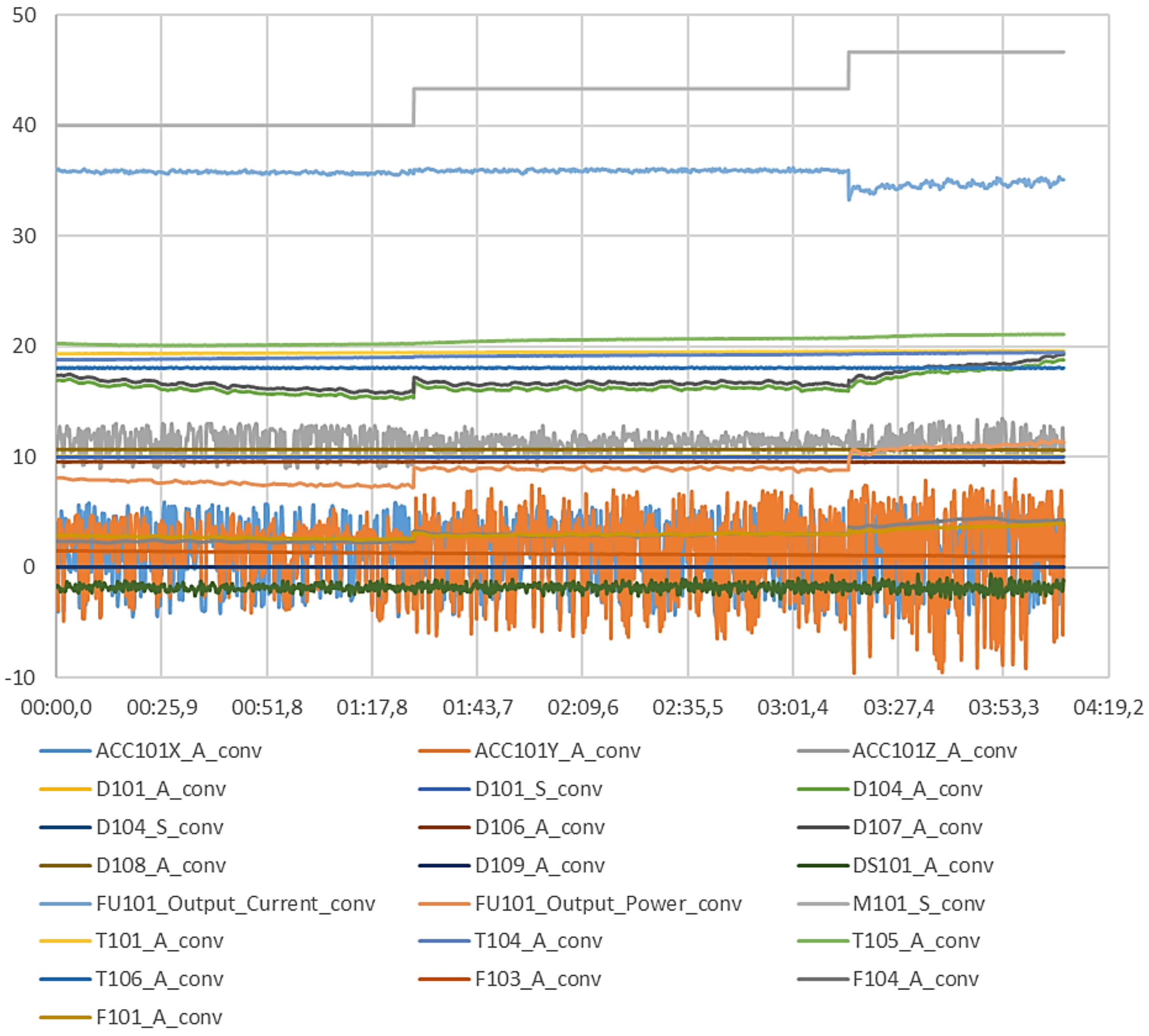

Figure 27. Filtered steady-state spectrum

One can immediately recognize the process steps and the dominating steady-state behavior of the records during a constant pumping frequency. Some data ideally follows the frequency trend, whereas other data records show significant fluctuations. Generally, the data structure and vision could be improved by this step. It made the recorded spectrum easier to interpret but additional measures and further separation into four subsets namely temperature, pressure, dynamics and flow-rates was required to make the examination of individual sensors easier. The dynamic part summarizes all data records directly linked with the changing pump frequency. The generated plots of the additional subsets are shown in the following figures.

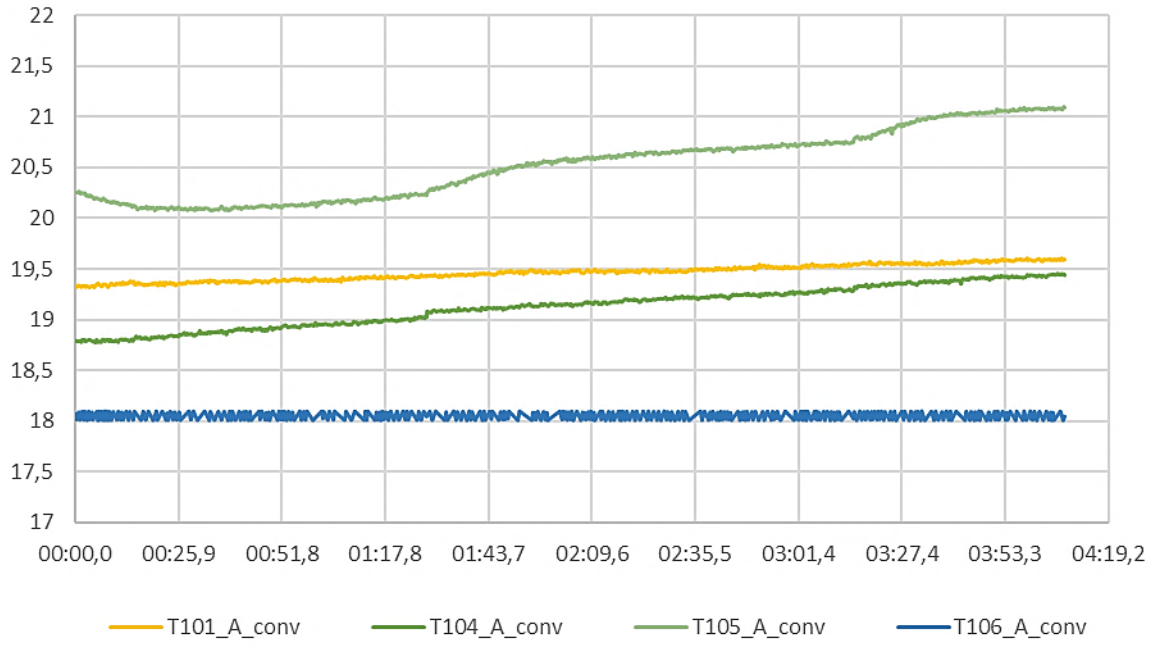

Figure 28. Steady-state temperature records

Figure 28 shows the temperature records from four different spots. T101 corresponds to the water tank temperature and is showing a weak increase in time, similar to T104 which is the temperature at the intake of the ESP. This gradual temperature increase of both sensors T101 and T104 can be explained by the fact that in this particular experiment the oil tank was filled with water and without any oil, in the system, the fluids could be pumped in a continuous cycle without directing the fluids into the IBC tank. During this circular pumping mode, heat from the ESP was transferred to the pumped fluid in each cycle, which led to this flat but visible temperature increase. T105 is the discharge temperature and is increasing differently since it is directly linked to the introduced heat within the pump. T106 is the only reading showing a constant record with minor fluctuations throughout the whole measurement cycle. It is constant because the temperature of the introduced air is measured before entering the flow-loop and is, therefore, not influenced by the generated parasitic heat.

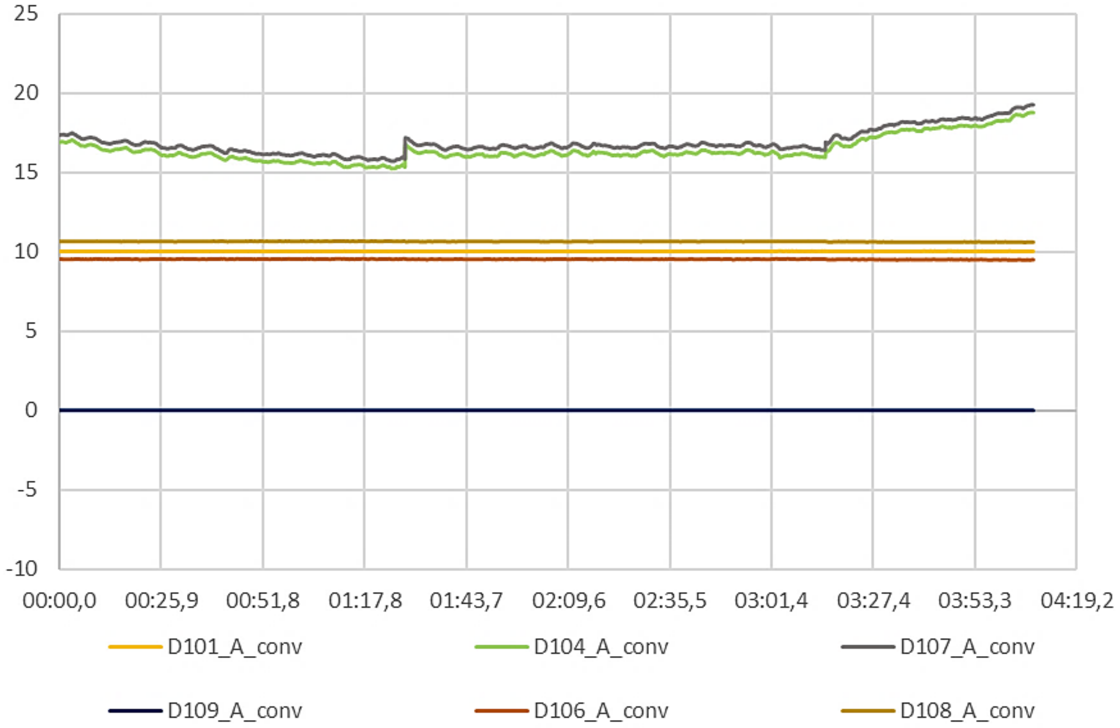

Figure 29. Steady-state pressure records

Starting from the top records in Figure 29, both wiggly lines are nearly perfectly overlapping and represent the sensors D104 and D107. The slightly higher positioned line is the discharge pressure, D107 recorded at the ESP outlet. The stream pressure is then measured next at the wellhead, D104 and is slightly lower due to the pressure losses along the flowline. The next two recorded pressures are captured by the sensors D106 and D108 which measure the intake pressure of the stream and the static gas flowing pressure respectively. At exactly 10 bar, positioned between D106 and D108, the water tank pressure D101 is shown. The lowermost pressure record is D109. D109 is measuring the dynamic pressure in the gas supply line and is used together with D108 and T106 for the mathematical determination of the gas rate.

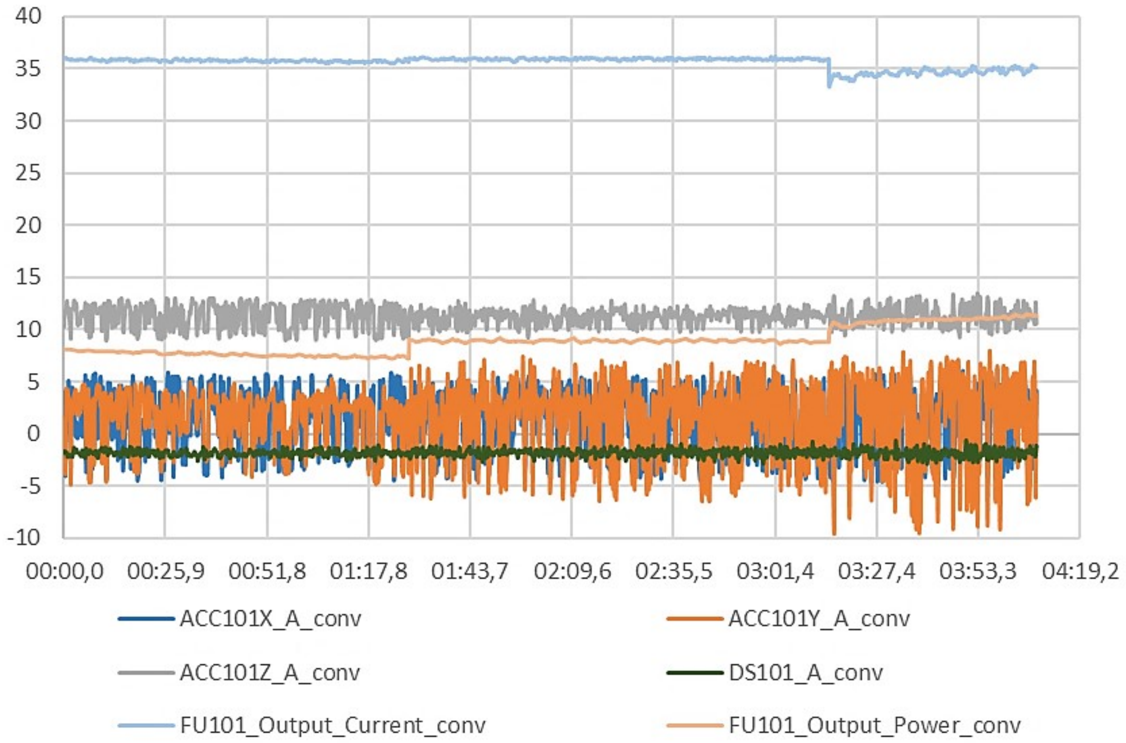

Figure 30. Steady-state dynamics records

In the summarized dynamics-window in Figure 30, the fluctuations are stronger than in any other subset. The two records FU101_Output_Current on the top FU101_Output_Power in the middle of the plot show a constant behavior and are the current and power output of the frequency converter. The third sensor showing low fluctuations is the DS101, which is measuring the motor shaft torque. The last three readings are the ACC101X, ACC101Y and ACC101Z sensors, which are fixed to the steel framework where the ESP hangs and are measuring its acceleration in three different directions x, y, and z.

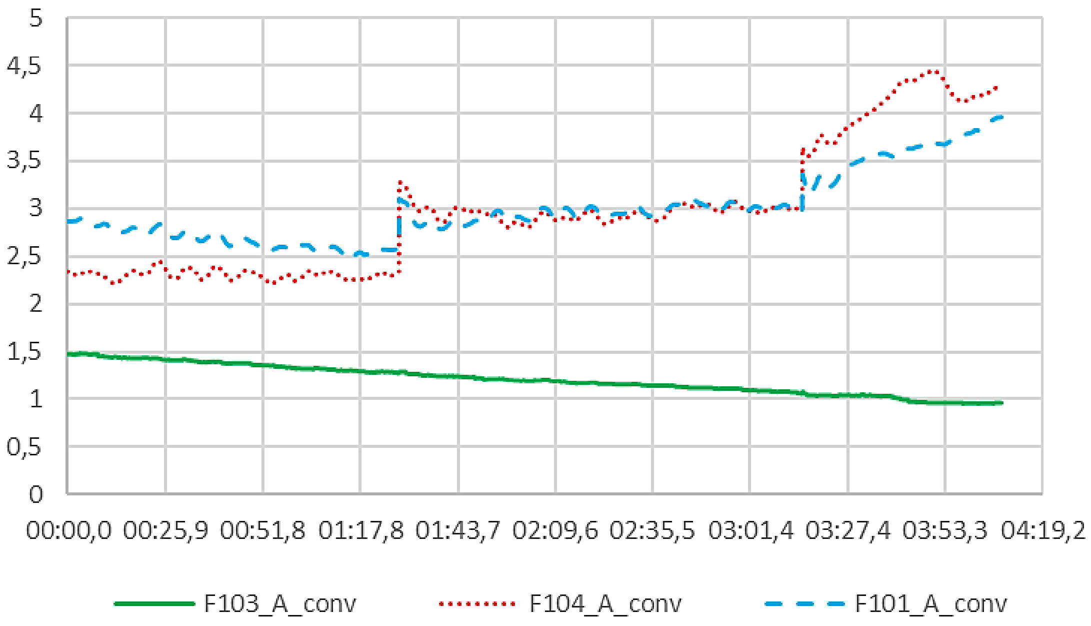

Figure 31. Steady-state flow records

In Figure 31 the desired VFM-model variables are recorded. These three lines represent the flow rates of each phase and are recorded before the fluids are mixed and pumped through the ESP. Throughout this work red is the color assigned to gas in kg/h, blue to water in m³/h and green represents oil in m³/h. In this figure, one can identify the steadily decreasing amount of oil, while gas and water have a similar but reciprocal behavior showing an increase in the gas flow, when water flow is decreasing and vice versa. This decreasing nature of the oil-rate, which in this experiment was replaced by water, was not desired. To reduce this effect a displacement pump was installed to preserve the flowing pressure and keep the oil-rate constant. A desired outcome that was recorded during a three-phase measurement cycle with synthetic oil from 28.01.2020 (2) is shown in Figure 32.

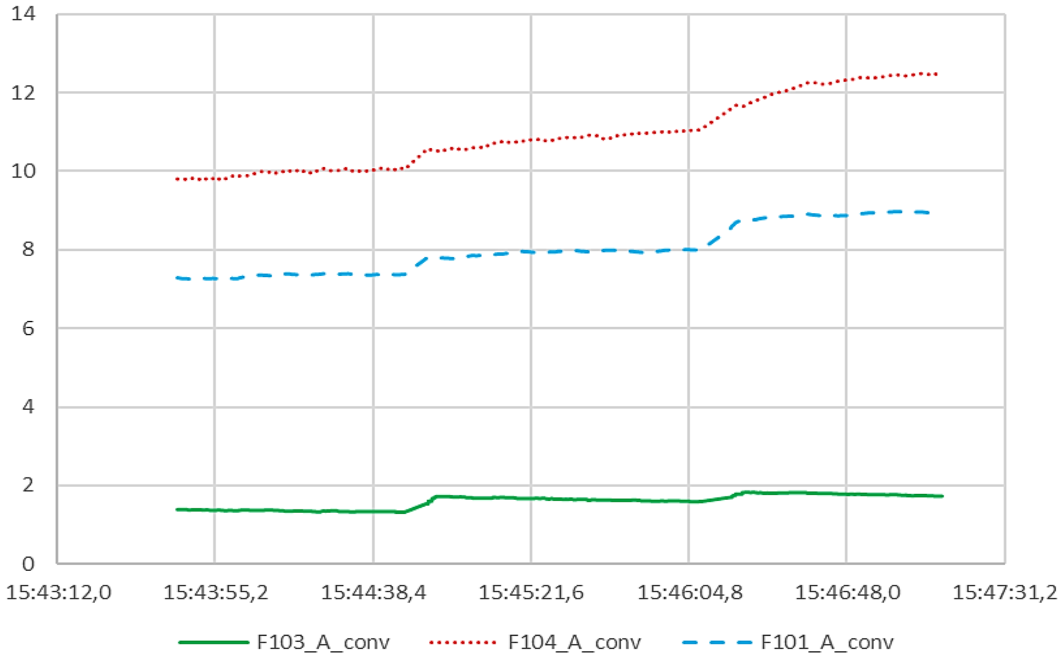

Figure 32. A desired steady-state flow record

The slicing and separation process was repeated for each individual experiment cycle. The imported data was filtered and prepared to be used as input for a feed-forward artificial neural network. The objective was to find clean and stable measurement configurations for both, recorded variables and flow rates. It was necessary to consider the error introduced by the sensors because some of the properties were calculated by combining the measurement outputs. The quantification of the relative error concerning the measurement range was required to not overestimate the accuracy of the VFM-model.

6 Error propagation

The data acquisition was carried out with different measuring instruments. Some could determine the desired property directly others were used in combination to compute the needed property. It was, therefore necessary to describe, understand and include the occurring error sources of each measurement to account for their propagation. Error propagation or propagation of uncertainty is an important measure to identify how the error propagates due to the mathematical combination of several variables. An error can be expressed as an absolute number or relative value, often stated in percent. The manufacturer typically states in the instrument manuals a relative error as a function of the measured range. A commonly found error-function is shown in Figure 33.

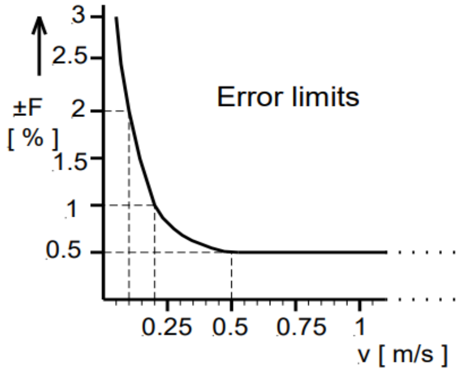

Figure 33. Relative error as function of the measurement window

It is desired to track the introduced errors to estimate the accuracy of the measurement outcome. Typically, the first step is the error source investigation to determine where errors are introduced. In the PTF we differentiate between the following error sources:

- Error of instruments
- Error from artificially introduced heat
- Error related to the power-loss along with the installed cables
- Combined error from calculated properties.

All sensors relevant for this experiment have already the ability to compensate for the error resulting from the thief cable resistivity. The introduced heat causing a temperature increase could only be corrected with an installed cooler or heat-exchanger, nevertheless, the same circumstances of introduced parasite-heat to the system are found in the field, so their correction will not necessarily contribute to any improvement in the model. When measuring properties we need to distinguish between accuracy and precision. The manufacturer often uses both terms interchangeably, which is not entirely correct. Accuracy describes the ability of an instrument to quantify the true value of the desired property. This means that if the room temperature e.g. is at 20,6 °C and the thermometer measures 20,5°C it is more accurate than a thermometer that would show 20,4°C since the ΔT is smaller. The error in a thermometer comes from two sources, the sensor, typically a platin wire and the electronics, responsible for converting analog to digital signals. If the thermometer is measuring in a range between -30°C and 60°C the relative error is calculated by dividing the difference, $\Delta T = 0{,}1$ by the total range. In this example $\frac{0{,}1}{|90|}$ which results in 0,11%.

In resistance thermometers, the relative error is not constant. Manufacturers typically distinguish between sensor and electronic error and provide a simple relationship that depends on the performance class of the thermometer. Equation 10 shows the absolute error for an A-class, Pt-100 thermometer (DIN EN 60751).

$$\Delta T\ [°C] = 0{,}15 + 0{,}002 \times |T| \qquad \text{(Eq. 10)}$$

The constant value of 0,15 is the sum of the constant error introduced by both the platin wire and the electronics and is related to the set span. The variable part is the error related to the platin wire type, calibration range and scales with the measured temperature regardless of the sign. To calculate the maximal relative error for the temperature sensors used during the experiment the constant value 0,15 was added to the maximum possible temperature, according to the sensor range, and multiplied by 0,002. Since, all the temperature sensors except T102 are in the same performance class A, the maximal relative error results in 0,35% For a range between 0-100°C. T102 which has a B-class performance has a maximum relative error of 0,7% for a range between 0-150°C. Equation 11 shows the maximal absolute error for a B-class, Pt-100 thermometer (DIN EN 60751).

$$\Delta T\ [°C] = 0{,}3 + 0{,}005 \times |T| \qquad \text{(Eq.11)}$$

Different from accuracy, precision is a measure of the repeatability of analysis. Going back to the example with the room temperature evaluation. If one enters the room with a thermometer and measure 20,4°C, then leave the room and enter the room again to measure the temperature a second time and the thermometer shows the same value. Then the instrument is precise but not accurate. This type of error is a systematic error and is reproducible. For accurate evaluation statistical approaches are typical.

To evaluate some properties a combination of measured data was required. Table 3 summarizes the maximal relative sensor errors based on their measuring range. Whereas Table 4 shows the calculated data.

Table 3. Sensor list

Name	Description	Error	Unit
ACC101X_A_conv	Shaft acceleration	1,0%	g
ACC101Y_A_conv	Shaft acceleration	1,0%	g
ACC101Z_A_conv	Shaft acceleration	1,0%	g
D101_A_conv	Water tank pressure	1,0%	bar
D102_A_conv	Oil tank pressure down	0,3%	bar
D103_A_conv	Oil tank pressure top	0,3%	bar
D104_A_conv	Pressure wellhead	0,3%	bar
D106_A_conv	ESP intake pressure	0,3%	bar
D107_A_conv	ESP discharge pressure	0,3%	bar
D108_A_conv	Static air pressure	0,85%	bar
D109_A_conv	Dynamic air pressure	0,16%	bar
DS101_A_conv	Shaft torque	0,1%	Nm
F103_A_conv	Oil rate	0,3%	m^3/h
F101_A_conv	Water rate	3,0%	m^3/h
FS101_A_conv	Liquid level in water tank	1,5%	m
T101_A_conv	Temperature water tank	0,3%	°C
T102_A_conv	Oil tank temperature	0,7%	°C
T103_A_conv	Temperature wellhead	0,35%	°C
T104_A_conv	ESP intake temperature	0,35%	°C
T105_A_conv	ESP discharge temperature	0,35%	°C
T106_A_conv	Air temperature before tee	0,35%	°C

Table 4.Calculated properties

Name	Description	Error	Formula	Unit
F104_A_conv	3 sensors combined (4 sec. average)	2,60%	Explained below	kg/h
M103_Rate	Piston compressor	2,0%	0,0015*D101-0,1318*D101+230689	kg/h
FU101_A_conv	Drive power M101 (4 sec. average)	3,1%	FU101_Speed/9550*DS101	kW
P101_A_hydr_conv	Hydraulic power	3,6%	D107-D106_conv*F101_A_conv/36	kW
dP D107-D106_conv	ESP differential pressure	0,6%	D107_A_conv-D106_A_conv	bar
dT T104-T105_conv	ESP differential temperature	0,2%	T104_A_con-T105_A_conv	°C
FU101_Current	FC- current	0,1%	FU101_Output_current/10	A
FU101_Torque	FC- torque	0,1%	FU101_Output_torque*177/1000*-1	Nm

The gas estimation is based on the ideal gas equation. Firstly using the temperature record T106 and static pressure D108 reading the density is calculated. Then the aperture opening of the gas stream A is normalized by the pipe diameter before the aperture, to calculate the constant c_2. These values are then combined with the dynamic pressure record D109 and D108 to calculate c_3 and finally determine the gas-rate, F104 as described by the following formulas.

$$F104 = (D108 - 0{,}008) \times 50000 \times 2 \times \rho \times \sqrt{A^2 \times 0{,}7853 \times c_3 \times c_1} \times 3600. \qquad \text{(Eq. 12)}$$

Where F104, is the gas rate, D108 the static pressure record in the gas line, ρ the gas density, A the pipe diameter before the aperture. Further, c_1, c_2 and c_3 are factors that are calculated as shown in equations 13 to 15.

$$c_1 = \frac{0{,}5988}{\sqrt{1-c_2{}^2}} \qquad \text{(Eq. 13)}$$

$$c_2 = \frac{A}{0{,}016} \qquad \text{(Eq. 14)}$$

$$c_3 = 1 - \left[\frac{D109 \times 5000 \times \left(0{,}35 \times c_2{}^4 + 0{,}41\right)}{D108 \times 4000000 \times 1{,}395}\right] \qquad \text{(Eq. 15)}$$

To estimate the factor c_3 the dynamic pressure record D109, the factor c_2 and the D108 readings are required. For gas density calculation the static pressure record D108 and T106, the gas temperature is required.

$$\rho = \frac{D108 \times 4000000}{[(T106 \times 100) + 273{,}15] \times 287} \qquad \text{(Eq. 16)}$$

Now to compute the error of the non-physical F104 sensor we need to combine the errors of each contributing instrument. For this reason, it is necessary to understand how mathematical operations transfer the error. There is a difference in whether one calculates with absolute values or a relative error range. The impact of a faulty feature on the result can be in both cases estimated using the Taylor series expansion, shown in equation 17 (G. Hartwig 2011).

y…result

x…feature

Δx…error

$$y(x + \Delta x) = y(x) + \frac{1}{1!}\frac{dy(x)}{dx}\Delta x + \frac{1}{2!}\frac{d^2y(x)}{dx^2}(\Delta x^2) + \cdots \qquad \text{(Eq. 17)}$$

If the error is sufficiently low, the series development can be stopped after the second series since a small error powered by two or higher, lead to technically negligible errors and do not impact the result reasonable. Equation 18 can be therefore written as follows.

$$\Delta y = y(x + \Delta x) - y(x) = \frac{dy(x)}{dx}\Delta x \qquad \text{(Eq. 18)}$$

If more faulty features have a contribution, the equation can be adopted in the following way.

$$y(x_1, x_2, \dots) = \Delta y = \frac{\partial y}{\partial x_1}\Delta x_1 + \frac{\partial y}{\partial x_2}\Delta x_2 + \cdots \qquad \text{(Eq. 19)}$$

The partial differential describes how much the result is changing with the change of the denominator considering that other features are held constant. Calculating with absolute error values, the total error can be simply added up for both additions and multiplications. In the case of divisions and subtractions, the absolute errors are subtracted. When calculating with a relative error range the error is added up for all basic arithmetic operations. This can be demonstrated in a simple example using the formula for density calculation from equation 15.

$$\rho = \frac{D108 \times 4000000}{[(T106 \times 100) + 273{,}15] \times 287}$$

The pressure sensor D108 has an accuracy of 0,85% and is divided by the record of the T106 sensor which has an accuracy of 0,35%. The remaining values are constant and don't introduce any error. So assuming the pressure is 10 bar, D108 will show a value between 9,915 bar and 10,085 bar. Whereas assuming that the temperature is at 20°C, T106 will show the temperature in the range between 19,93 °C and 20,07 °C, if we now combine each output and divide it we will see that the maximal error will be 1,2%, the sum of both error ranges.

$$\frac{9{,}915}{19{,}93} = 0{,}4975 \quad ; \frac{9{,}915}{20{,}07} = \boxed{0{,}4940} \quad ; \frac{10{,}085}{19{,}93} = \boxed{0{,}5060} \quad ; \frac{10{,}085}{20.07} = 0{,}5025$$

The highest deviation from the true result is represented by the two divisions marked red, which represent the most unfavorable combinations. Comparing these values to the division of the true values multiplied by the sum of both error ranges results in:

$$\frac{10}{20} = 0{,}5 \times 1{,}012 = 0{,}506$$

$$\frac{10}{20} = 0{,}5 \times 0{,}988 = 0{,}494$$

This proves the maximal relative error to be 1,2%. A more general formulation for the relative error of density would look like in the following equation.

$$\frac{\Delta\rho}{\rho} = \frac{\Delta D108}{D108} + \frac{\Delta T106}{T106} \leq 1{,}2\% \qquad \text{(Eq. 20)}$$

Meaning that the estimated density will be in the worst case 1,2% higher or lower than the true value. Following the same principle, the gas rate error can be evaluated. The error of $\boldsymbol{\varepsilon}$ is a combination of two errors introduced by the pressure gauges D108 and D109 and equals 1,01%. For power and root operations, the error needs to be multiplied or divided by the exponent respectively. For the gas-rate equation, the relative error can be calculated as shown in equation 21 (G. Hartwig 2011).

$$\frac{\Delta F104}{F104} = \frac{\Delta D108}{D108} + \frac{\Delta \rho}{\rho} + \left(\frac{\Delta \varepsilon}{\varepsilon}\right) \div 2 = 0{,}85\% + 1{,}2\% + (1{,}1\%) \div 2 = 2{,}60\% \qquad \text{(Eq. 21)}$$

The maximal relative error for estimated gas-rate F104 is therefore 2,60%.

7 Evaluation of modeled flow experiments

In this section, the modeling results of single two and three-phase experiments are described and compared. The processed data from each experiment were fed into a feed-forward neural network. One network for each phase was modeled. The data was partitioned into learning, validation and testing set, for quality control. The artificial neural network architecture was increasing its complexity with each generation, by adding a hidden neuron to the hidden-layer block. The so-called heuristic approach, where the network complexity is not defined in advance but evolves during the learning process. The decision of the best network leading to the most accurate prediction was based on the lowest validation-error. In each generation 10 experts with different initialization weights were trained in a cluster simultaneously, to avoid potential stucking in local minima of the model function. The early stopping criterion was set at 100 epochs, which stops the training of a particular expert in a cluster in every generation if no improvement is reached within 100 epochs. Combined with an error-fluctuation of 1%, which stops the iteration if the average error change is below 1%. The network was a completely connected perceptron with shortcut connections between the input and the output layer. An arbitrary representation of the prediction model evolution is shown in Figure 34.

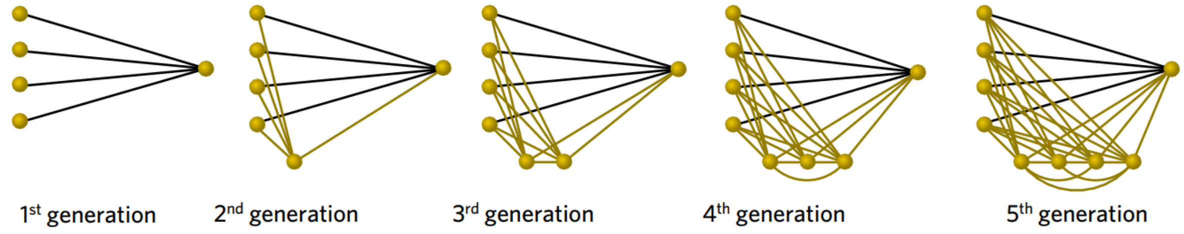

Figure 34. Model architecture evolution (Fruhwirth 2019)

The predicted data was then visualized in cross-plots together with the desired outputs. To judge on the variance and bias with respect to three different subsets, the three-phase experiments include separate plots for each subset. The majority of all experiments led to successful outcomes. The following sections summarize the results of the conducted experiment program and show the root-mean-square errors (RMSE) of each subset listed in tables.

7.1 Single-phase results

In total 3 single-phase measurements were conducted and evaluated. The modeling results are summarized in Table 5.

7.1.1 Water results

Table 5. Single-phase experiments

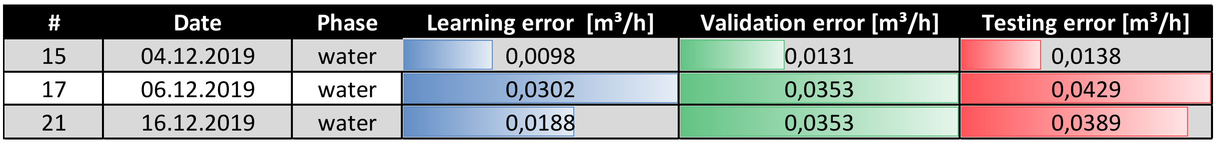

#	Date	Phase	Learning error [m³/h]	Validation error [m³/h]	Testing error [m³/h]
15	04.12.2019	water	0,0098	0,0131	0,0138
17	06.12.2019	water	0,0302	0,0353	0,0429
21	16.12.2019	water	0,0188	0,0353	0,0389

The next figure shows the correlation between the measured and the predicted values plotted on the x and y-axis respectively. In all three graphs, the measured and predicted values are fitting the black line, representing the desired linear correlation. Since the predicted data should match the measured values, the plotted data should follow the black diagonal line over the measured range.

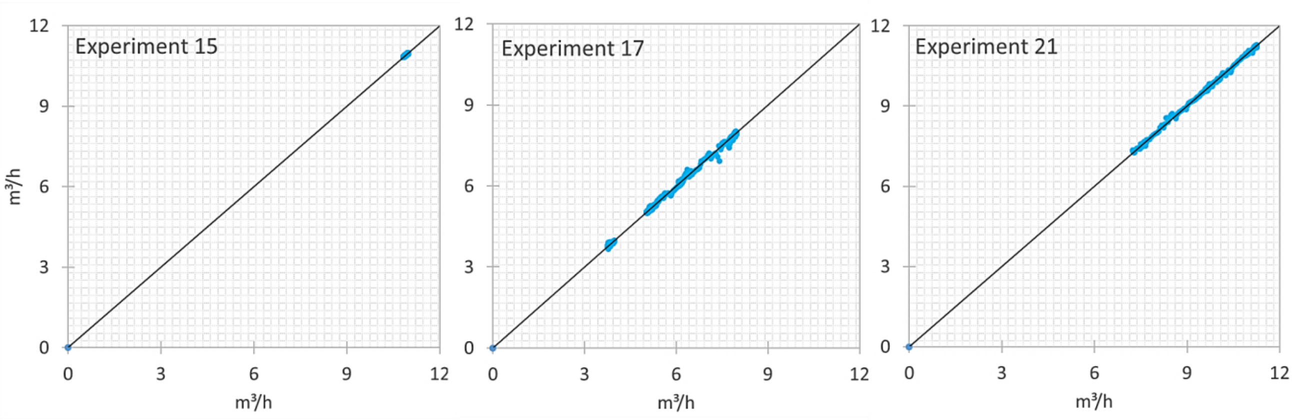

Figure 35. Modeling results of water in single-phase experiments 15, 17 and 21

Figure 35 shows the model outputs of all three experiments with predicted data from all subsets. All three single-phase experiments show a good correlation between measured and predicted data which is reflected by both the absolute numbers and the graphical interpretation. Experiment 17 showed the lowest accuracy, whereas the water-rate is best predicted in experiment 15, where the water was tested at one flow-rate.

7.2 Two-phase results

In this section, the water and gas prediction results of the two-phase experiments are summarized. 11 two-phase experiments with 17 different configurations were tested and evaluated.

7.2.1 Water results

Table 6. Water results of two-phase experiments

#	Date	Phase	Learning error [m³/h]	Validation error [m³/h]	Testing error [m³/h]
1	30.09.2019	water	0,0170	0,0181	0,0191
2	03.10.2019 (1)	water	0,0186	0,0167	0,0210
3	03.10.2019 (2)	water	0,0225	0,0219	0,0218
4	04.10.2019 (1)	water	0,0118	0,0139	0,0129
5	04.10.2019 (2)	water	0,0117	0,0135	0,0117
6	16.10.2019	water	0,0300	0,0287	0,0304
7	18.10.2019	water	0,0149	0,0155	0,0225
8	23.10.2019	water	0,0157	0,0168	0,0156
9	24.10.2019	water	0,0165	0,0167	0,0163
10	21.11.2019	water	0,0227	0,0363	0,0314
16	05.12.2019	water	0,0147	0,0144	0,0155

The generated models show a low variability in error between the individual subsets, which, indicates a low degree of overtraining. From the result summary in Table 6 the experiments 6 and 10 have the lowest prediction accuracy, which is indicated by the highest testing RMSE. Additionally, very valuable information in terms of repeatability can be extracted. In Figure 36 one can see that both experiments, 4 and 5 measure the water rate in the same range. Their prediction accuracy is similar, as reflected by the error results in Table 6. This is an indication of good operational stability and repeatability of the measurements. The best model could be developed based on data from experiments 4 and 5, which introduce the lowest RMS testing-error and the correlation between measured and predicted rates can be observed in Figure 36.

The cross-plots of the remaining experiments can be found in Appendix A: .

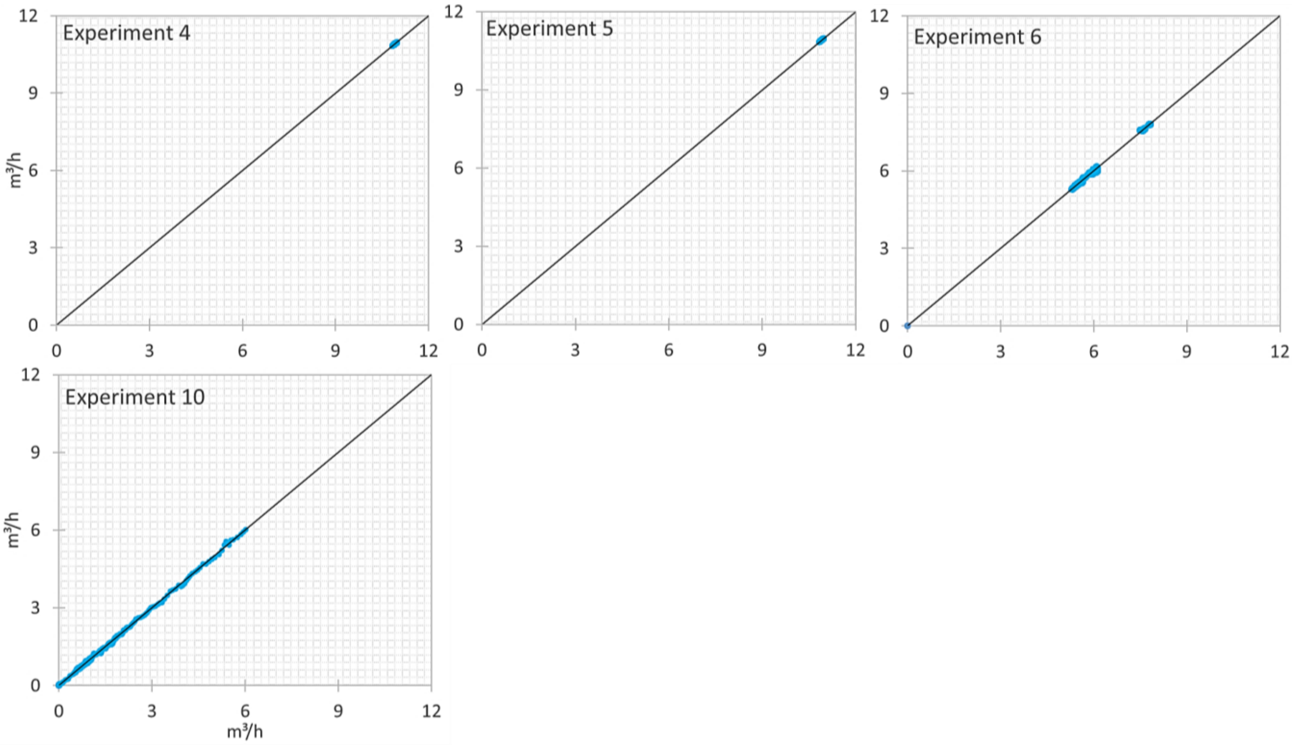

Figure 36. Modeling results of water in two-phase experiments 4, 5, 6 and 10

7.2.2 Gas results

Table 7. Gas results of two-phase experiments

#	Date	Phase	Learning error [kg/h]	Validation error [kg/h]	Testing error [kg/h]
1	30.09.2019	gas	0,0968	0,0984	0,1000
2	03.10.2019 (1)	gas	0,1045	0,0997	0,1162
3	03.10.2019 (2)	gas	0,0962	0,1015	0,1077
4	04.10.2019 (1)	gas	0,0882	0,0983	0,1013
5	04.10.2019 (2)	gas	0,0882	0,0983	0,1013
6	16.10.2019	gas	0,1468	0,1555	0,1523
7	18.10.2019	gas	0,1027	0,1008	0,1018
8	23.10.2019	gas	0,1268	0,1286	0,1394
9	24.10.2019	gas	0,1212	0,1247	0,1290
10	21.11.2019	gas	0,1350	0,2436	0,2169
16	05.12.2019	gas	0,0498	0,0505	0,0607

The prediction accuracies of gas compared to water in two-phase measurements are approximately lower by a factor of 10 and are summarized in Table 7. The generated models show a low error variation between the subsets which indicates a good level of generalization. The lowest accuracy in gas prediction was estimated for experiments 6 and 10. The experiments, 16 and 10 were conducted at elevated gas-rates, higher than in the other listed experiments. Experiment 16 shows the lowest RMS testing-error, whereas, experiment 10 the highest. This indicates that better accuracy is reached when only a few flow rate configurations are tested, as it is in the case of experiment 16, where the gas is flowing at two rates compared to experiment 10, where a wide spectrum between 0-18 kg/h was tested. The correlations between the measured and predicted values of gas in experiments 6, 10 and 16 are summarized in Figure 37, whereas the remaining results can be found in Appendix B.

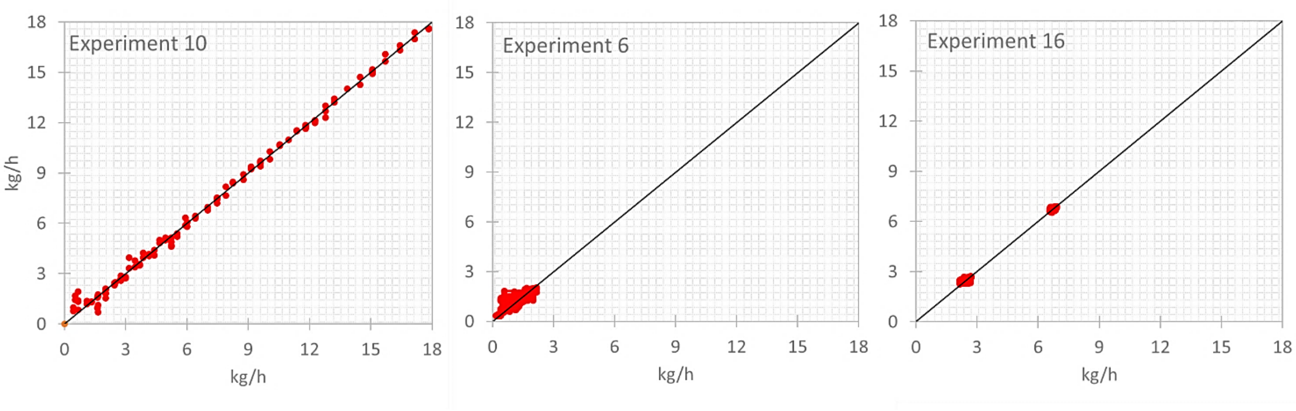

Figure 37. Modeling results of gas in two-phase experiments 6, 10 and 16

From the cross-plots in Figure 37, one can see that at gas rates below 2 kg/h the outlier density is higher than at elevated rates. The cross-plots show an increasing accuracy from left to right showing the lowest validation-error in experiment 16. Experiment 6 and 10 reached the lowest accuracy, nevertheless, the cross-plots shows a good correlation between measured and predicted data and indicate a reliable model performance. The overall prediction accuracy for gas in two-phase experiments is lower compared to water.

7.3 Three-phase results

The evaluation process of three-phase experiments was based on the same principles as shown in single and two-phase results. The main difference is that during the evaluation, cross-plots of all three model subsets namely, learning, validation and testing were created to better judge the results visually and decide which of the experiments delivered the best predictions.

7.3.1 Water results

The measurements show very good results with an absolute testing RMSE below 0,08 m³/h and are shown in Table 8. Experiment 23 led to the highest testing RMSE of 0,075 m³/h. Considering the average flow rate and the highest estimated validation RMSE in experiment 23, the relative validation RMSE results in 1,30%, which is technically satisfactory.

Table 8. Water results of three-phase experiments

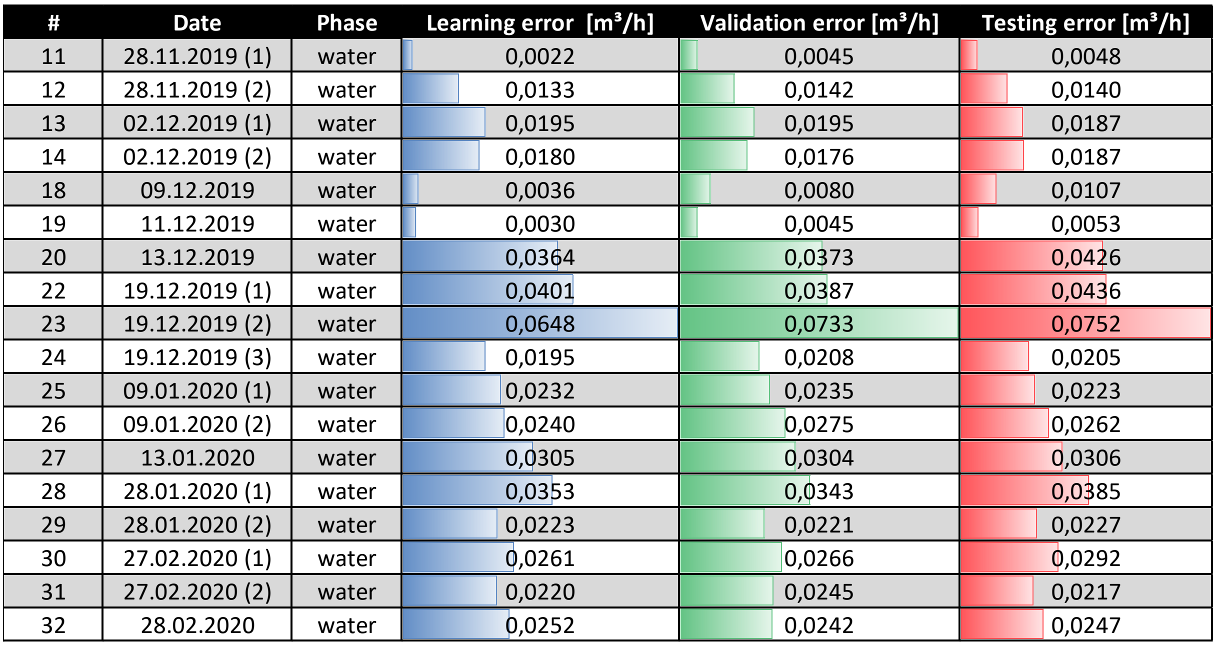

#	Date	Phase	Learning error [m³/h]	Validation error [m³/h]	Testing error [m³/h]
11	28.11.2019 (1)	water	0,0022	0,0045	0,0048
12	28.11.2019 (2)	water	0,0133	0,0142	0,0140
13	02.12.2019 (1)	water	0,0195	0,0195	0,0187
14	02.12.2019 (2)	water	0,0180	0,0176	0,0187
18	09.12.2019	water	0,0036	0,0080	0,0107
19	11.12.2019	water	0,0030	0,0045	0,0053
20	13.12.2019	water	0,0364	0,0373	0,0426
22	19.12.2019 (1)	water	0,0401	0,0387	0,0436
23	19.12.2019 (2)	water	0,0648	0,0733	0,0752
24	19.12.2019 (3)	water	0,0195	0,0208	0,0205
25	09.01.2020 (1)	water	0,0232	0,0235	0,0223
26	09.01.2020 (2)	water	0,0240	0,0275	0,0262
27	13.01.2020	water	0,0305	0,0304	0,0306
28	28.01.2020 (1)	water	0,0353	0,0343	0,0385
29	28.01.2020 (2)	water	0,0223	0,0221	0,0227
30	27.02.2020 (1)	water	0,0261	0,0266	0,0292
31	27.02.2020 (2)	water	0,0220	0,0245	0,0217
32	28.02.2020	water	0,0252	0,0242	0,0247

The following cross-plots are colored according to the presented error-type and follow the scheme presented in Table 8. Where blue is assigned to the learning, green to the validation and red to the testing-error. Cross-plots are used for quality control of the model. If all three plotted subsets show a similar distribution and fit the black diagonal line, a representation of linear correlation, the created network captured the relation between measured and predicted data well. The testing-error is significant to see how the model reacts on statistically independent data which was not used during training and should be in the same range as the validation-error. If the difference between both is kept low the model variance is low, which indicates a good degree of generalization. Figure 38 shows the cross-plots of experiment 11 with the highest accuracy and experiment 23, which reached the lowest prediction accuracy. The plotted data of both experiments follow well the black diagonal line, indicating a low bias. Both experiments show a very low deviation between the testing and validation subset and are therefore reliable, although their error range differs significantly. The graphical results of the remaining experiments are enclosed in Appendix C.

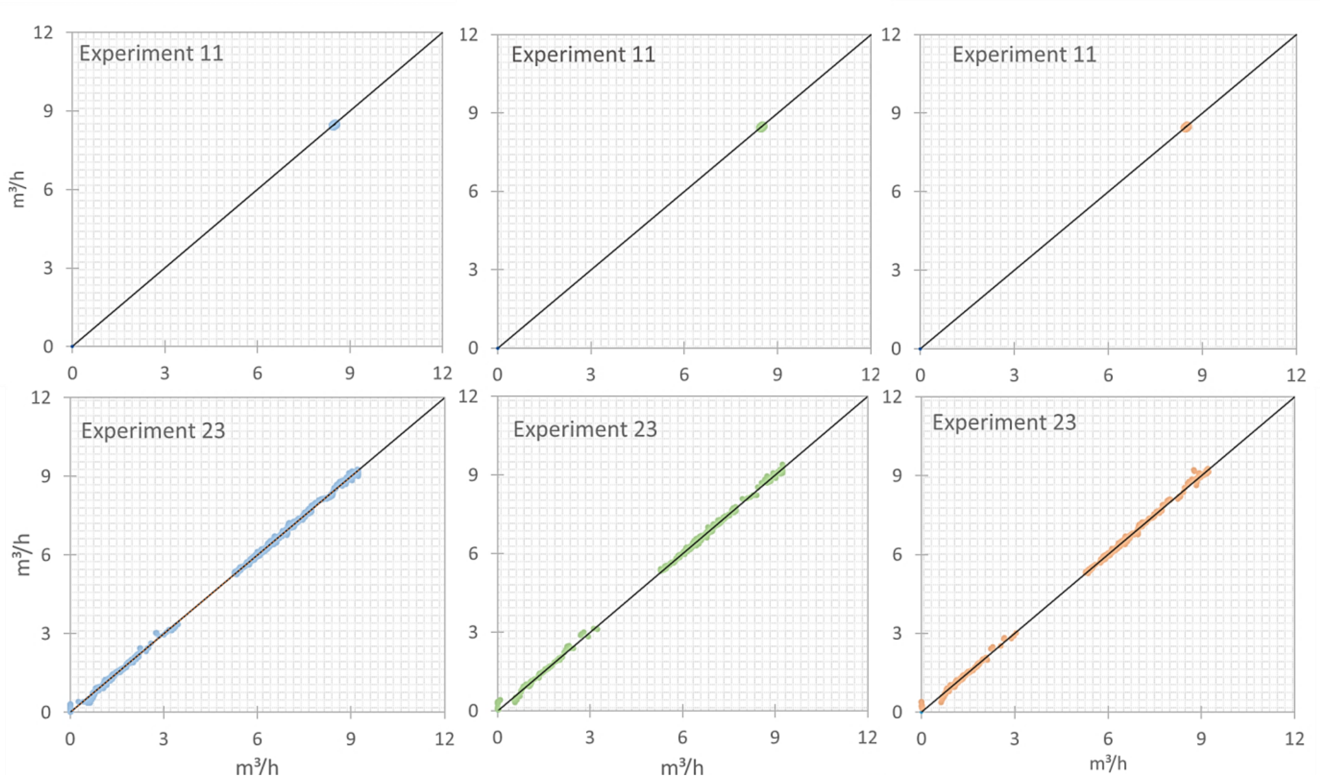

Figure 38. Modeling results of water in experiment 11 and 23

7.3.2 Oil results

All of the experiments, except experiment 20, show very good prediction results with a testing RMSE below 0,03 m³/h. The highest relative testing RMSE estimated in experiment 20 results in 5,15% which is in the range of conventional test-separators. The results of all three-phase experiments are summarized in Table 9.

Table 9. Oil results of three-phase experiments

#	Date	Phase	Learning error [m^3/h]	Validation error [m^3/h]	Testing error [m^3/h]
11	28.11.2019 (1)	oil	0,0020	0,0028	0,0036
12	28.11.2019 (2)	oil	0,0060	0,0066	0,0063
13	02.12.2019 (1)	oil	0,0041	0,0046	0,0043
14	02.12.2019 (2)	oil	0,0033	0,0035	0,0037
18	09.12.2019	oil	0,0024	0,0044	0,0074
19	11.12.2019	oil	0,0020	0,0036	0,0036
20	13.12.2019	oil	0,0870	0,1032	0,1227
22	19.12.2019 (1)	oil	0,0125	0,0155	0,0262
23	19.12.2019 (2)	oil	0,0169	0,0211	0,0184
24	19.12.2019 (3)	oil	0,0039	0,0041	0,0040
25	09.01.2020 (1)	oil	0,0079	0,0085	0,0082
26	09.01.2020 (2)	oil	0,0073	0,0075	0,0076
27	13.01.2020	oil	0,0112	0,0106	0,0121
28	28.01.2020 (1)	oil	0,0154	0,0154	0,0170
29	28.01.2020 (2)	oil	0,0101	0,0099	0,0102
30	27.02.2020 (1)	oil	0,0031	0,0032	0,0034
31	27.02.2020 (2)	oil	0,0022	0,0029	0,0034
32	28.02.2020	oil	0,0047	0,0052	0,0057

Figure 39 shows the prediction errors of all three subsets generated from experiments 11 and 20. Both experiments are visualized in the same manner as previously shown for the water-phase, using cross-plots of measured and predicted flowrates plotted on the x and y-axis respectively. Experiment 11 shows the lowest validation-error, which is reflected by the data-points fitting the black line in the cross-plot. Whereas, experiment 20 reached the highest validation-error. The data points are not perfectly fitting the black line but rather form a data cloud around it. Nevertheless, the plots show a low deviation between the individual subsets and indicate a good degree of generalization. Apart from experiment 20 the overall prediction accuracy of the listed experiments is comparable. All experiments show low variability between the validation and testing subset and are technically useful. The cross-plots of the remaining experiments are summarized in Appendix D.

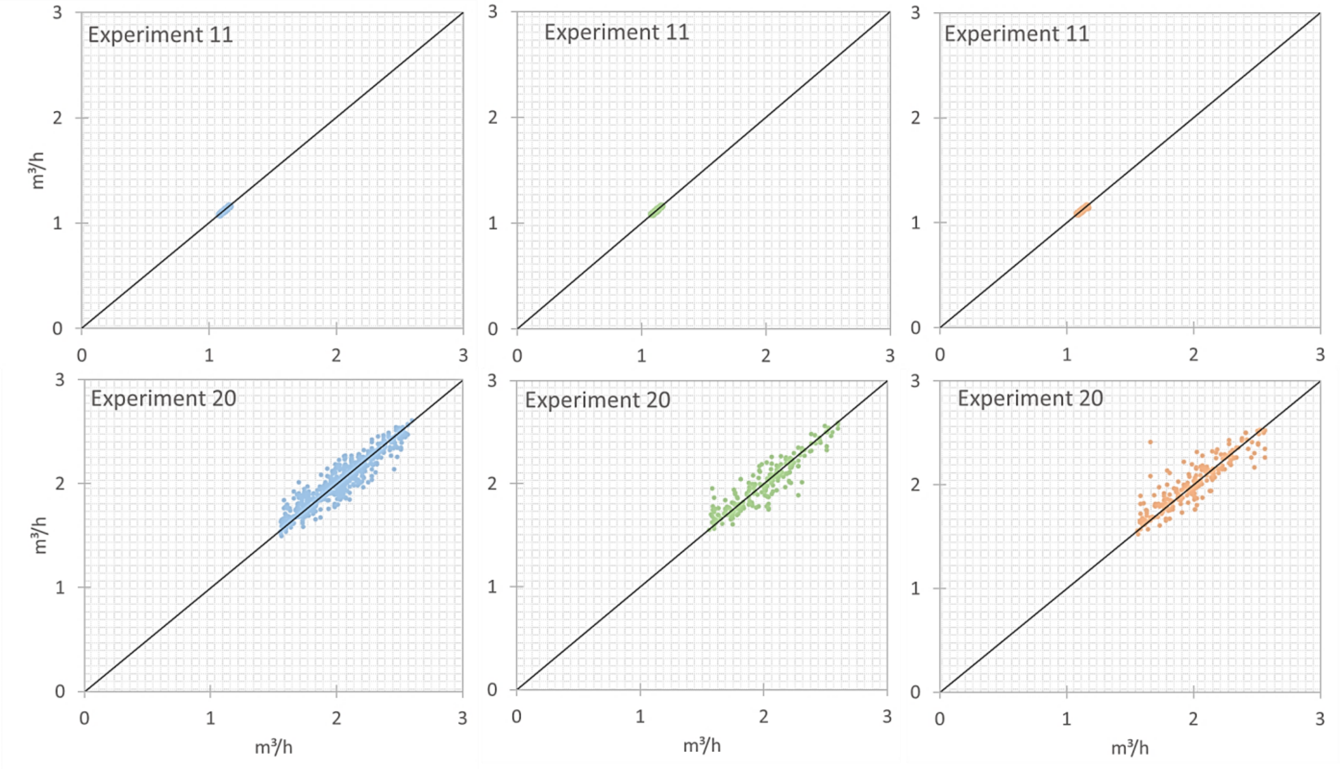

Figure 39. Modeling results of oil in experiment 11 and 20

7.3.3 Gas results

The prediction results of the gas phase are summarized in Table 10. The validation RMSE in the gas prediction models is highest in experiments 18 and 19. The remaining experiments show comparable errors between 0,01 kg/h and 0,07 kg/h. In the experiments 11 to 14 and 24, where gas rates below 2 kg/h were tested the modeling results reach higher accuracies. Whereas, the remaining experiments were tested above 2 kg/h and reached lower accuracies. The situation is reversed when the predicted results are normalized by the average flow rate, indicating that higher accuracies are reached at elevated rates as shown in Table 12.

Table 10. Gas results of three-phase experiments

#	Date	Phase	Learning error [kg/h]	Validation error [kg/h]	Testing error [kg/h]
11	28.11.2019 (1)	gas	0,0076	0,0156	0,0157
12	28.11.2019 (2)	gas	0,0312	0,0328	0,0346
13	02.12.2019 (1)	gas	0,0339	0,0364	0,0369
14	02.12.2019 (2)	gas	0,0308	0,0335	0,0276
18	09.12.2019	gas	0,0264	0,1449	0,1599
19	11.12.2019	gas	0,0900	0,0839	0,1141
20	13.12.2019	gas	0,0553	0,0506	0,0569
22	19.12.2019 (1)	gas	0,0669	0,0590	0,0652
23	19.12.2019 (2)	gas	0,0638	0,0636	0,0703
24	19.12.2019 (3)	gas	0,0347	0,0365	0,0373
25	09.01.2020 (1)	gas	0,0401	0,0404	0,0404
26	09.01.2020 (2)	gas	0,0445	0,0485	0,0481
27	13.01.2020	gas	0,0514	0,0561	0,0535
28	28.01.2020 (1)	gas	0,0666	0,0717	0,0700
29	28.01.2020 (2)	gas	0,0389	0,0410	0,0393
30	27.02.2020 (1)	gas	0,0535	0,0494	0,0595
31	27.02.2020 (2)	gas	0,0502	0,0461	0,0506
32	28.02.2020	gas	0,0504	0,0551	0,0509

Figure 40 shows the prediction errors of gas in experiment 11 and 18, which are visualized in the same manner as previously shown for the water and oil-phase. The cross-plots of the remaining experiments can be found in Appendix E.

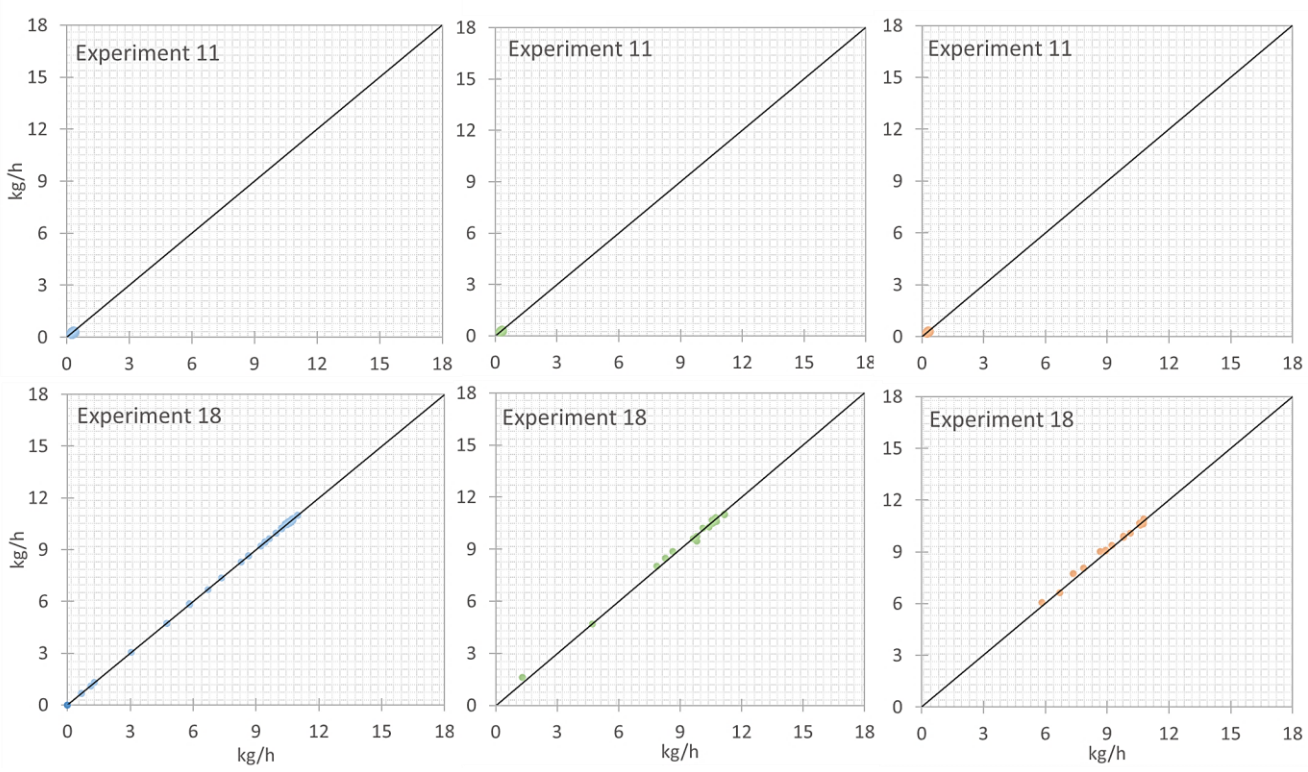

Figure 40. Modeling results of oil in experiment 11 and 18

Experiment 18 with the lowest prediction accuracy shows a low deviation from the black line in all three subsets, which indicates a good quality of the model. Experiment 11 reached the highest accuracy which is also reflected in the cross-plots by data-points fitting the black line. The difference between both experiments is significant, nevertheless, the cross-plots of both experiments show low deviation and indicate a good degree of generalization. Moreover, the cross-plots of the remaining experiments show similar accuracies, which is reflected in Table 10 showing that the validation and testing-error are nearly equal and the model performances are good.

8 VFM

The VFM-model was created based on 19 features and three variables the water, oil and gas-rate, which are shown in Table 11. Each variable input consists of 34488 data points. Altogether the model is based on 724248 data-points. Where 60% were used for learning and 20% for each, validation and testing. Based on the learning data the network was created and learned to predict the desired flow rates. With the validation subset, the network was tuned and updated to fit the newly introduced data. Finally, the algorithm feeds the testing data into the validated network and performs the flow rate calculations based on the network algorithm created during training. The testing subset is important since it is statistically independent and delivers information about the model variance. If all three calculated absolute errors are similar, it implies a low grade of overtraining. Since all three-phase measurements showed satisfactory modeling results with low deviations between each error subset, the VFM utilizes processed data from all three-phase experiment. For the VFM, a heuristic modeling approach, as for the individual experiments, was used. The network complexity was increasing with every model generation starting with a multi-linear regression and finishing with a network consisting of 10 hidden neurons. Water, oil and gas were modeled individually to avoid any interference due to the different magnitudes of the output. The chosen ANN architecture is an improved completely connected perceptron with shortcut connections between input and output. The learning process is based on error-backpropagation. It uses an adaptive learning algorithm that adjusts the weights according to the estimated local error gradient and is, therefore, able to converge faster.

Table 11. VFM input variables

Name	Description	Range	Error	Unit
ACC101X_A_conv	Framework acceleration	(+/-) 2	1,00%	g
ACC101Y_A_conv	Framework acceleration	(+/-) 2	1,00%	g
ACC101Z_A_conv	Framework acceleration	(+/-) 2	1,00%	g
D101_A_conv	Water tank pressure	0-40	1,00%	bar
D101_S_conv	Desired water tank pressure	0-40	1,00%	bar
D104_A_conv	Pressure wellhead	0-200	0,30%	bar
D104_S_conv	Wellhead-valve position	0-100	-	%
D106_A_conv	ESP intake pressure	0-200	0,30%	bar
D107_A_conv	ESP discharge pressure	0-200	0,30%	bar
D108_A_conv	Static air pressure	0-40	0,85%	bar
D109_A_conv	Dynamic air pressure	0-0,5	0,16%	bar
M101_S_conv	Desired motor speed	0-60	-	Hz
DS101_A_conv	Shaft torque	0-500	0,10%	Nm
F101_A_conv	Water rate	0-25	3,00%	m^3/h
F103_A_conv	Oil rate	0,2-32	0,30%	m^3/h
F104_A_conv	Gas rate	-	2,60%	kg/h
FU101_Current	FC- current	-	0,10%	A
FU101_Power	FC- power	-	3,10%	kW
T101_A_conv	Temperature water tank	0-100	0,35%	°C
T104_A_conv	ESP intake temperature	0-100	0,35%	°C
T105_A_conv	ESP discharge temperature	0-100	0,35%	°C
T106_A_conv	Air temperature	0-100	0,35%	°C

8.1 Prediction accuracy

For the development of the VFM-model, eighteen three-phase experiments were used. The highest relative errors from the three-phase experiments are related to the gas phase prediction, as seen in Table 12. Particularly the experiments 11 to 14 and 24 show the lowest accuracy in predicting gas. The lowest prediction accuracy of oil was reached in experiments 20. Whereas, water has the lowest accuracy in experiment 23.

Table 12. Relative RMSE summary of three-phase measurements

#	Date	Type	relative validation RMSE water	relative validation RMSE oil	relative validation RMSE gas
11	28.11.2019 (1)	3-Phase	0,05%	0,25%	5,39%
12	28.11.2019 (2)	3-Phase	0,23%	0,26%	8,34%
13	02.12.2019 (1)	3-Phase	0,18%	0,55%	4,07%
14	02.12.2019 (2)	3-Phase	0,17%	0,52%	4,60%
18	09.12.2019	3-Phase	0,11%	0,29%	1,53%
19	11.12.2019	3-Phase	0,06%	0,27%	2,24%
20	13.12.2019	3-Phase	0,59%	5,15%	0,63%
22	19.12.2019 (1)	3-Phase	0,67%	1,14%	0,73%
23	19.12.2019 (2)	3-Phase	1,30%	1,57%	0,72%
24	19.12.2019 (3)	3-Phase	0,19%	0,49%	4,06%
25	09.01.2020 (1)	3-Phase	0,36%	0,66%	0,51%
26	09.01.2020 (2)	3-Phase	0,92%	0,62%	1,62%
27	13.01.2020	3-Phase	0,46%	0,81%	0,70%
28	28.01.2020 (1)	3-Phase	0,55%	0,98%	0,87%
29	28.01.2020 (2)	3-Phase	0,28%	0,62%	0,37%
30	27.02.2020 (1)	3-Phase	0,28%	0,32%	0,68%
31	27.02.2020 (2)	3-Phase	0,27%	0,57%	0,28%
32	28.02.2020	3-Phase	0,29%	0,30%	0,37%

Despite, the error degree in the individual measurements the entire processed data delivered promising results and was completely utilized in the VFM. For this purpose the data used for modeling the three-phase experiments were merged and modeled at once, to create a network consisting of a wide spectrum of different flow configurations. The simulation of one VFM prediction model took about 7 hours and delivered technically desirable results, which are shown in Figure 41, where the error-convergence of the VFM-model of water, oil and gas is shown. The blue line represents the validation-error evolution of water, green of oil and red of gas.

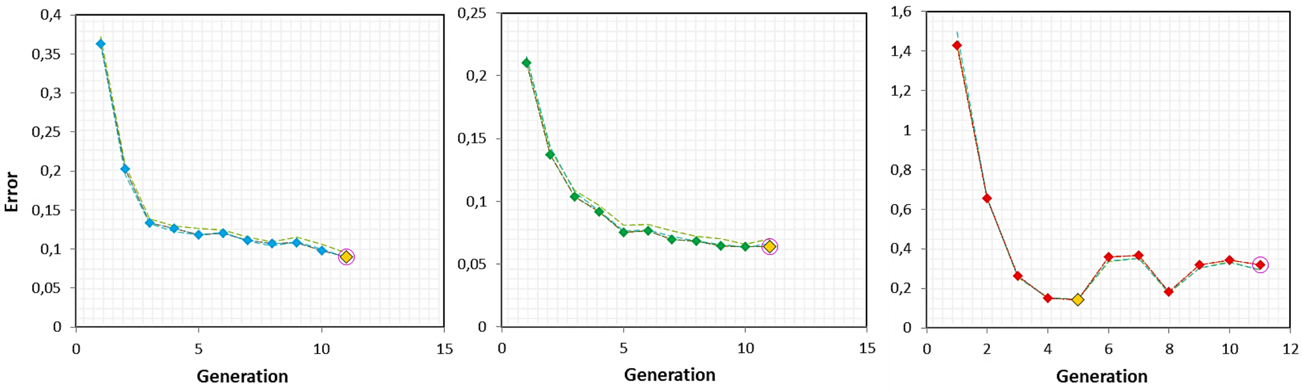

Figure 41. VFM validation-error evolution for water, oil and gas

The graph shows how the model error is changing with increasing model complexity. The yellow point in each of the plots represents the generation with the lowest average validation-error. The optimal learning point is reached at the 11th generation for the water and oil rate, which indicates a network with 10 hidden units in the hidden-layer block. The gas rate is modeled best by a network with 4 hidden units, which indicates a lower complexity of the problem. The summary of the calculated RMS learning, validation and testing-error for all three phases is shown in Table 13.

Table 13. VFM-model results

Phase	Unit	Learning error	Validation error	Testing error
water	m³/h	0,0956	0,0899	0,0894
oil	m³/h	0,0704	0,0638	0,0666
gas	kg/h	0,1439	0,1426	0,1451

The models reached a relative validation RMSE of 1,20% for water, 4,85% for oil and 2,40% for gas. These values were calculated based on the RMS testing error from Table 13 and normalized by the average measured flow rate, 7,52 m³/h for water, 1,32 m³/h for oil and 5,94 kg/h for gas. To see the tested ranges and their distribution, histograms for water, oil and gas were generated and are shown in the following Figure 45, Figure 46 and Figure 47 respectively. Where the left y-axis shows the frequency of the measured rates and the x-axis is split into representative bins of the respective flowrates in m³/h for water, oil and kg/h for gas. The second y-axis captures the cumulative occurrence of the measured rates in percent.

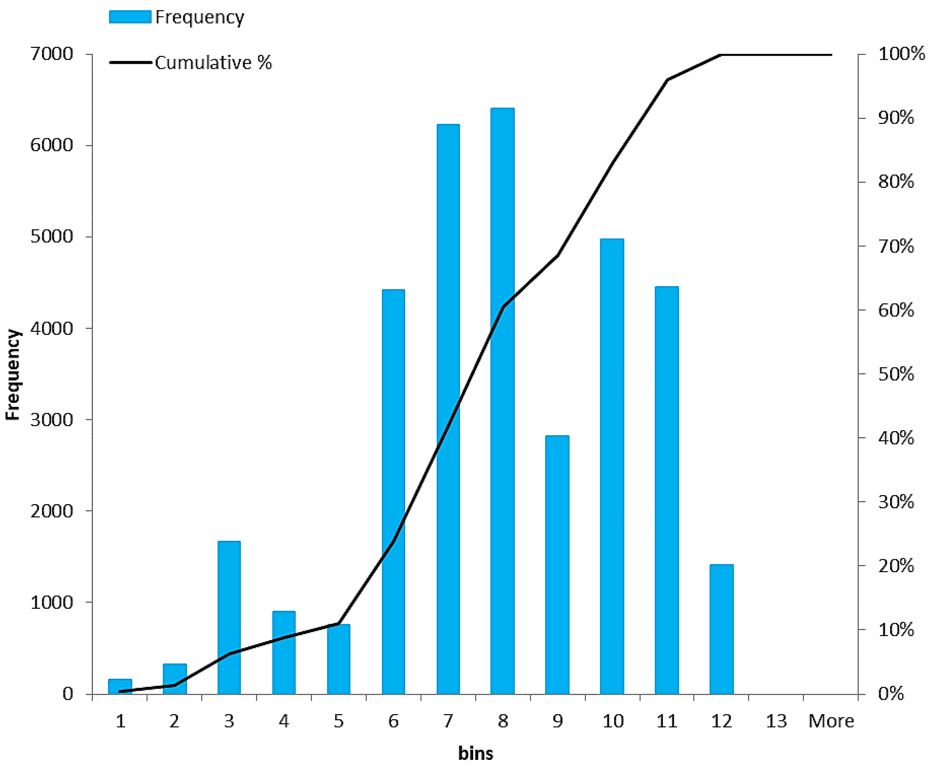

Figure 42. Water-rate distribution

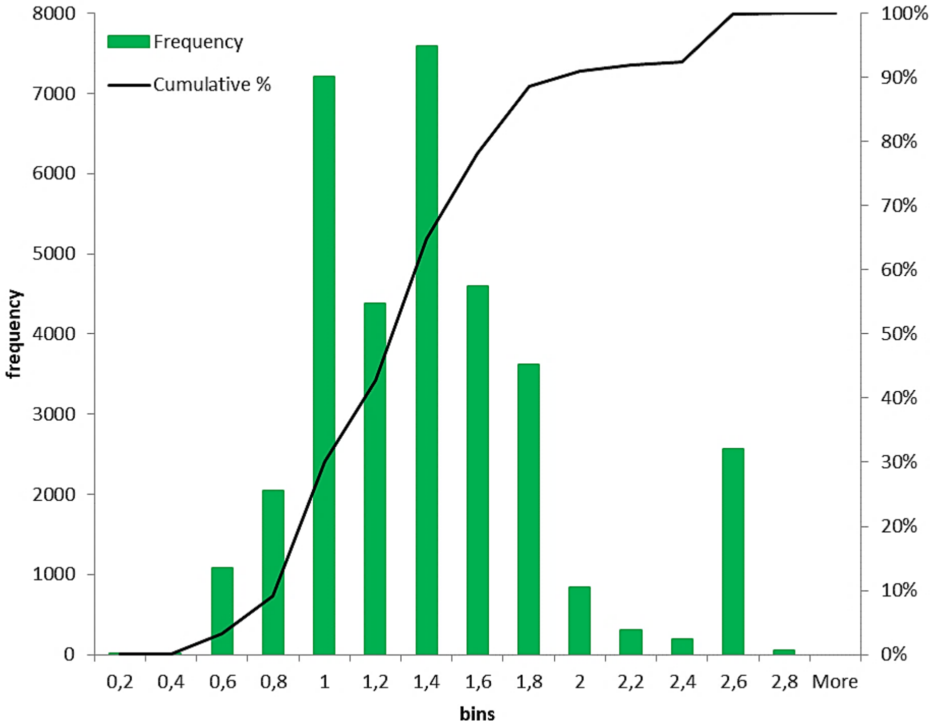

Figure 43. Oil-rate distribution

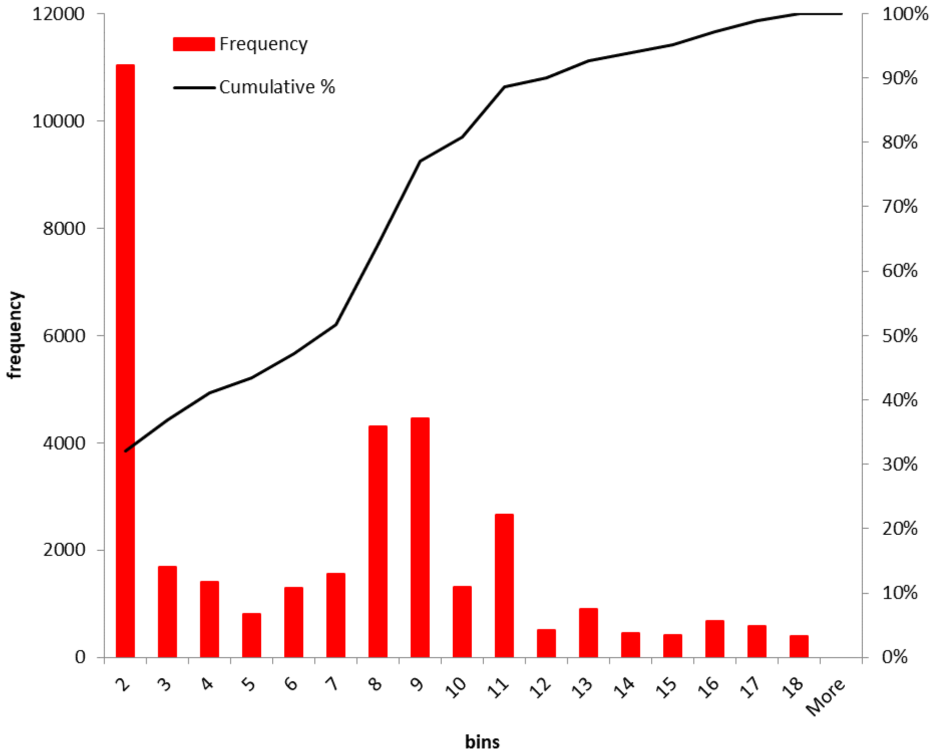

Figure 44. Gas-rate distribution

Finally, to visualize the relationship between the measured and predicted flow rates, cross-plots were used as in the evaluation of three-phase experiments. The measured water, oil, and gas rates were plotted with the predicted values on the x and y-axis respectively. The following figures show the learning in blue, validation in green and testing-subset in red of each phase in a cross-plot.

8.1.1 Water-phase:

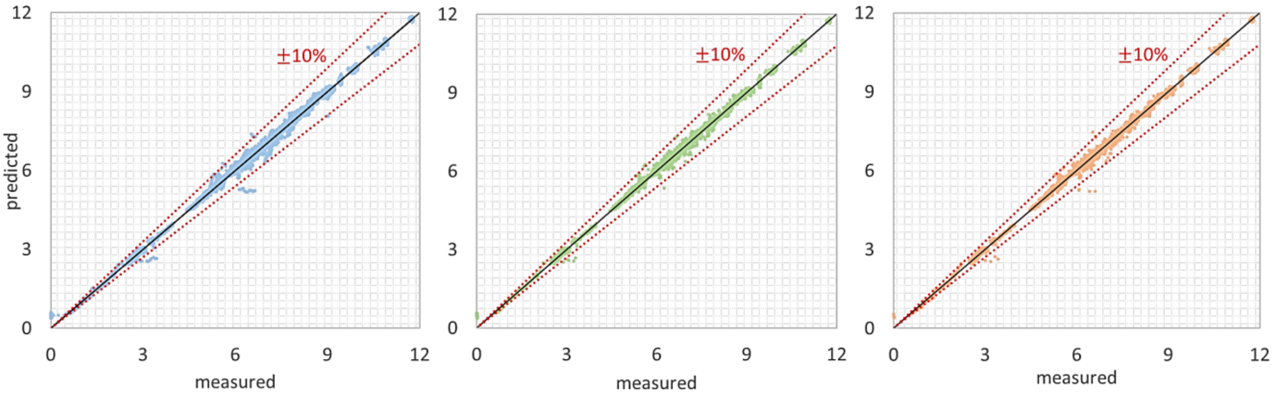

Figure 45. VFM water rate cross-plots

From the cross-plots, in Figure 45 one can immediately see the linear correlation between the measured and predicted rates. The data distribution covers the total tested range and follows the black line similarly in each plotted subset. The plotted results have a minor deviation between each other and indicate low variability of the algorithm and a reasonable degree of generalization. The two red dotted lines represent the window within 10% deviation. The estimated relative validation RMSE for water is 1,20%

8.1.2 Oil-phase:

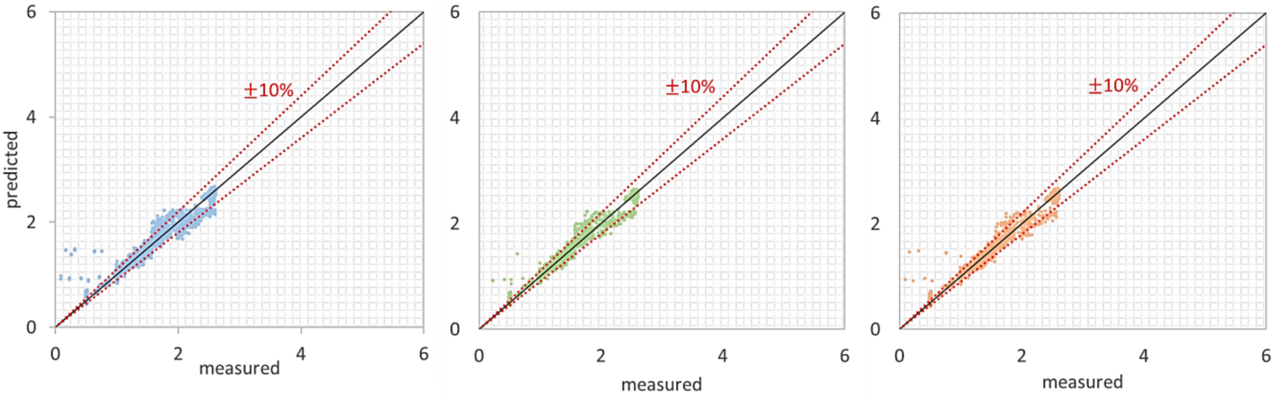

Figure 46. VFM oil-rate cross-plots

Figure 46 shows that the prediction accuracy of oil is lower than the accuracy of water since it shows a higher density of points laying off the black line and the 10% margin. Nevertheless, a relative validation RMSE of 4,85% is technically satisfactory and comparable with conventional test-separators. Some of the data points plotted in Figure 46 shows an increased deviation at oil rates below 1 m³/h and leads to an increased number of outliers. The degree of correlation increases between 1 m³/h and 1,8 m³/h. This indicates an operational range where good prediction results were reached. From 1,8 m³/h to 2 m³/h, one can identify a spreading shape of the data localized slightly above and below the black line. Between roughly 2,6 m³/h and 2,8 m³/h, a steady operational mode is captured. It is characterized by the isolated data cloud, which is localized on the black line and within the 10% margin. The three cross-plots show minor differences and indicate a low degree of overtraining.

8.1.3 Gas-phase:

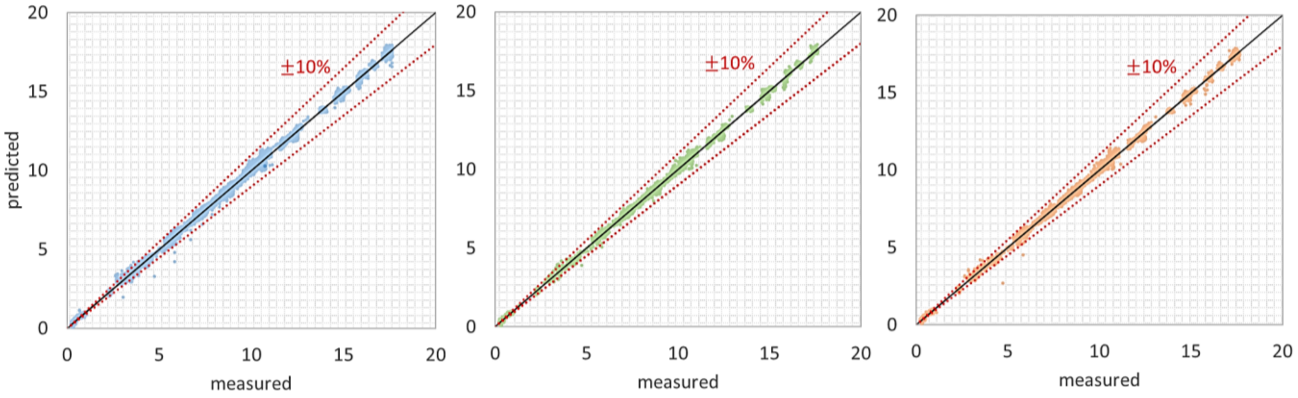

Figure 47. VFM gas-rate cross-plots

Similar to water, the gas prediction in Figure 47 reaches a very high accuracy with a relative validation RMSE of 2,40%. The data is fitting the black line well along the entire test-range. Between 2 kg/h and 12 kg/h, the data is continuously covering the black line. Whereas, at elevated rates, individual flow configurations can be detected. These are very good seen in the learning subset cross-plot, where 5 isolated data clusters are fitting the black line. The overall correlation between the measured and predicted flow rates is evenly distributed along the entire range with an decreasing accuracy at rates below 2 kg/h.

8.2 Case study: Importance of acceleration sensors

The three acceleration sensors used during the experimental program were attached to the steel framework where the ESP was hanging. Apart from the ESP other equipment like pipes, tubes and cables were attached and added to the same construction during the experimental period. The total load on the framework was frequently changing during the work in the PTF, therefore a sensibility analysis of the VFM to the acceleration sensors was conducted. The aim was to analyze the impact of these sensors on the final VFM-model. Following the same procedure, a new VFM model was created based on 16 features. Three separate prediction models for water oil and gas were generated and their results are summarized in Table 14.

Table 14. VFM results without acceleration input

Phase	Unit	Learning error	Validation error	Testing error
water	m^3/h	0,0976	0,0904	0,0917
oil	m^3/h	0,0649	0,0581	0,0603
gas	kg/h	0,1016	0,1049	0,0998

The difference in the results is small, although the prediction accuracy for oil and gas could be improved by neglecting the acceleration data, which is reflected in the testing-error of both, shown in Table 14. Whereas, the testing-error of water is higher in the model where accelerators are neglected. This example indicates that the sensitivity of the predicted rates to the input variables is not uniform. Nevertheless, the output might be slightly different, if for example the subset partitioning is done differently, therefore the importance of acceleration sensors in the prediction of water, oil and gas in the PTF was minor since no significant loss or improvement in prediction accuracy was reached. The relative validation RMSE for water, oil and gas result in 1,20%, 4,41% and 1,76 respectively. Which indicates that the prediction accuracy for oil and gas could be improved, whereas for water it remains the same.

8.3 Case Study: Principal Component Analysis (PCA)

To evaluate which sensor-data is capturing the most information required for accurate multiphase flow prediction, a PCA was conducted. All 19 features except the three adjustable features namely, D104_S control-valve position at the wellhead, P101_S the desired water tank pressure and M101_S the desired pump speed, were analyzed to determine their significance in multiphase flow prediction.

PCA is used to reduce the dimension of the network by maximizing the variance. Features are selected based on the eigenvalues derived from the 16 x 16 covariance matrix by calculating the characteristic root. The eigenvalues are proportional to the total explained variance in the data which is proportional to the captured information. Principle components describe both, the direction and quantity of maximum data variance. The eigenvalue with the highest variance is the first principle component PC1. Typically, the first few principal components are capable of explaining the majority of the introduced variance. The sum of the eigenvalue coefficients equals the number of input variables. By summing-up, the eigenvalues and dividing them by their individual contribution, the percentage of the total variance captured in each principal component can be quantified. From the eigenvectors, the contribution of each feature to the derived principal components was determined. The sum of the squared eigenvector weights equals one for every principal component, where positive coefficients indicate a proportional, and negative coefficients indicate a reciprocal relationship between the principal component and the feature (Walde). Table 15 shows the derived eigenvalues and the contribution of each principal component to the total variance.

Table 15. Principle components and their variance contribution

PC	Variance	Proportion [%]	Cumulative proportion
1	5,549	0,347	0,347
2	3,348	0,209	0,556
3	2,294	0,143	0,699
4	1,717	0,107	0,807
5	1,119	0,070	0,877
6	0,929	0,058	0,935
7	0,339	0,021	0,956
8	0,294	0,018	0,974
9	0,211	0,013	0,987
10	0,087	0,005	0,993
11	0,072	0,004	0,997
12	0,027	0,002	0,999
13	0,011	0,001	1
14	0,003	0,000	1
15	0,001	0,000	1
16	0,000	0,000	1

Based on Table 15, one can see that more than 80% of the variance can be explained by the first four principal components. The next step was to identify the contribution of each sensor to the variance of principal components 1,2,3 and 4. This can be done based on the eigenvectors summarized in Table 16. Eigenvectors are a list of weights, which describe how each individual sensor contributes to the determined variance of the principal component. The contribution of the sensors to the variance of PC1 to PC4 is evenly distributed, showing that two sensors ACC101X and D101_A are of least importance.

Table 16. Sensor contribution to principal components

Sensor	PC1	PC2	PC3	PC4	Contribution [%]
ACC101X	-0,002	-0,034	0,101	-0,353	2%
ACC101Y	0,056	-0,108	0,322	-0,561	6%
ACC101Z	-0,086	0,128	-0,331	0,448	5%
D101_A	-0,203	0,092	-0,091	0,157	2%
D104_A	-0,002	-0,525	-0,084	0,040	7%
D106_A	0,258	0,284	-0,328	-0,218	8%
D107_A	-0,012	-0,527	-0,071	0,048	7%
D108_A	0,333	0,121	-0,234	-0,209	7%
D109_A	0,252	0,295	-0,313	-0,199	7%
DS101_A	0,327	-0,027	-0,115	0,246	6%
FU101_current	0,192	-0,309	-0,375	-0,068	7%
FU101_power	0,219	-0,359	-0,302	-0,102	7%
T101_A	-0,374	0,021	-0,261	-0,174	8%
T104_A	-0,353	0,002	-0,280	-0,206	7%
T105_A	-0,344	-0,010	-0,282	-0,227	7%
T106_A	-0,364	0,022	-0,160	-0,048	6%

The new VFM model for water, oil and gas was based on sensors with the highest variance contribution, which were calculated using the sensor loading factors in Table 16. The percentual contribution or score was calculated by multiplying the variance of the principal component from Table 15 with the square of the sensor loading factor, summed over the first four principal components and divided by 12,91, the sum of the variances PC1 to PC4. In total, 10 sensors, marked grey in Table 16, with a contribution of at least 7%, were selected and utilized together with the three adjustable features to create new models and investigate the impact on prediction accuracy. The RMS errors of the new VFM models for water, oil and gas based on the PCA are shown in Table 17.

Table 17. VFM results based on PCA

Phase	Unit	Learning error	Validation error	Testing error
water	m³/h	0,1198	0,1127	0,1136
oil	m³/h	0,0756	0,0706	0,0704
gas	kg/h	0,3054	0,3043	0,3003

The overall prediction accuracy of the PCA based VFM is lower, because 6 input sensors were neglected. For all three phases, a low deviation between the individual subset-errors could be reached and indicate herewith a low variability of the model. The RMS validation-error of water and oil is in the same range, showing a deviation below 0,02 m³/h for both, compared to the initial VFM model. Whereas, the prediction accuracy of gas based on the RMS validation-error increased significantly from roughly 0,14 to 0,3 kg/h, which is still a technically desirable result with a relative validation RMSE of 5,12%. Water and oil reached relative validation RMSEs of 1,50% and 5,37% respectively. Based on these results the total number of required features could be reduced to 13 features, which are listed in Table 18.

Table 18. Reduced VFM input data

Name	Description
D101_S_conv	Desired water tank pressure
D104_A_conv	Pressure wellhead
D104_S_conv	Wellhead-valve position
D106_A_conv	ESP intake pressure
D107_A_conv	ESP discharge pressure
D108_A_conv	Static air pressure
D109_A_conv	Dynamic air pressure
M101_S_conv	Desired motor speed
FU101_Current	FC- current
FU101_Power	FC- power
T101_A_conv	Temperature water tank
T104_A_conv	ESP intake temperature
T105_A_conv	ESP discharge temperature

9 Conclusion

VFMs are a promising approach for multiphase flow prediction due to its low costs and real-time monitoring capabilities. They are also easy to integrate with an already existing software solution. The VFM-model developed in the PTF is capable of predicting flow rates with a relative RMSE of 1,20% for water, 4,85% for oil and 2,40% for gas. The next step in the development of the VFM-model would be further testing with field-data. A well with a similar setup with respect to the measured range and fluid fractions would be recommendable for further VFM testing and tuning. The potential of a VFM, to be used as backup-system for metering operations and failure prediction is therefore approved but indicates that further investigations in this field are required to use it as a standalone solution. Especially long-term field tests and parallel applications with test-separators at different conditions are recommendable, to adjust and tune the algorithm. There is still a lack of field-experiments and publicly available test-data that would allow a better judgment on the efficiency and accuracy of VFMs in field applications.

Due to the technical and spatial limitations of the PTF, investigations at elevated oil rates were not performed. Anyhow it would be interesting to test the VFM at higher oil rates and investigate if a similar prediction accuracy as for water or gas could be reached. This work contributes to the overall understanding of data-based VFMs and confirms that information stored in readily accessible production data have a huge unexhausted potential in terms of multiphase flow prediction.

The following points summarize the main advantages and disadvantages of data-based models:

(+) No detailed knowledge about the system physics

(+) Low computational costs

(+) Quick and easy update with new data

(+) Fast incorporation of new parameters

(-) Limited experience in field application

(-) Requires calibration and re-training, if field conditions differ significantly

(-) Requires a good understanding of ANN methodology

10 References

AL-Qutami, Tareq Aziz; Ibrahim, Rosdiazli; Ismail, Idris; Ishak, Mohd Azmin (2018): Hybrid Neural Network And Regression Tree Ensemble Pruned By Simulated Annealing For Virtual Flow Metering Application. In: *Expert Systems with Applications* 93, S. 72–85. DOI: 10.1016/j.eswa.2017.10.014.

Amin, A. (2015): Evaluation of Commercially Available Virtual Flow Meters (VFMs). In: Offshore Technology Conference. Offshore Technology Conference. Houston, Texas, USA, 2015-05-04: Offshore Technology Conference.

Andrianov, Nikolai (2018): A Machine Learning Approach for Virtual Flow Metering and Forecasting. Online verfügbar unter http://folk.ntnu.no/skoge/prost/proceedings/ifac-oogp18/OOGP18/0023.pdf, zuletzt geprüft am 26.05.2020.

Bikmukhametov, Timur; Jäschke, Johannes (2020): First Principles and Machine Learning Virtual Flow Metering: A Literature Review. In: *Journal of Petroleum Science and Engineering* 184, S. 106487. DOI: 10.1016/j.petrol.2019.106487.

Corneliussen et al. (2005): Handbook of Multiphase Flow Metering. Unter Mitarbeit von Corneliussen, Sidsel: BP Norway Couput, Jean-Paul: TOTAL Dahl, Eivind: Christian Michelsen Research Dykesteen, Eivind: Roxar Flow Measurement Frøysa, Kjell-Eivind: Christian Michelsen Research Malde, Erik: ConocoPhillips Moestue, Håkon: Norsk Hydro Moksnes, Paul Ove: Framo and Schlumberger Scheers, Lex: Shell GS International Tunheim, Hallvard: Norsk Hydro und co-ordinated by Eivind Dahl, Christian Michelsen Research AS. 2. Aufl. Online verfügbar unter https://nfogm.no/wp-content/uploads/2014/02/MPFM_Handbook_Revision2_2005_ISBN-82-91341-89-3.pdf.

Dellarole, E.; Bonuccelli, M.; Antico, L.; Faluomi, V. (2005): Virtual Metering And Flow Allocation: Models, Tools And Field Results. In:. Offshore Mediterranean Conference and Exhibition: Offshore Mediterranean Conference.

DIN EN 60751: ti-5_kennlinien-pt100-widerstaende-nach-toleranzklassen. Online verfügbar unter https://www.electronic-sensor.de/attachments/article/68/ti-5_kennlinien-pt100-widerstaende-nach-toleranzklassen.pdf, zuletzt geprüft am 28.05.2020.

Emerie Dupius and Gerrard Hwang (2010): Custody Transfer: Flowmeter as Cash Register. Online verfügbar unter https://www.controleng.com/articles/custody-transfer-flowmeter-as-cash-register/, zuletzt aktualisiert am 26.05.2020, zuletzt geprüft am 26.05.2020.

Falcone, Gioia; Hewitt, Geoffrey F.; Alimonti, Claudio (2010): Multiphase flow metering. Principles and application. 1. ed. Amsterdam: Elsevier (Developments in petroleum science, 54). Online verfügbar unter http://gbv.eblib.com/patron/FullRecord.aspx?p=477342.

Fruhwirth (2019): Production Data Analysis and Modelling course materials.

G. Hartwig (2011): Einführung in die Fehler- und Ausgleichsrechnung. Norm:DIN1319. Hg. v. Carl Hanser Verlag. München. Online verfügbar unter https://www.hsaalen.de/uploads/mediapool/media/file/13430/F_Fehlerrechnung.pdf.

Gandhi, S. M.; Sarkar, B. C. (2016): Essentials of mineral exploration and evaluation. Amsterdam, Boston, Heidelberg: Elsevier.

Haldipur, Prashant; Metcalf, Gregory D. (2008): Virtual Metering Technology Field Experience Examples. In: Offshore Technology Conference. Offshore Technology Conference. Houston, Texas, USA, 2008-05-05: Offshore Technology Conference.

Hastie, Trevor; Tibshirani, Robert; Friedman, Jerome H. (2017): The elements of statistical learning. Data mining, inference, and prediction. Second edition, corrected at 12th printing 2017. New York, NY: Springer (Springer series in statistics).

IFA (2019). IFA: Institut für Arbeitsschutz. Online verfügbar unter http://gestis.itrust.de/nxt/gateway.dll/gestis_de/535513.xml?f=templates$fn=default.htm$3.

Jaadi, Zakaria (2019): A Step by Step Explanation of Principal Component Analysis. In: *Built In*, 04.09.2019. Online verfügbar unter https://builtin.com/data-science/step-step-explanation-principal-component-analysis, zuletzt geprüft am 28.05.2020.

Jan, Briers; Keat-Choon, Goh; Ann, Sniekers; Dave, Schotanus; John, Hofland; David, Adun (2016): Looking Back 2006 - 2016 - Ten Years of Data Driven Well Rate Estimates for Real-Time Surveillance and Optimization. In: SPE Intelligent Energy International Conference and Exhibition. SPE Intelligent Energy International Conference and Exhibition. Aberdeen, Scotland, UK, 2016-09-06: Society of Petroleum Engineers.

Jenny Hartmann-Schreier (2015.): Sudanblau II. Hg. v. Georg Thieme Verlag. Online verfügbar unter https://roempp.thieme.de/lexicon/RD-19-04643.

Melbø, Hallgeir: Software That Enables Flow Metering of Well Rates With Long Tiebacks and With Limited or Inaccurate Instrumentation. Online verfügbar unter https://pdfs.semanticscholar.org/75b3/1b259b092e5e7e4b73d0a2bfca1abdbdd1c9.pdf, zuletzt geprüft am 26.05.2020.

Melbø, Hallgeir; Morud, Svein Arne; van der Geest, Robert; Bringeda, Bjørn; Stenersen, Kjetil (2003): Software That Enables Flow Metering of Well Rates With Long Tiebacks and With Limited or Inaccurate Instrumentation. In: Offshore Technology Conference. Offshore Technology Conference. Houston, Texas, 2003-05-05: Offshore Technology Conference.

Missinglink.ai (2020a): 7 Types of Activation Functions. Online verfügbar unter https://missinglink.ai/guides/neural-network-concepts/7-types-neural-network-activation-functions-right/, zuletzt aktualisiert am 27.05.2020, zuletzt geprüft am 27.05.2020.

Missinglink.ai (2020b): Perceptrons & Multi-Layer Perceptrons: the Artificial Neuron. Online verfügbar unter https://missinglink.ai/guides/neural-network-concepts/perceptrons-and-multi-layer-perceptrons-the-artificial-neuron-at-the-core-of-deep-learning/, zuletzt aktualisiert am 27.05.2020, zuletzt geprüft am 27.05.2020.

Mokhtari, K.; Waltrich, P. J. (2016): Performance evaluation of multiphase flow models applied to virtual flow metering. In: C. A. Brebbia und M. Rahman (Hg.): Advances in Fluid Mechanics XI. AFM 2016. Ancona, Italy, 9/5/2016 - 9/7/2016: WIT PressSouthampton UK (WIT Transactions on Engineering Sciences), S. 99–111.

Nielsen, M. (2019): A visual proof that neural nets can compute any function. Online verfügbar unter http://neuralnetworksanddeeplearning.com/chap4.html.

Perkins, T. K. (1993): Critical and Subcritical Flow of Multiphase Mixtures Through Chokes. In: *SPE Drilling & Completion* 8 (04), S. 271–276. DOI: 10.2118/20633-PA.

RIS - Abfallwirtschaftsgesetz 2002 - Bundesrecht konsolidiert, Fassung vom 26.05.2020 (2020). Online verfügbar unter https://www.ris.bka.gv.at/GeltendeFassung.wxe?Abfrage=Bundesnormen&Gesetzesnummer=20002086, zuletzt aktualisiert am 26.05.2020, zuletzt geprüft am 26.05.2020.

Shoeibi Omrani, Pejman; Dobrovolschi, Iulian; Belfroid, Stefan; Kronberger, Peter; Munoz, Esteban (2018): Improving the Accuracy of Virtual Flow Metering and Back-Allocation through Machine Learning. In: Abu Dhabi International Petroleum Exhibition & Conference. Abu Dhabi International Petroleum Exhibition & Conference. Abu Dhabi, UAE, 2018-11-12: Society of Petroleum Engineers.

TAKACS, GABOR. (2017): ELECTRICAL SUBMERSIBLE PUMPS MANUAL. Design, operations, and maintenance. S.l.: GULF PROFESSIONAL. Online verfügbar unter http://www.sciencedirect.com/science/book/9780128145708.

Unneland, Trond; Hauser, Michael Kent (2005): Real-Time Asset Management: From Vision to Engagement-An Operator's Experience. In: SPE Annual Technical Conference and Exhibition. SPE Annual Technical Conference and Exhibition. Dallas, Texas, 2005-10-09: Society of Petroleum Engineers.

Varyan, R.; Haug, R. K.; Fonnes, D. G. (2015): Investigation on the Suitability of Virtual Flow Metering System as an Alternative to the Conventional Physical Flow Meter. In: SPE/IATMI Asia Pacific Oil & Gas Conference and Exhibition. SPE/IATMI Asia Pacific Oil & Gas

Conference and Exhibition. Nusa Dua, Bali, Indonesia, 2015-10-20: Society of Petroleum Engineers.

Walde, Janette: Principal Components Analysis (PCA). Online verfügbar unter https://www.uibk.ac.at/statistics/personal/janettewalde/lehre/phd_biology/ss2011/principal_component_analysis.pdf, zuletzt geprüft am 31.05.2020.

11 List of Tables

12 List of Figures

13 Abbreviations

Abbreviation	Name
ANN	Artificial neural network
ESP	Electrical submersible pump
GOR	Gas oil ratio
GFF	Gas volume fraction
IBC	Intermediate bulk container
MSE	Mean square error
MFM	Multiphase flowmeter
PCA	Principal Component Analysis
PTF	Pump-testing facility
QCLS	Quantum cascade laser spectrometer
RMSE	Root mean square error
VFM	Virtual flowmeter
WLR	Water liquid ratio

14 List of symbols

Symbol	Property	Unit
$\boldsymbol{A}_{\boldsymbol{gas}}$	Area occupied by gas	m²
$\boldsymbol{A}_{\boldsymbol{liquid}}$	Area occupied by liquid	m²
$\boldsymbol{\rho}$	density	kg/m³
$\boldsymbol{v}_{\boldsymbol{m}}$	Fluid mixture velocity	m/s
$\boldsymbol{Q}_{\boldsymbol{gas}}$	Gas flow rate	m³/s
$\boldsymbol{\lambda}_{\boldsymbol{gas}}$	Gas void fraction	%
$\boldsymbol{\alpha}_{\boldsymbol{gas}}$	Gas volume fraction	%
$\boldsymbol{\mu}$	Learning rate	-
$\boldsymbol{Q}_{\boldsymbol{liquid}}$	Liquid flow rate	m³/s
$\boldsymbol{\lambda}_{\boldsymbol{liquid}}$	Liquid hold-up	%
$\boldsymbol{\alpha}_{\boldsymbol{liquid}}$	Liquid volume fraction	%
$\boldsymbol{A}_{\boldsymbol{pipe}}$	Pipe diameter	m²
$\boldsymbol{v}_{\boldsymbol{s,gas}}$	Superficial gas velocity	m/s
$\boldsymbol{v}_{\boldsymbol{s,liquid}}$	Superficial liquid velocity	m/s
$\boldsymbol{\omega}$	weights	-

15 Appendix

Appendix A: Two-phase water prediction results

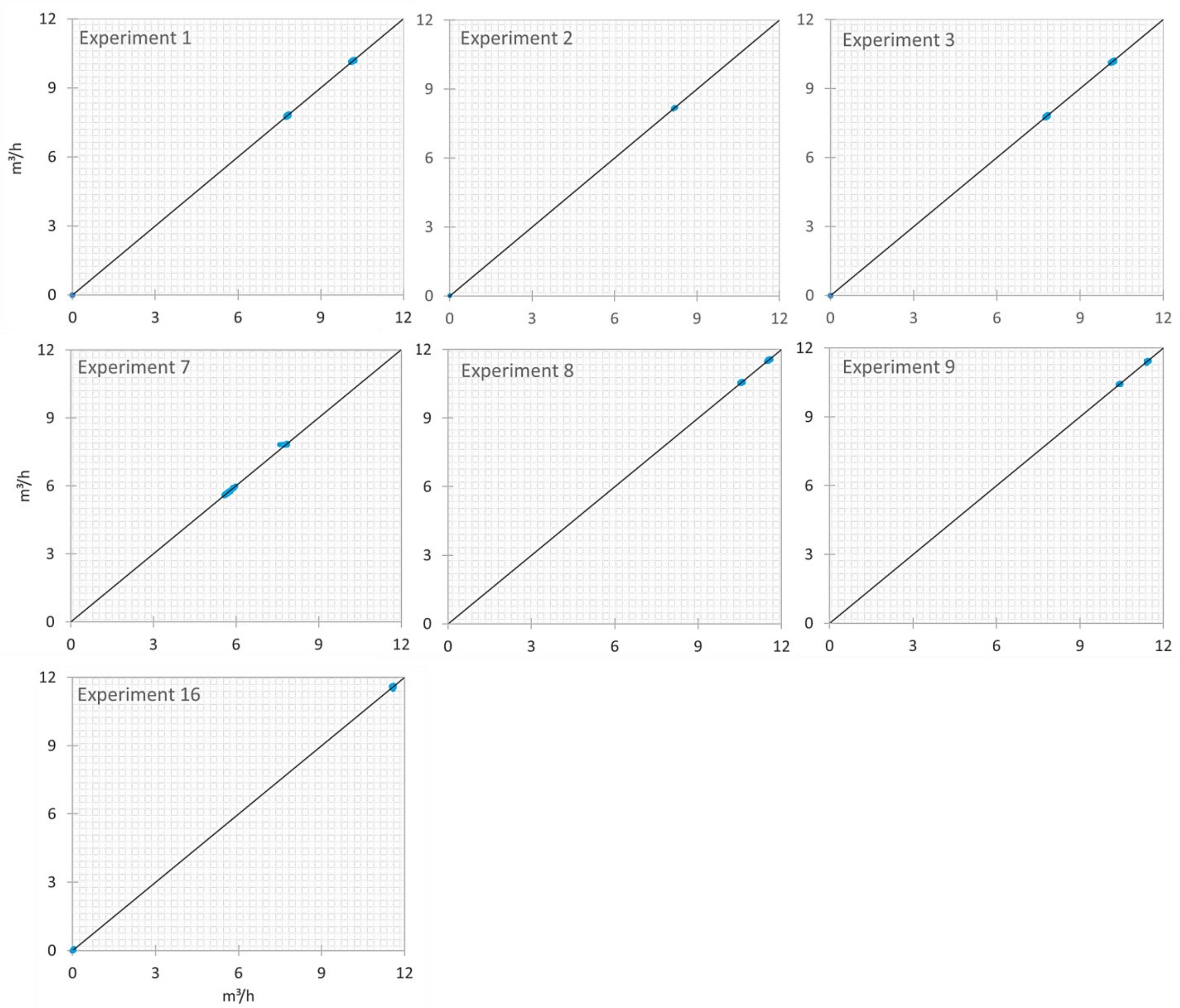

Fig. 1: Cross-plots of the two-phase water experiments showing the correlation between the predicted and measured water flow rate on the y and x-axis respectively. All seven experiments show a satisfactory degree of correlation indicating a good neural network performance.

Appendix B: Two-phase gas prediction results

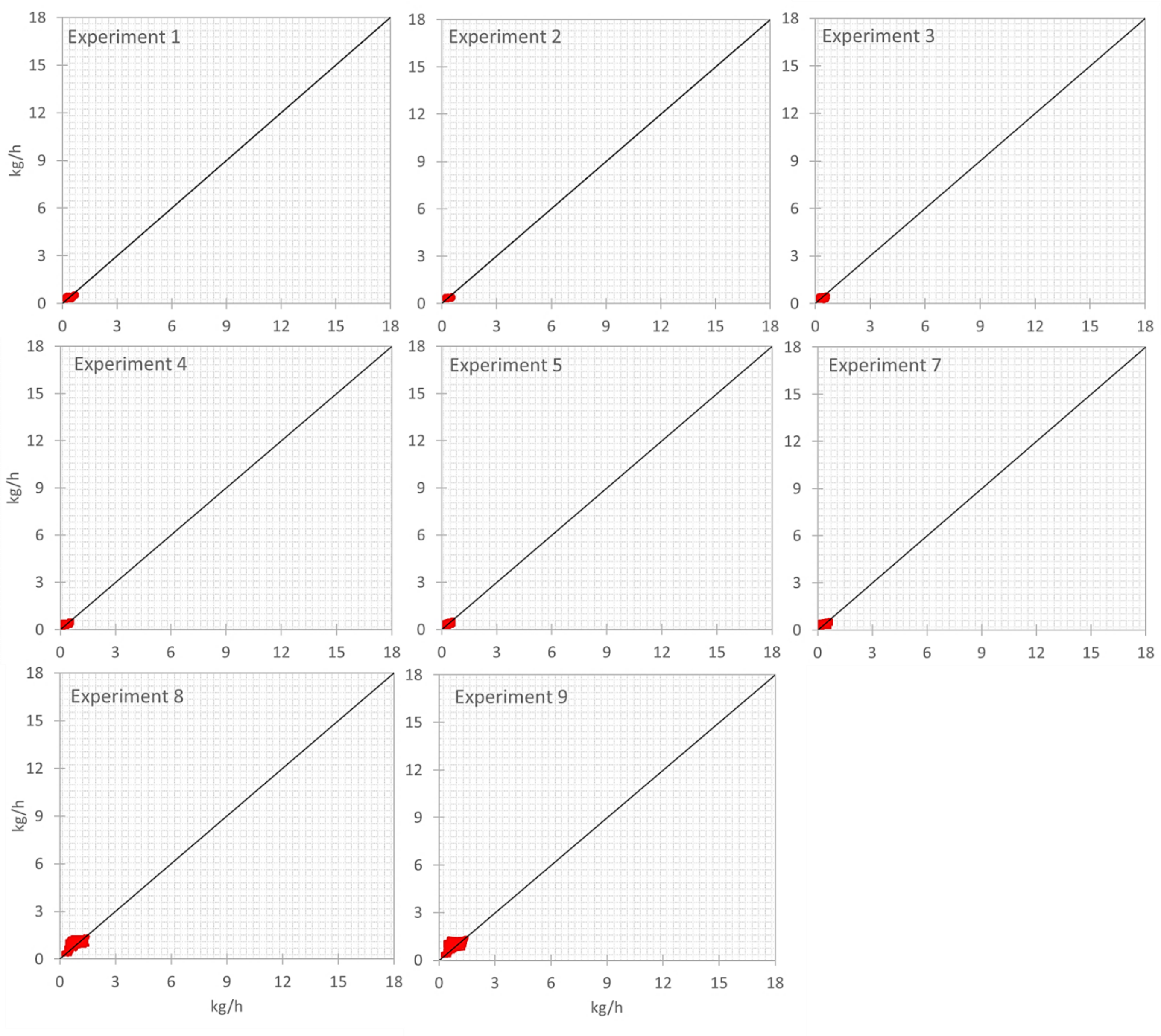

Fig. 2: Cross-plots of the two-phase gas experiments showing the correlation between the predicted and measured water flow rate on the y and x-axis respectively. All nine experiments show a satisfactory degree of correlation indicating a good neural network performance, nevertheless there is higher outliers density in the experiments 8 and 9.

Appendix C: Three-phase water prediction results

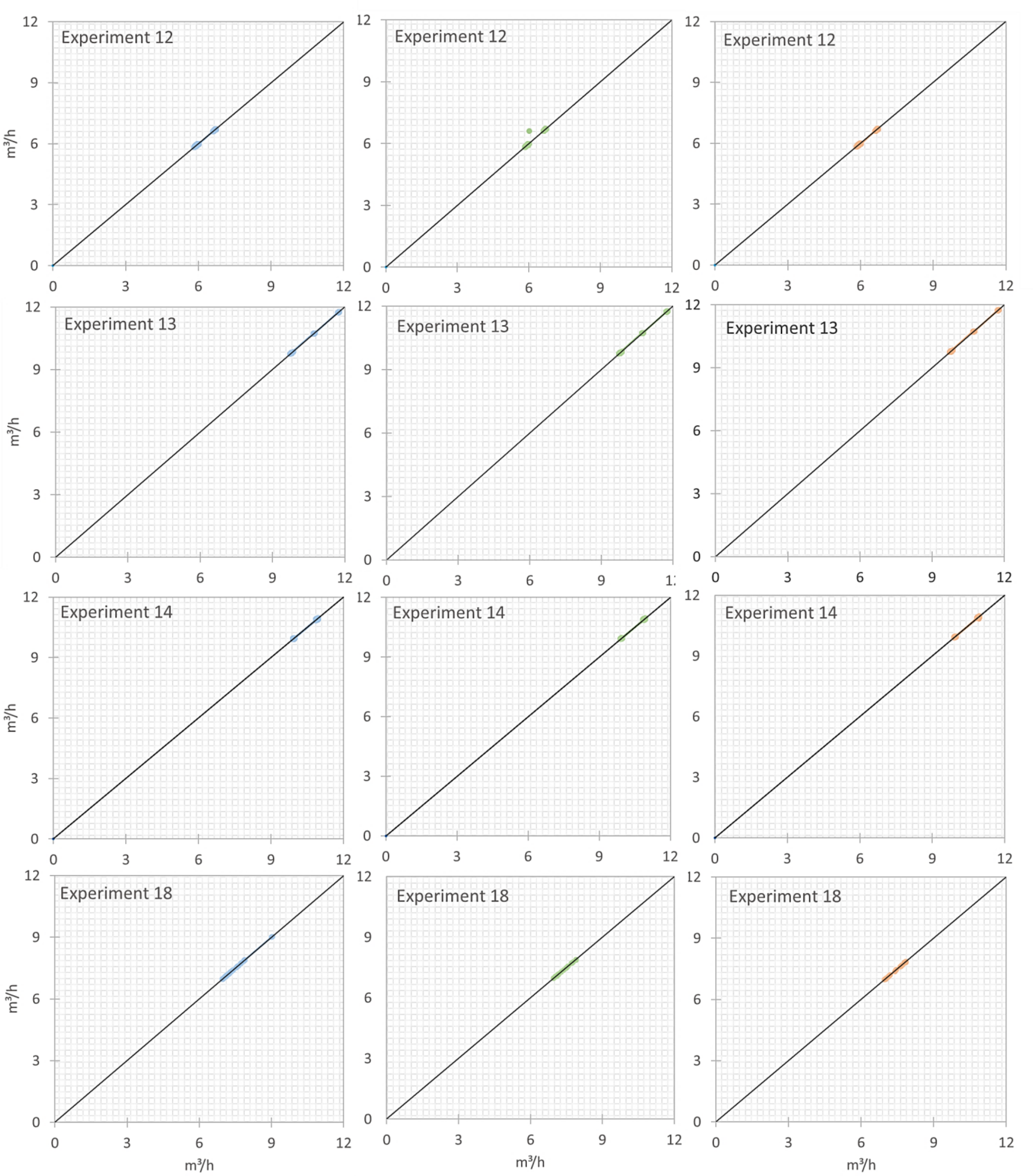

Fig. 3: Cross-plots of the three-phase experiments showing the correlation between the predicted and measured water flow rate on the y and x-axis respectively. The prediction results of the learning, validation and testing subset are plotted in blue, green and red respectively showing low variability between each subset and indicate a good artificial neural network performance

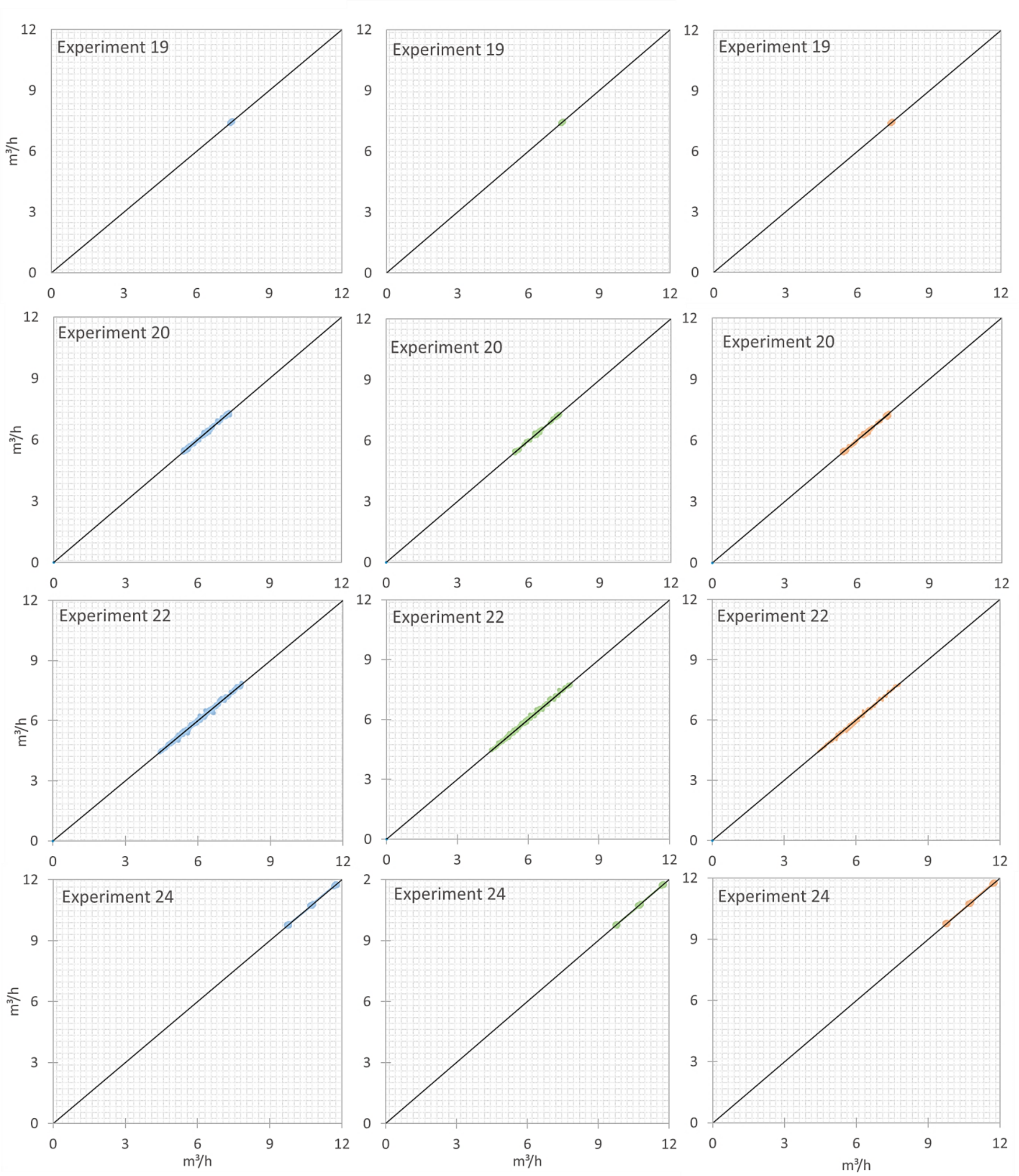

Fig. 4: Cross-plots of the three-phase experiments showing the correlation between the predicted and measured water flow rate on the y and x-axis respectively. The prediction results of the learning, validation and testing subset are plotted in blue, green and red respectively showing low variability between each subset and indicate a good artificial neural network performance.

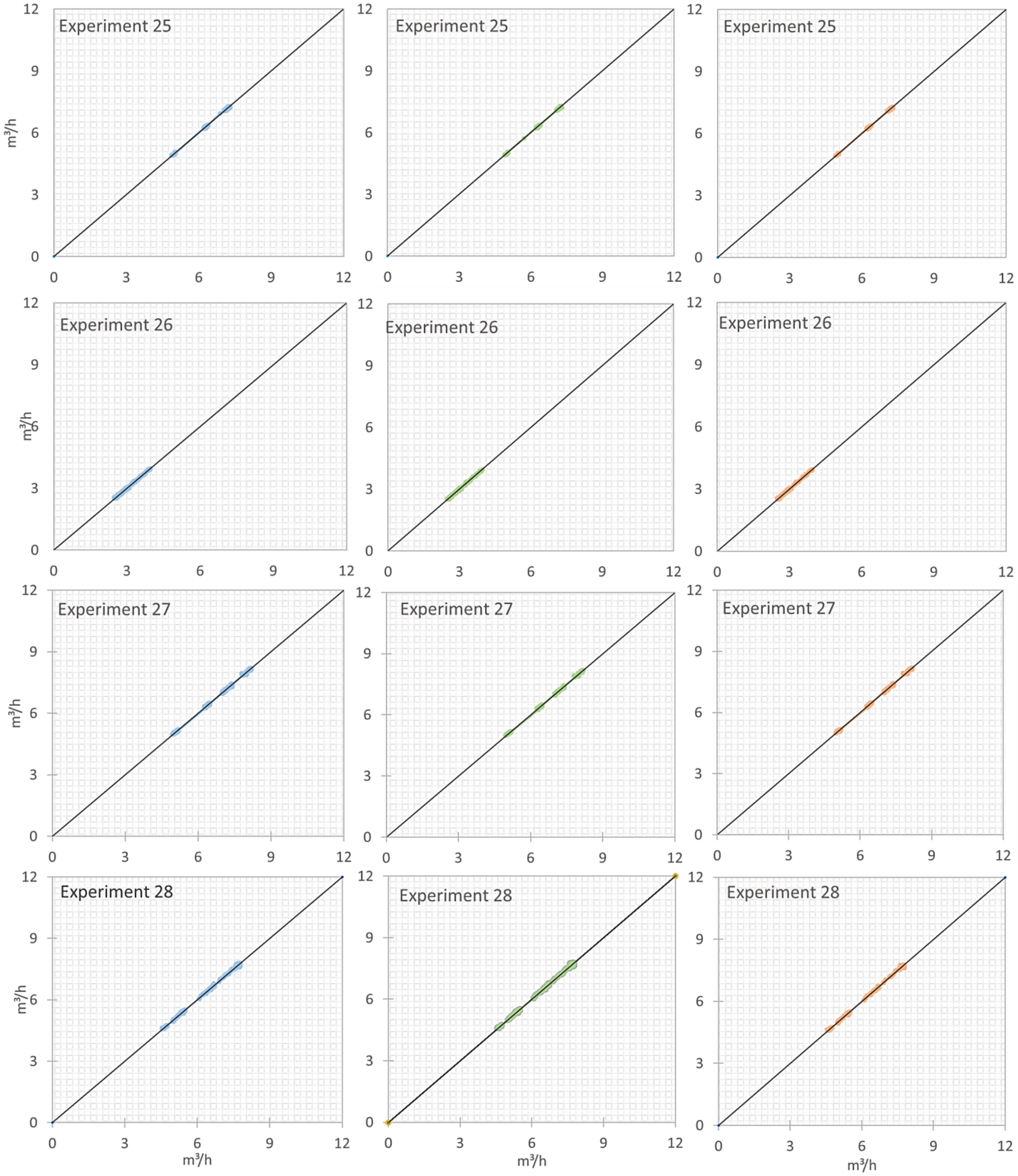

Fig. 5: Cross-plots of the three-phase experiments showing the correlation between the predicted and measured water flow rate on the y and x-axis respectively. The prediction results of the learning, validation and testing subset are plotted in blue, green and red respectively showing low variability between each subset and indicate a good artificial neural network performance.

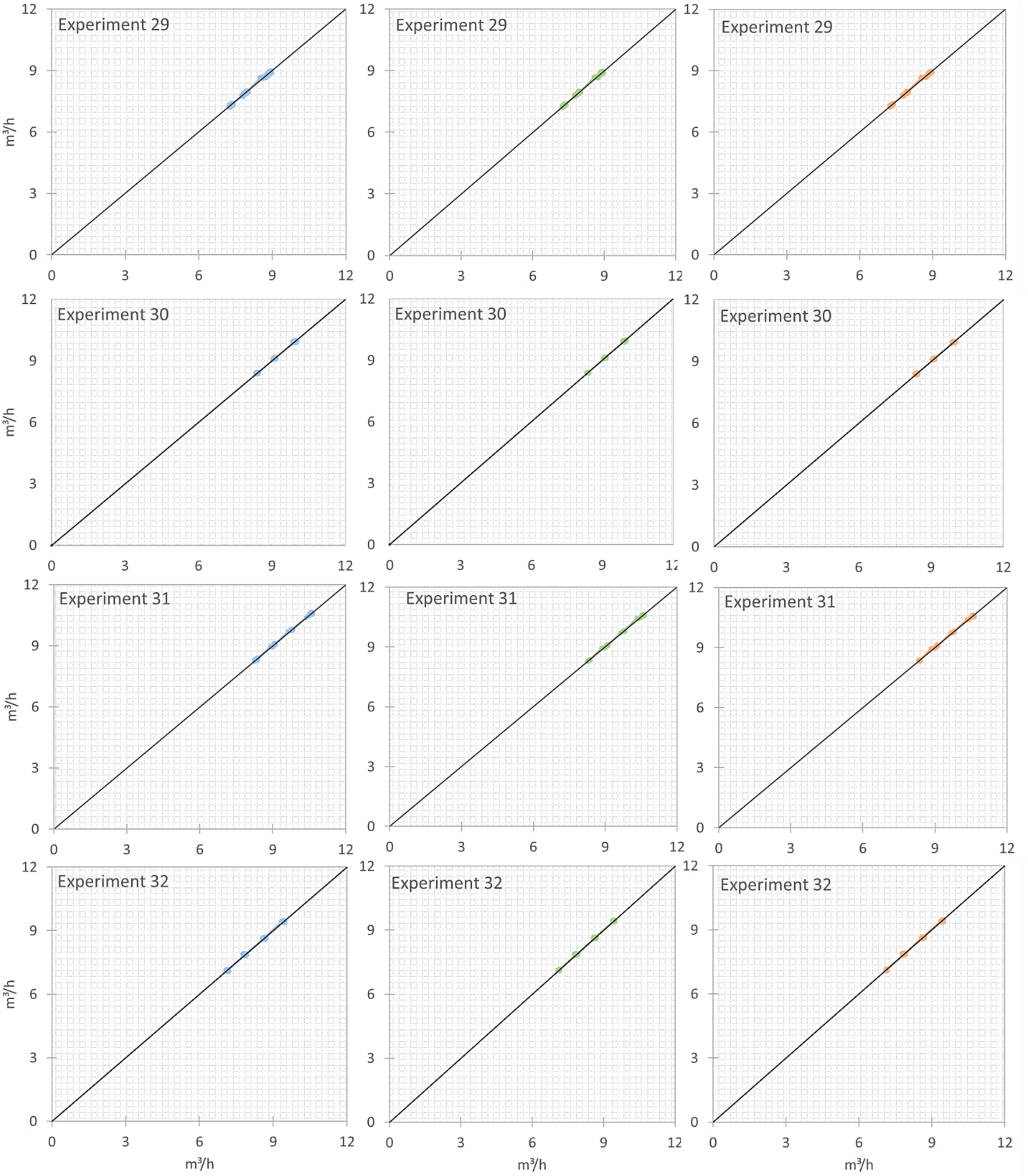

Fig. 6: Cross-plots of the three-phase experiments showing the correlation between the predicted and measured water flow rate on the y and x-axis respectively. The prediction results of the learning, validation and testing subset are plotted in blue, green and red respectively showing low variability between each subset and indicate a good neural network performance.

Appendix D: Three-phase oil prediction results

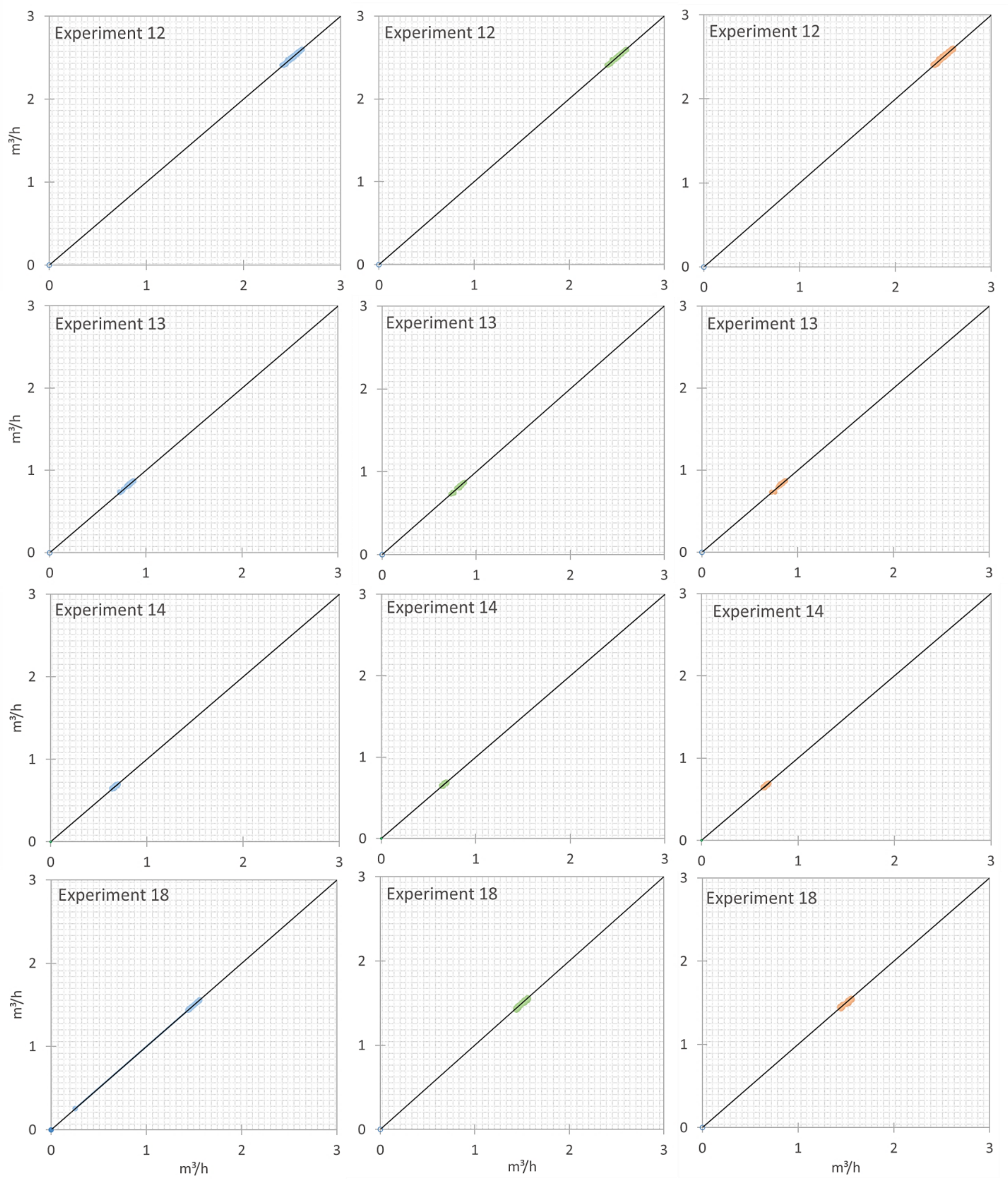

Fig. 7: Cross-plots of the three-phase experiments showing the correlation between the predicted and measured oil flow rate on the y and x-axis respectively. The prediction results of the learning, validation and testing subset are plotted in blue, green and red respectively showing low variability between each subset and indicate a good neural network performance.

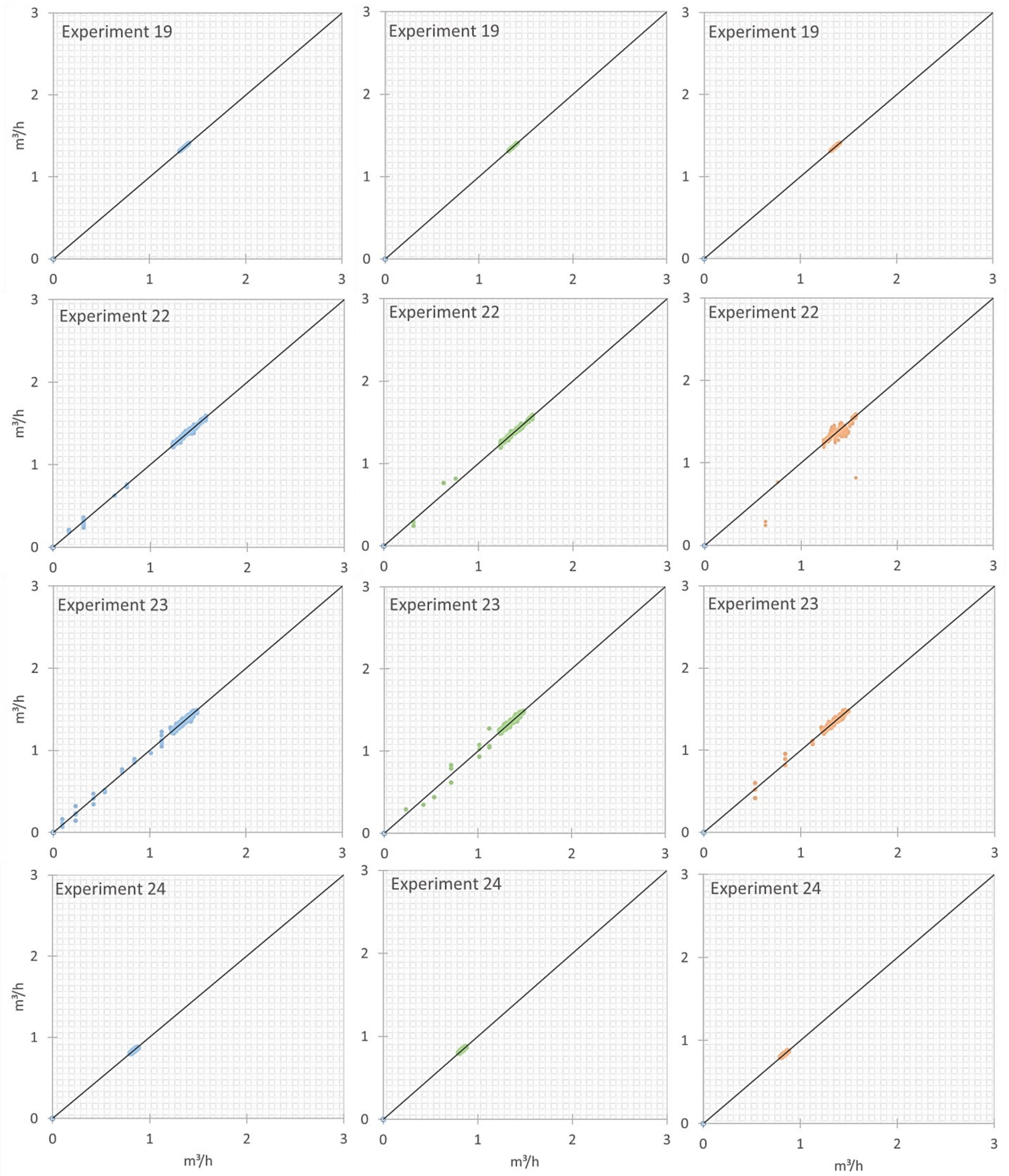

Fig. 8: Cross-plots of the three-phase experiments showing the correlation between the predicted and measured oil flow rate on the y and x-axis respectively. The prediction results of the learning, validation and testing subset are plotted in blue, green and red respectively showing low variability between each subset and indicate a good neural network performance.

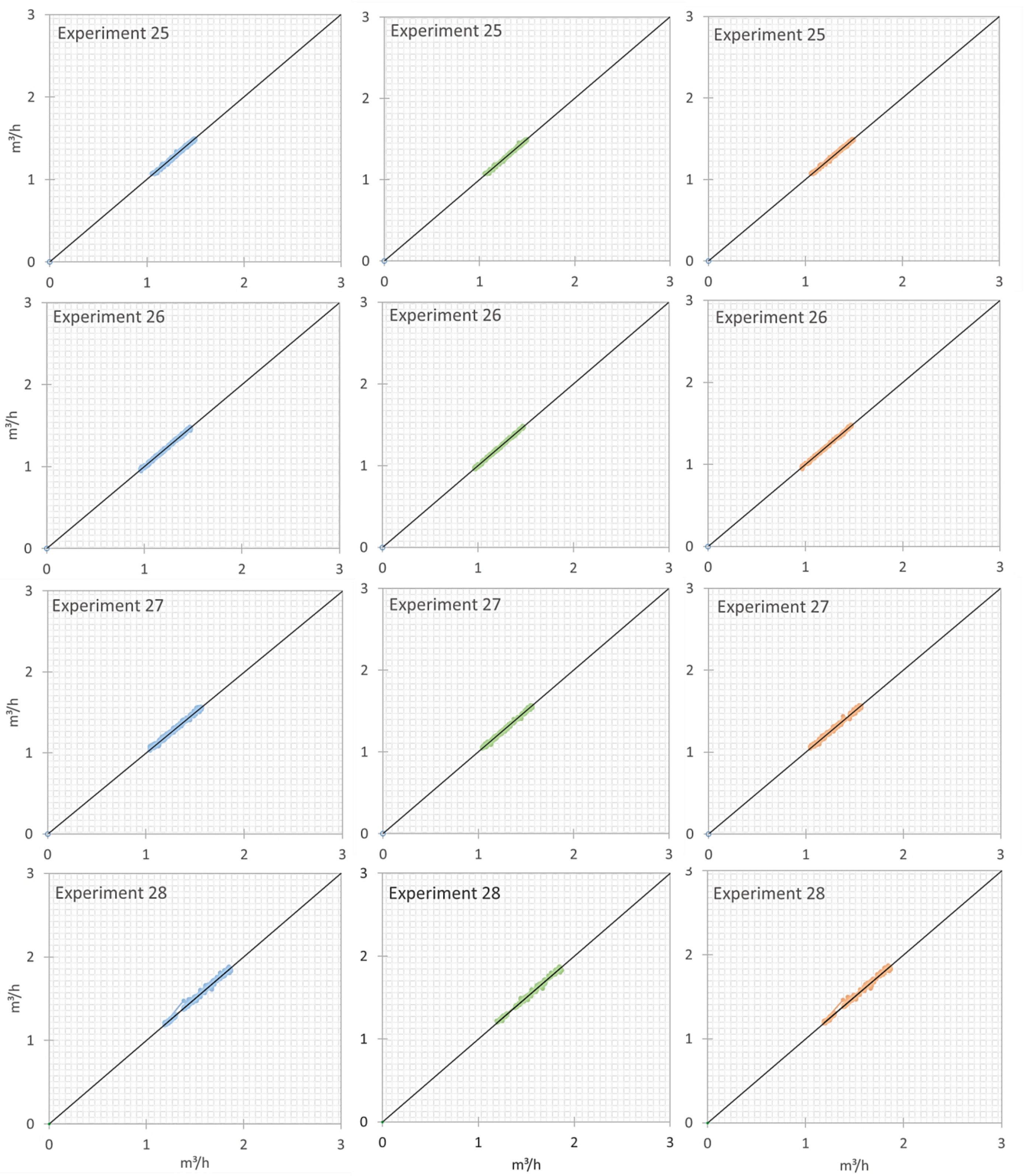

Fig. 9: Cross-plots of the three-phase experiments showing the correlation between the predicted and measured oil flow rate on the y and x-axis respectively. The prediction results of the learning, validation and testing subset are plotted in blue, green and red respectively showing low variability between each subset and indicate a good neural network performance.

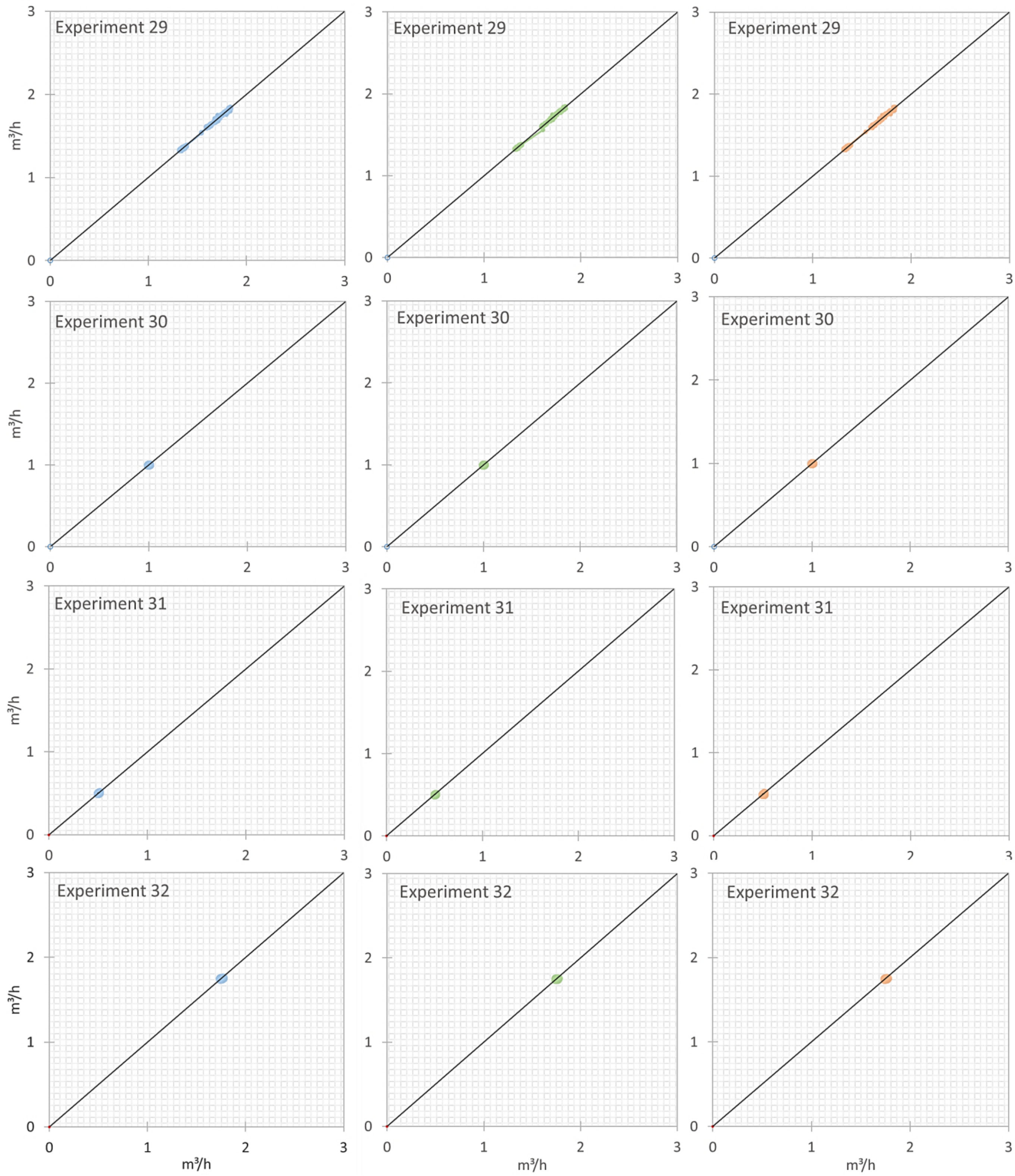

Fig. 10: Cross-plots of the three-phase experiments showing the correlation between the predicted and measured oil flow rate on the y and x-axis respectively. The prediction results of the learning, validation and testing subset are plotted in blue, green and red respectively showing low variability between each subset and indicate a good neural network performance.

Appendix E: Three-phase gas prediction results

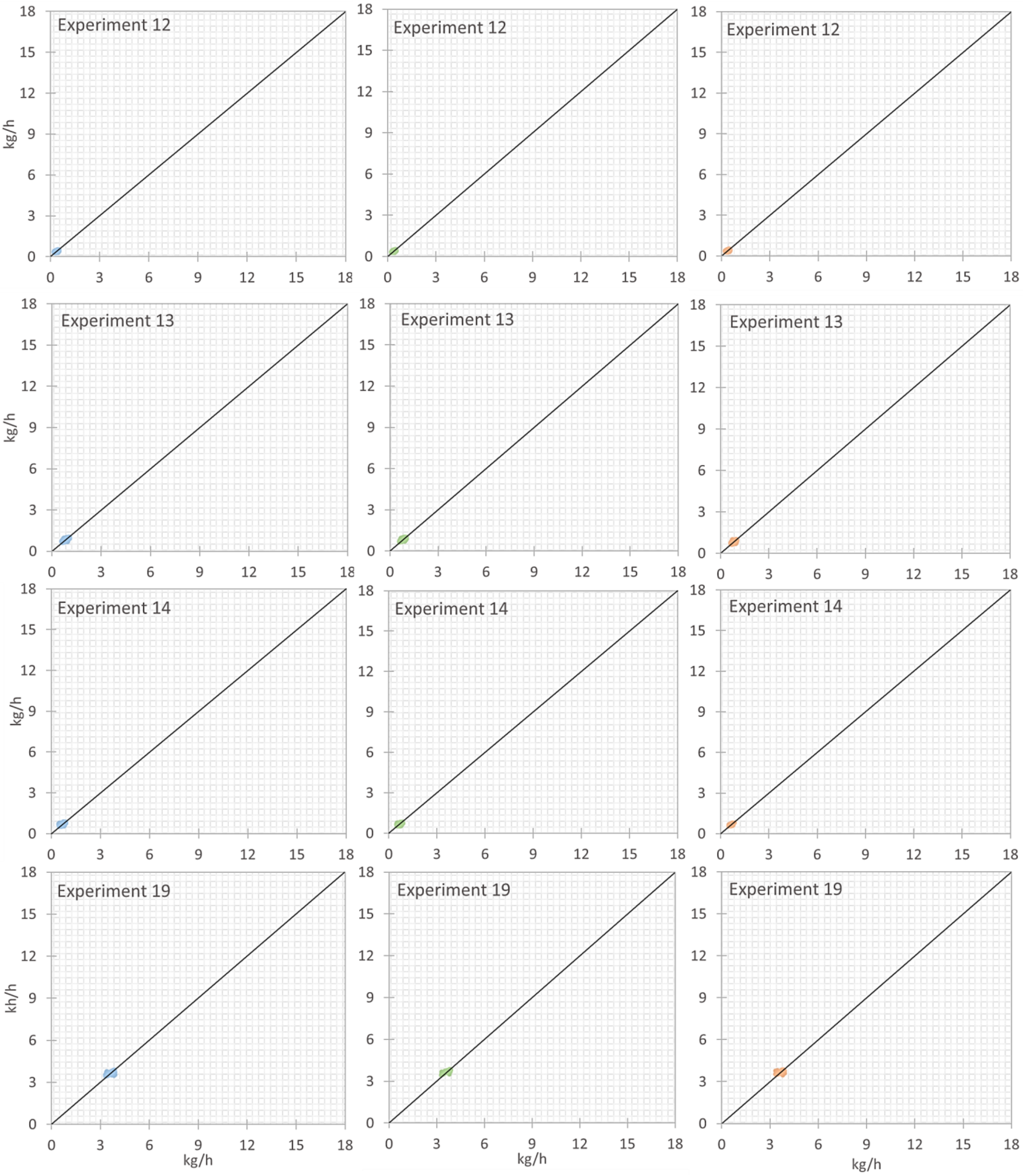

Fig. 11: Cross-plots of the three-phase experiments showing the correlation between the predicted and measured gas flow rate on the y and x-axis respectively. The prediction results of the learning, validation and testing subset are plotted in blue, green and red respectively showing low variability between each subset and indicate a good neural network performance.

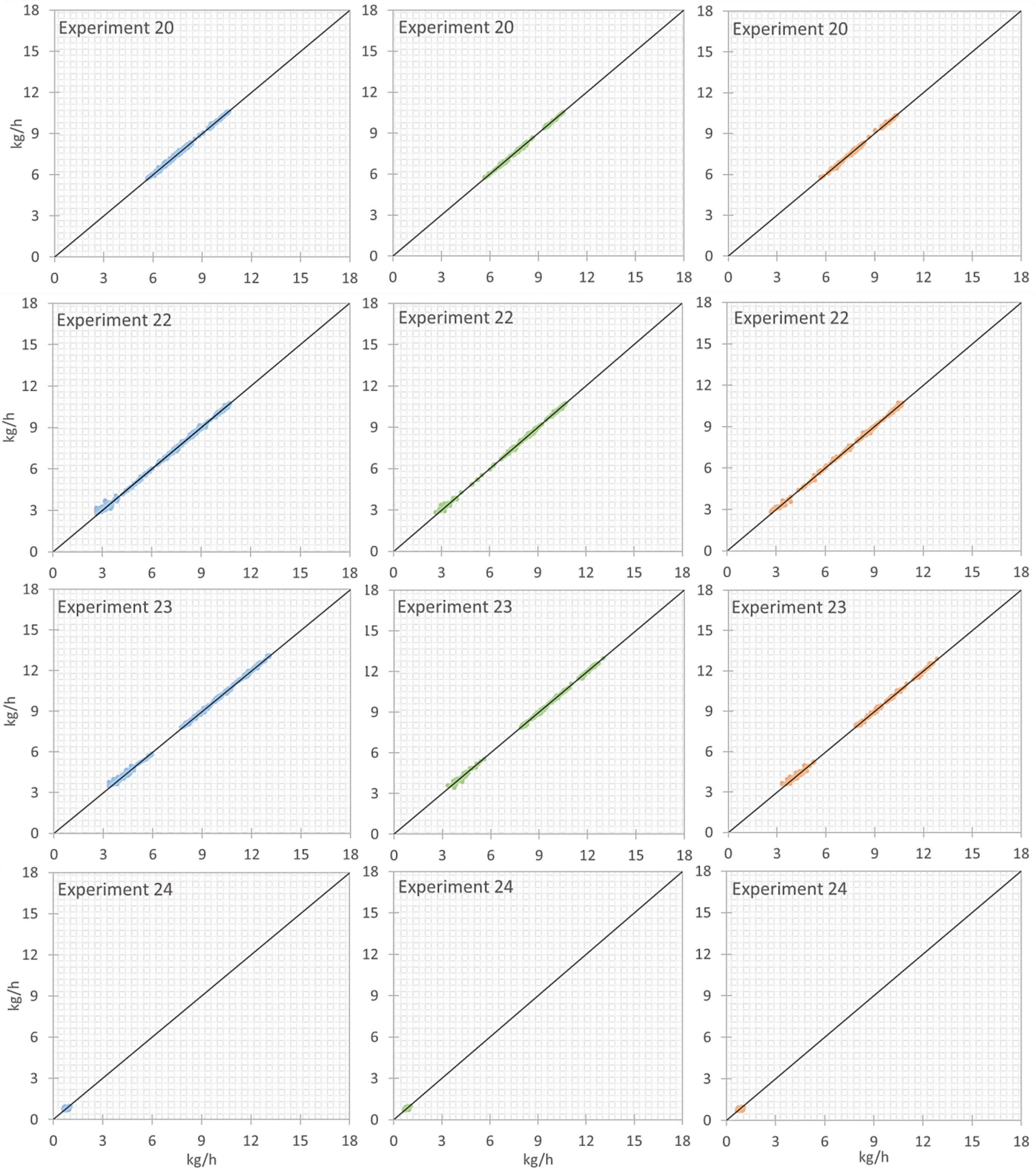

Fig. 12: Cross-plots of the three-phase experiments showing the correlation between the predicted and measured gas flow rate on the y and x-axis respectively. The prediction results of the learning, validation and testing subset are plotted in blue, green and red respectively showing low variability between each subset and indicate a good neural network performance.

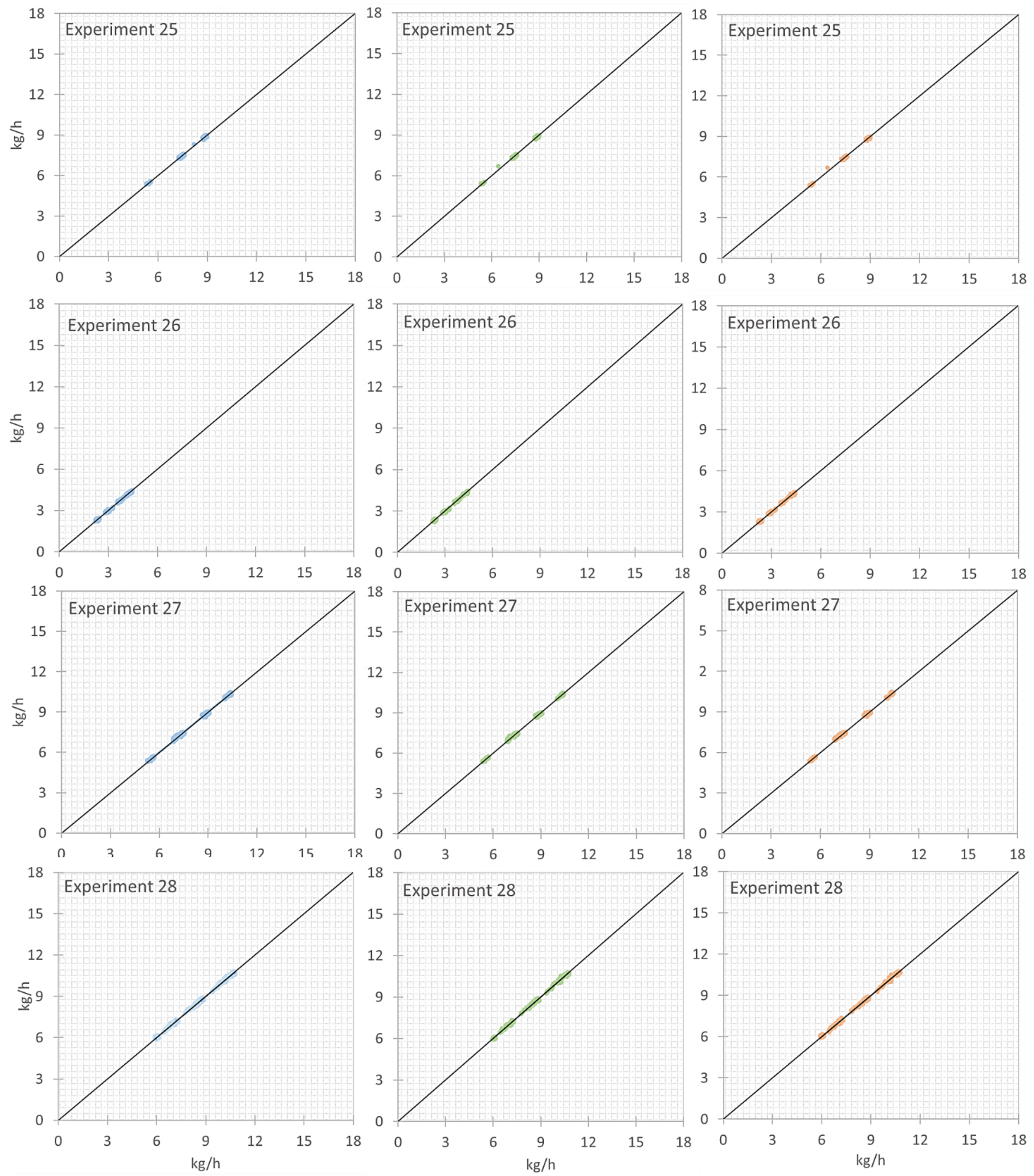

Fig. 13: Cross-plots of the three-phase experiments showing the correlation between the predicted and measured gas flow rate on the y and x-axis respectively. The prediction results of the learning, validation and testing subset are plotted in blue, green and red respectively showing low variability between each subset and indicate a good neural network performance.

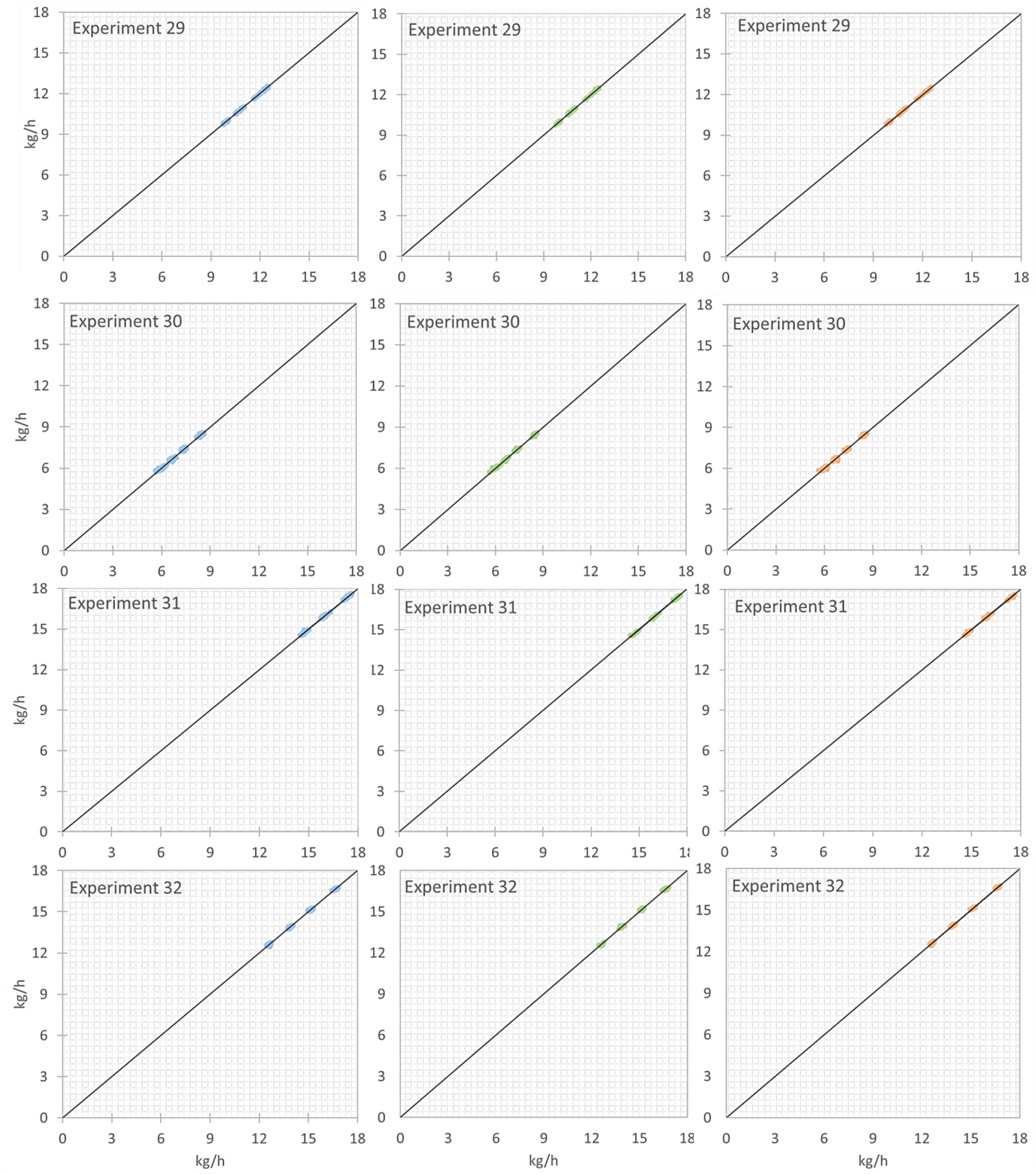

Fig. 14: Cross-plots of the three-phase experiments showing the correlation between the predicted and measured gas flow rate on the y and x-axis respectively. The prediction results of the learning, validation and testing subset are plotted in blue, green and red respectively showing low variability between each subset and indicate a good neural network performance.